THESIS

PREVENTION OF MUSCLE FIBROSIS IN DUCHENNE MUSCULAR DYSTROPHY VIA ENGINEERED MESENCHYMAL STROMAL CELL-MEDIATED FIBRONECTIN DEGRADATION

Submitted by

Helena R. Roell

School of Biomedical and Chemical Engineering

In partial fulfillment of the requirements

For the Degree of Master of Science

Colorado State University

Fort Collins, Colorado

Summer 2026

Master's Committee:

Advisor: Sing-Wan Wong

Soham Ghosh
Ben Gadomski
Dan Lark

Copyright by Helena R. Roell 2026

All Rights Reserved

ABSTRACT

PREVENTION OF MUSCLE FIBROSIS IN DUCHENNE MUSCULAR DYSTROPHY VIA ENGINEERED MESENCHYMAL STROMAL CELL-MEDIATED FIBRONECTIN DEGRADATION

Duchenne Muscular Dystrophy (DMD) is a genetic disorder caused by the loss of the protein dystrophin, resulting in progressive muscle degeneration and impaired regeneration. A hallmark feature of DMD pathology is excessive extracellular matrix (ECM) deposition, marked by early fibronectin accumulation followed by collagen-rich fibrosis. Currently, no therapies effectively prevent or reverse fibrosis in DMD, underscoring the need for new regenerative approaches.

Mesenchymal stromal cells (MSCs) have emerged as a promising cell-based therapy due to their ability to secrete a broad array of paracrine factors, including matrix-remodeling enzymes. Despite evaluation in over a thousand clinical trials, MSC-based therapies have yielded inconsistent outcomes, in part due to limited control over MSC behavior following administration. Given the mechanosensitivity of MSCs, which enables them to adapt functionally to their physical microenvironment, we sought to develop a mechanobiological strategy to enhance the therapeutic potential of MSC-derived secretomes for muscle fibrosis.

We hypothesized that conditioning MSCs within tunable hydrogel environments would enrich their secretion of matrix metalloproteinases (MMPs), thereby promoting fibrotic ECM remodeling in DMD. D1 murine MSCs were cultured on tissue culture plastic or encapsulated within alginate hydrogels of defined stiffness (~2.9–5.0 kPa) and stimulated with tumor necrosis factor–α (TNFα). Expression and secretion of MMP 2, 3, 9, and 10 were quantified using qPCR and ELISA. MSCs encapsulated in softer hydrogels exhibited enhanced MMP expression, with MMP-3 showing the most pronounced transcriptional upregulation, which was subsequently confirmed at the protein level.

Conditioned media from engineered MSCs was then administered via intramuscular injection into wild-type and dystrophin-deficient mice to assess therapeutic efficacy. Treated dystrophin-deficient mice demonstrated improved locomotor activity, alongside reduced fibronectin and collagen deposition within muscle tissue, as assessed by immunohistochemistry.

Collectively, these findings demonstrate that hydrogel-mediated mechanobiological conditioning enhances the ECM-remodeling capacity of engineered MSCs, leading to reduced fibrotic deposition and improved muscle function *in vivo*. This work supports the development of a novel therapeutic approach for managing muscle fibrosis in Duchenne Muscular Dystrophy.

ACKNOWLEDGEMENTS

I would like to acknowledge my advisor, Dr. Sing-Wan Wong and my committee members, Dr. Soham Ghosh, Dr. Ben Gadomski and Dr. Dan Lark for their support and insight on this project.

I would also like to thank all the members of the Orthopaedic Bioengineering Research Laboratory, particularly the histology department, who patiently and eagerly trained me on many instruments and protocols. I would also like to thank Dr. Ketul Popat and Sara Neys, who were both instrumental in bringing me to Colorado State University.

I would like to thank my labmates, Nick Serio, Ali Eldeiry, Thomas Leachman, and Salem Dietrich, for their friendship and guidance, and for making this lab feel like a family. I would also like to thank my undergraduates, for all their help in acquiring data and keeping the lab afloat (and constantly doing dishes!).

Finally, I would like to thank my parents and family (including my puppy Mocha!), who have supported me in every endeavor I've set out to chase, with this being the craziest of them all. I would also like to thank my friends, for their unconditional love and support, and for always having my back. I would not be who I am today, and none of this would have been possible without any of the amazing people I have mentioned, and I am truly grateful to have been guided, encouraged, and loved by all of them!

DEDICATION

I would like to dedicate this dissertation to my friends and family, who were confident in my abilities, even when I was not.

TABLE OF CONTENTS

ABSTRACT ii
ACKNOWLEDGEMENTS iv
DEDICATION v
LIST OF TABLES ix
LIST OF FIGURES x

Chapter 1 Introduction and Objectives 1
1.1 Motivation- Duchenne Muscular Dystrophy (DMD) 1
1.1.1 Injury Remodeling and Fibrosis in DMD 3
1.1.2 Matrix Metalloproteinases (MMPs) 9
1.1.3 Current Therapies for Muscle Fibrosis 11
1.2 Mechanobiology Engineering MSCs 12
1.2.1 Mesenchymal Stromal Cells 12
1.2.2 Overview of Current MSC Therapy Clinical Trials 15
1.3 Alginate 18
1.3.1 General Alginate Properties 18
1.3.2 Hydrogel Creation 20
1.4 Research Objectives 21
1.4.1 Aims 22
1.5 Organization of the Thesis Document 22

Chapter 2 Aim 1: Engineer biocompatible alginate hydrogels to enhance MSC secretion of MMPs 30
2.1 Introduction 30
2.2 Alginate as a Biocompatible Matrix 30
2.2.1 Materials Preparation: Alginate and Calcium Sulfate 30
2.3 Cell Culturing 32
2.3.1 General Cell Culturing 32
2.3.2 Cell Counting 33
2.3.3 Six-Well Plastic Culture 34
2.3.4 Gel-encapsulated MSCs 34
2.3.5 Gel Mechanical Characterization 37
2.3.6 Inflammation Factor 38
2.4 Plastic Wells RNA Purification and Reverse Transcription 39
2.5 Gel-encapsulated MSC Purification & Reverse Transcription 41
2.5.1 Digestion of Gel-encapsulated MSCs 41
2.5.2 CTAB protocol and RNA Purification/Reverse Transcription 42
2.6 qPCR 44
2.6.1 Primers 44
2.6.2 Quantitative PCR (qPCR) 44
2.7 MMP-3 ELISA 46

2.7.1 Collection of Conditioned Culture Media (CCM) from Gel-Encapsulated Cells and Plastic Culture . . . 46
2.7.2 Reagents . . . 47
2.7.3 Procedure and Analysis . . . 48
2.8 Stiffness Analysis of Hydrogels . . . 49
2.9 qPCR Results . . . 51
2.9.1 MMP-2 . . . 52
2.9.2 MMP-3 . . . 53
2.9.3 MMP-9 . . . 54
2.9.4 MMP-10 . . . 54
2.10 MMP-3 ELISA Results . . . 57
2.11 Discussion . . . 59

Chapter 3 Evaluate the Functionality of Engineered MSC Secretome *in vitro* . . . 66
3.1 Introduction . . . 66
3.2 Fibronectin Degradation Assay . . . 66
3.2.1 Modified Fibronectin ELISA kit . . . 66
3.2.2 Modified Incubation Protocol/APMA . . . 67
3.2.3 Filtration . . . 68
3.2.4 Incubation Protocol . . . 68
3.2.5 Fibronectin ELISA Assay Procedure . . . 69
3.2.6 Results . . . 70
3.3 Discussion . . . 71

Chapter 4 Evaluate the Therapeutic Efficacy of Engineered MSC Secretome on Rodent Muscle Fibrosis . . . 75
4.1 Introduction . . . 75
4.2 Animal Handling . . . 76
4.2.1 Home Cage Activity Monitoring Using AnyMaze . . . 76
4.2.2 Intramusuclar Injection of Engineered MSC Secretome . . . 78
4.2.3 Isolation of Murine Skeletal Muscle Tissue . . . 78
4.3 Histology . . . 79
4.3.1 Tissue Processing . . . 79
4.3.2 Tissue Embedding . . . 79
4.3.3 Tissue Sectioning . . . 80
4.3.4 Masson's Trichrome Staining . . . 80
4.3.5 Immunohistochemistry (IHC) Staining . . . 81
4.3.6 Imaging . . . 83
4.4 AnyMaze Results . . . 85
4.4.1 Distance Traveled . . . 86
4.4.2 Anti-Clockwise Turning Behavior . . . 87
4.5 Fibronectin Deposition After Engineered MSC Treatment . . . 88
4.5.1 Baseline Comparison: mdx vs. DBA . . . 89
4.5.2 Treatment Effects in Thigh Muscle . . . 89
4.5.3 Treatment Effects in Calf Muscle . . . 90

4.6 Collagen Deposition After Engineered MSC Treatment 92
4.6.1 Baseline Comparison: mdx vs. DBA 93
4.6.2 Treatment Effects in Thigh Muscle 94
4.6.3 Treatment Effects in Calf Muscle 95
4.7 Discussion 97

Chapter 5 Conclusions and Future Works 106
5.1 Conclusions 106
5.2 Future Work 108

Appendices 110

Appendix A CTAB Bulk Mixture Recipe (100 mL) 111

Appendix B MMP-3 Excel Standard Curves 112

Appendix C ImageJ Editable Collagen Macro 113

Appendix D ImageJ Editable Fibronectin Macro 119

LIST OF TABLES

1.1 MMP Classification and Degradative Capabilities 10

2.1 Dialysis Concentrations 31
2.2 CTAB Reagents and Purposes 43
2.3 Primer and Probe Sequences used for qPCR. 45

LIST OF FIGURES

1.1 (A) Illustration of the 23 human chromosomes, with location of the DMD gene on the Xp21 locus enlarged. Image modified in Biorender to show location of DMD. Note. Adapted from "The genetics of human blood," by H. L. Carson, n.d., *Encyclopædia Britannica*. Retrieved November 4, 2025, from https://www.britannica.com/science/human-genetics/The-genetics-of-human-blood. Copyright Encyclopædia Britannica, Inc. (B) Prevalence of Duchenne and Becker muscular dystrophy by race/ethnicity. Note. Adapted from [4] 2
1.2 Schematic of clinical progression of DMD, including age range, body areas affected, and disease stages. Note. Adapted from "MRI biomarkers for Duchenne muscular dystrophy (DMD)," by E. Laurie & B. J. Bedell, 2025, *Biospective*. https://imaging-cro.biospective.com/resources/mri-biomarkers-duchenne-muscular-dystrophy. Copyright 2025 by Biospective Inc. 3
1.3 Cryo-EM structure of native dystrophin-glycoprotein complex. This figure visualizes the relationship between the cytoplasm, DGC, sarcolemma, and the ECM. Note. Adapted from "Native DGC structure rationalizes muscular dystrophy-causing mutations," by S. Liu, T. Su, X. Xia, & Z. H. Zhou, 2024, *Nature*, 637(8006), 1261–1271. https://doi.org/10.1038/s41586-024-08324-w. Copyright 2024 by Springer Nature. . . 4
1.4 (A) Schematic illustration of the arrangement of 3 specimen types. Single fibers (curved pink lines) were isolated from the muscle and tested individually or secured in groups. Bundles of a similar number of fibers embedded in ECM (light pink) were isolated and similarly secured (B) Normalized stiffness of fibers, fiber groups, and fiber bundles. Fiber bundles have a significantly higher modulus than either individual fibers or fiber groups, demonstrating that the ECM provides a large fraction of the loadbearing. Fiber and fiber group moduli were not significantly different from each other. Connecting bars represent significant differences ($P < 0.05$). Note. Both A and B reprinted from [11] 5
1.5 (A) Soft tissue elasticity scale ranging from soft brain, fat, and striated muscle to stiff cartilage [E ~20 to 30 kPa at the scale of adhesions] and precalcified bone. Note. Adapted from [15]. (B) Muscle size and mechanical properties from wildtype (n = 10; 5M/5F) and mdx (n = 10; 5M/5F) mice. Elastic stiffness taken as the elastic modulus at 10% strain shows the mdx EDL is significantly stiffer than the wildtype EDL. The soleus had similar stiffness between genotypes. (C) Collagen content and solubility, determined through a hydroxyproline assay, and its relation to passive mechanics. The amount of collagen per muscle in wildtype and mdx muscles. The soleus muscle collagen content of mdx mice was significantly increased compared with the wildtype (n = 6 wildtype; n = 8 mdx). Note. Figures B and C adapted from [14] 7

1.6 (A) Diagram of a FN monomer showing binding and interaction sites. Fn exists as a dimer of two nearly identical monomers, linked at the C-terminus by disulfide bonds. The yellow circles show the 6 nm Forster energy transfer radius for the acceptor dyes that are located on modules FnIII7 and FnIII15 in FRET-labelled Fn. While the FRET radii are drawn roughly to scale to indicate which modules are covered, other aspects of the diagram are not necessarily to scale. The canonical collagen/gelatin-binding domain, the R1R2 bacterial-adhesin-derived peptide, and the two binding sites for a CLP encompassing the Fn-binding domain of the collagen I $\alpha 1$ chain are shown in bold. (B) Hypothetical model of collagen fibril nucleation at the plasma membrane. (1) Dimeric FN (black) binds to $\alpha 5\beta 1$ integrins (green). (2) Engagement of the integrin with the cytoskeleton (red lines) causes a conformational change in FN with subsequent fibril formation. Additional receptors (orange bars) bind FN. (3) Collagen I, procollagen I (black), and collagen V (purple) engage with FN at the fibril surface to facilitate collagen fibril formation. Decorin (interlocking dimers) shown bound to procollagen. (4) Activated collagen integrins (e.g. $\alpha 2\beta 1$) bind collagen and induce a conformation change that facilitates fibril formation. (5) Collagen fibril formation at the cell surface. (6) Interactions between collagen fibrils determine fibril diameter, organization, and spacing. Note. (A) Adapted from [13]; (B) Adapted from [16]. . . . 8

1.7 (A) Major MMP subtypes and structures. A typical MMP consists of a propeptide, a catalytic domain, a linker peptide (hinge region), and a hemopexin domain. The propeptide has a cysteine switch (PRCGXPD) whose cysteine sulfhydryl (–SH) group chelates the active site Zn^{2+}, keeping the MMP in the latent proMMP zymogen form. The catalytic domain contains the Zn^{2+} binding motif HEXXHXXGXXH, two Zn^{2+} ions (one catalytic and one structural), specificity conferring 'S-pockets', and two or three Ca^{2+} ions for stabilization. Some MMPs show exceptions in their structures. Gelatinases have 3 type-II fibronectin repeats in the catalytic domain. Note. Adapted from [23] (B) The three forms of MMPs as illustrated in MMP-2. MMPs are made as inactive zymogens or proMMPs. They are activated by removal of the propeptide domain. MMPs are regulated primarily by complexation with TIMPs. Note. Adapted from [22] 11

1.8 MSC isolation, expansion, differentiation and niche. MSCs can be isolated from various tissues. Upon isolation, MSCs may be expanded and enriched by *in vitro* passaging. A combination of positive and negative markers can be used to determine MSC purity. These cells can undergo differentiation *in vitro*, generating adipo, osteo, and chondrocytes, in addition to neurons and myocytes. Note. Adapted from [21] 14

1.9 (A) MSC clinical trials classified by disease categories subdivided by progress status: in green, "Recruiting Status"; in red, "Completed"; in yellow, "Active not recruiting"; in magenta, "Terminated". The 22 shown categories account for >90% of the trials reported on clinicaltrials.gov from 2015 to present. Note. Reprinted from [29] (B) MSC clinical trials classified by disease categories and subdivided by progress status: in blue "Withdrawn/Suspended/Terminated"; in pink "Active/Other"; in purple "Completed", representing ~293 trials as of October 2025. Information sourced from ClinicalTrials.gov, visualized using GraphPad Prism. 17

1.10 3D matrix stiffness regulates expression of TNF-α-inducible genes implicated in monocyte functions. Effects of 3D matrix stiffness on protein secretion kinetics in response to TNF-α. Data were fitted to standard one-phase association curves. (i) CCL2: t1/2 = 126 hours for both soft and stiff; plateau for soft = 156-fold and for stiff = 61-fold. (ii) IL-6: t1/2 = 204 hours for both soft and stiff; plateau for soft = 143-fold and for stiff = 58-fold. Fold change refers to increase over untreated condition. Note. Adapted from [33]. 18
1.11 Representative alginate structure: (A) chain conformation and (B) block distribution. Note: Adapted from [38] 19
1.12 (A) Schematic drawing and calcium coordination of the "egg-box" model, as described for the pair of guluronate chains in calcium ALG junction ones. Dark circles represent the oxygen atoms involved in the coordination of the calcium ion. Note. Adapted from [39] (B) Molecular structure of anhydrous Calcium sulfate ($CaSO_4$) (C) Molecular structure of calcium carbonate ($CaCO_3$) Note. B and C rendered in Webqc.org 21

2.1 Fabrication of cell-laden alginate hydrogels. (A) Two syringes containing either (1) Alginate/FluoroBrite DMEM solution or cell pellet suspension or (2) cell/alginate mixture or $CaSO_4$ are connected and rapidly pressed back and forth for mixing. (B) The resulting $CaSO_4$/alginate mixture is deposited onto a glass slide. (C) Base slide is flanked by two 1 mm spacer slides and covered by a third slide to ensure uniform 1 mm thickness across gel. (D) After gelation period, four punchouts (8 mm diameter) were taken from each gel. Note. Figure generated in Biorender. 36
2.2 Well-plate configurations for hydrogel and plastic cultures. (A) 24-well plate layout for cell-laden alginate hydrogels: orange wells contain standard culture media; red wells contain TNF-α-supplemented media. (B) 6-well plate layout for MSC plastic cultures: orange = standard media, red = TNF-α-supplemented media. Note: Schematics in A and B were created using BioRender. 39
2.3 PCR Plate Layout. Target genes are sectioned by black lines, and labeled GAPDH, MMP-2, MMP-3, MMP-9 and MMP-10. Colors for samples are pink = soft gel control, purple = soft gel TNF-α, blue = stiff gel control, green = stiff gel TNF-α, orange = plastic control, red = plastic TNF-α. Samples were analyzed in triplicate to ensure reproducibility and statistical reliability. 46
2.4 MMP-3 ELISA plate layout for a single experiment containing a standard curve (purple), soft gel control (light pink), soft gel TNF-α (dark pink), stiff gel control (light blue), stiff gel TNF-α (dark blue), plastic control (light green), and plastic TNF-α (dark green). All samples were performed in duplicate. 49
2.5 Young's Modulus measurements of alginate hydrogels. Comparison between the softest (15 mM $CaSO_4$) and stiffest (40 mM $CaSO_4$) hydrogels: the softest formulation exhibited a mean Young's Modulus of 2.91 kPa, while the stiffest reached 5.00 kPa. Statistical analysis yielded a p-value < 0.0329. Note. Graph visualized in GraphPad Prism. 51

2.6 MMP Expressions in Plastics and Gel-Encapsulated MSCS, significance established by Two-Way Anova and confirmed with Tukey's post-hoc HSD. (A) MMP-2 expression is significantly upregulated in the soft gel with inflammation factor (soft TNF-α) compared to the plastic control (p = 0.0050), the plastic TNF-α (p = 0.0032), the soft control (p = 0.0114), and the stiff control (p = 0.0117). Significance was also established between the soft TNF-α and the stiff TNF-α (p = 0.0350). (B) MMP-3 expression is significantly upregulated in the soft gel with inflammation factor (soft TNF-α) compared to the plastic control (p = 0.0244), plastic TNF-α (p = 0.0266), the soft control (p = 0.0248), and the stiff control (p = 0.0258). No significance established between the soft TNF-α and stiff TNF-α. The scale at which MMP-3 was upregulated was much larger than in other MMPs. (C) MMP-9 expression is significantly upregulated in the soft gel with inflammation factor (soft TNF-α) compared to the and the soft control (p = 0.0070) and stiff control (p = 0.0056). No significance was established between the soft TNF-α and stiff TNF-α. MMP-9 plastic control and TNF-α data obtained at this time did not fit inclusion criteria. (D) MMP-10 expression is significantly upregulated in the soft gel with inflammation factor (soft TNF-α) when compared to the plastic control (p = 0.0010), plastic TNF-α (p = 0.0072), soft control (p = 0.0009) and the stiff control (p = 0.0045). Significance was also established between the soft TNF-α and the stiff TNF-α (p = 0.0083). Note. All graphs visualized in GraphPad Prism. 56

2.7 MMP-3 ELISA Assay Results. Statistical analysis using two-way ANOVA revealed revealed significant main effects of row factor (gel encapsulation) (F(2, 26) = 8.850, p = 0.0012), column factor (TNF-α vs. Control) (F(1, 26) = 47.07, p <0.0001), and interaction between factors (F(2, 26) = 8.272, p = 0.0017). Tukey's HSD post hoc analysis revealed significant pairwise differences between the soft gel with TNF-α (soft TNF-α) and the plastic control (p < 0.0001), plastic TNF-α group (p = 0.0003), soft control (p < 0.0001) and the stiff control (p < 0.0001). The stiff TNF-α group also showed significant differences when compared to the plastic control (p < 0.0001), plastic TNF-α (p = 0.0002), soft control (p < 0.0001) and stiff control (p < 0.0001). No significance was established between the soft TNF-α and stiff TNF-α groups. . . . 58

3.1 Fibronectin ELISA plate layout for a single experiment containing a standard curve (purple), plastic control (light pink), plastic TNF-α (dark pink), soft gel control (light blue), soft gel TNF-α (dark blue), stiff gel control (light green), stiff gel TNF-α (dark green), recombinant MMP-3 (orange), and untreated culture media (red). All samples were performed in duplicate. 70

4.1 Example comparison image generated from ImageJ code for collagen content analysis. Image is of a 24-week mdx thigh, analyzed with a custom macro in Fiji (ImageJ). . . . 84

4.2 Example comparison image generated from ImageJ code for fibronectin content analysis. Image is of a 24-week untreated mdx thigh, analyzed with a custom macro in Fiji (ImageJ). 85

4.3 AnyMaze Results of sixteen 20 -24 week female mice divided into four groups (n = 4 per group): wild-type DBA mice without injection, wild-type DBA mice receiving injection, dystrophin-deficient (mdx) mice without injection, and dystrophin-deficient (mdx) mice receiving injection. **(A)** Distance traveled. Wild-type DBA mice exhibited low and stable levels of locomotion, mdx mice demonstrated consistently elevated locomotor activity relative to DBA controls. Treated mdx mice displayed notably higher and more variable locomotor activity, while untreated mdx mice exhibited more stable activity levels. **(B)** Anti-clockwise turning behavior. DBA mice exhibited low to moderate levels of turning behavior with modest variability. mdx mice displayed a marked increase in anti-clockwise turning behavior, and treated animals showed particularly elevated and more variable turning behavior across the testing period. Untreated mdx mice exhibited more constrained and consistent values compared to treated mdx mice. 88

4.4 Quantification of fibronectin deposition in thigh and calf muscles across DBA and mdx mice following treatment. **(A)** mdx mice showed significantly elevated fibronectin compared to DBA controls at baseline, with greater severity in calf muscle. **(B)** In the thigh, conditioned culture media (M) significantly reduced fibronectin levels in mdx mice relative to untreated (U) and culture media (C) groups, resulting in values comparable to DBA controls, while CM alone had no significant effect. **(C)** In the calf, CCM produced a more pronounced reduction in fibronectin, consistent with increased baseline disease severity, whereas CM showed only partial or variable effects. No significant treatment effects were observed in DBA mice. Data are normalized to baseline and presented as mean ± [SEM/SD]; significance determined by one- or two-way ANOVA with Tukey's multiple comparisons test 92

4.5 Collagen deposition in thigh and calf muscles of DBA and mdx mice with and without treatment. **(A)** At baseline, mdx mice exhibited significantly higher collagen content compared to DBA controls, with a muscle-dependent pattern in which thigh muscle showed greater collagen accumulation than calf. **(B)** In thigh muscle, conditioned culture media (M) partially reduced collagen deposition relative to culture media (C), but did not significantly differ from untreated (U) mdx, indicating incomplete reversal of fibrosis. **(C)** In calf muscle, collagen levels were primarily driven by disease status, with no significant differences observed between treatment conditions in mdx mice. DBA mice remained low in collagen across all groups. Data represent mean ± [SEM/SD]; statistical significance determined by ANOVA with Tukey's post hoc test ($p < 0.05$). 97

B.1 Excel-generated standard curves from the three MMP-3 ELISA experiments 112

Chapter 1

Introduction and Objectives

1.1 Motivation- Duchenne Muscular Dystrophy (DMD)

Duchenne Muscular Dystrophy (DMD) is a genetic disorder caused by mutations within the *dystrophin* gene located on chromosome Xp21[1] as seen in **Figure 1.1A**, and is an X-linked recessive trait, therefore appearing almost entirely within the male population[2]. Affecting approximately 1 in 5,000 male births[3], DMD is considered one of the most severe forms of inherited muscular dystrophies. According to data obtained from the U.S. Centers for Disease Control (CDC), occurrence is most prevalent in non-Hispanic white males, representing 59.9% of diagnosed cases (**Figure 1.1B**)[4,5].

Clinically, DMD is often first suspected in children between the ages of 1 and 3[6], identified by atypical proximal limb muscle function, manifesting in difficulty with arm movement[3]. The average age of diagnosis is around 4 years old[1,3,5]. Abnormal distal limb muscle behavior exhibited in gait abnormalities can be observed shortly after, in addition to other symptoms including breathing difficulties, sleep apnea, and learning disabilities[3]. By age 12, most individuals require wheelchair assistance. DMD patient life expectancy is short, as most pass away between the ages of 20 and 30 due to cardiac and respiratory failure, stemming from the absence of dystrophin in cardiac muscle tissue[1] (**Figure 1.2**).

At the molecular level, the *dystrophin* gene, also known as the DMD gene, is the largest known gene in the human genome[1]. It spans approximately 2.5 megabases of DNA with 79 exons and 78 introns[1]. This gene produces a 14-kilobase mRNA transcript that encodes dystrophin, a 427-kilodalton cytoskeletal protein located in the plasma membrane of muscle tissues[1]. Dystrophin is critical for stability in the sarcolemma of muscle fibers and is crucial to muscle fiber structural integrity[1,7,8].

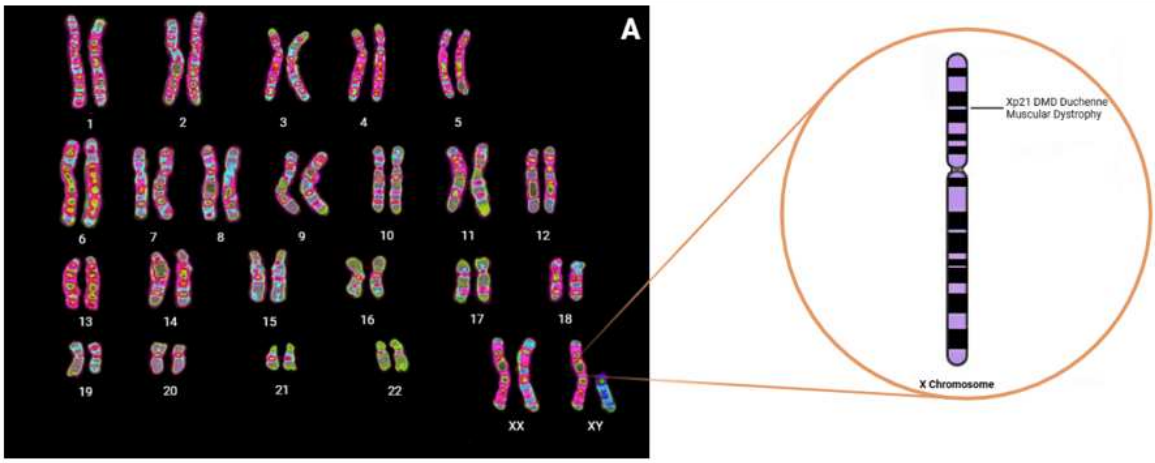

B

	n	%
Asian/Hawaiian/Pacific Islander	29	2.3%
Non-Hispanic Black	90	7.2%
Hispanic/Latino	249	19.8%
Non-Hispanic White	752	59.9%
Other*	35	2.8%
Unknown	101	8.0%

Number and percentage of males with DBMD by race/ethnicity

*Native American, American Indian, Alaskan Native, multiple, and other

Figure 1.1: (A) Illustration of the 23 human chromosomes, with location of the DMD gene on the Xp21 locus enlarged. Image modified in Biorender to show location of DMD. Note. Adapted from "The genetics of human blood," by H. L. Carson, n.d., *Encyclopædia Britannica*. Retrieved November 4, 2025, from https://www.britannica.com/science/human-genetics/The-genetics-of-human-blood. Copyright Encyclopædia Britannica, Inc. (B) Prevalence of Duchenne and Becker muscular dystrophy by race/ethnicity. Note. Adapted from [4]

Deletions in exons 3-9 and 45-55 account for approximately 60% of mutations found in DMD patients[1]. Dystrophin interacts with the dystrophin-glyco-protein complex (DGC) serving as a link between the extracellular matrix (ECM) and the cytoskeleton[8] (**Figure 1.3**). Disruption of this link due to insufficient dystrophin presence and DGC proteins in DMD results in muscle membrane fragility and permeability, allowing for degeneration and necrosis of muscle fibers[2,8]. Furthermore, dystrophin deficiency disrupts the organization of associated proteins, impairing cell signaling and exacerbating muscle fiber degeneration[1].

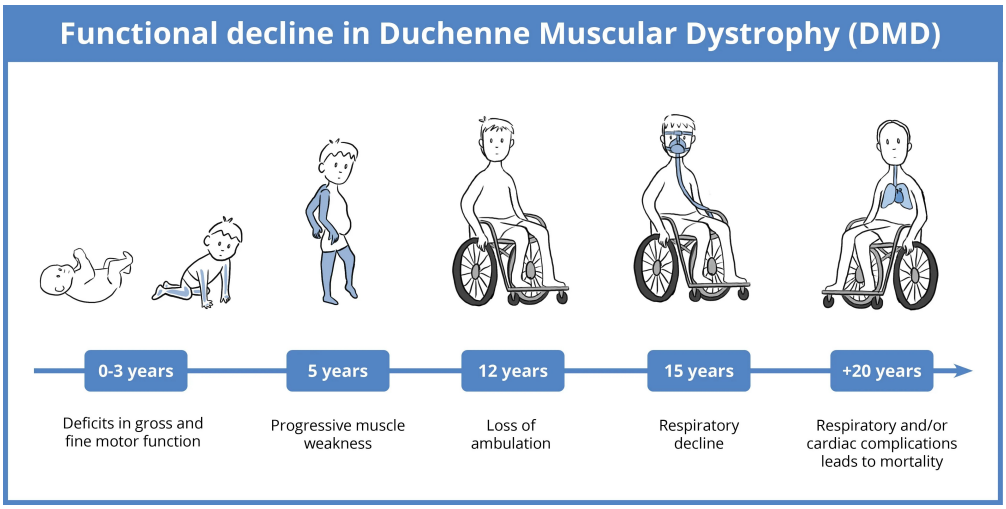

Figure 1.2: Schematic of clinical progression of DMD, including age range, body areas affected, and disease stages. Note. Adapted from "MRI biomarkers for Duchenne muscular dystrophy (DMD)," by E. Laurie & B. J. Bedell, 2025, *Biospective*. https://imaging-cro.biospective.com/resources/mri-biomarkers-duchenne-muscular-dystrophy. Copyright 2025 by Biospective Inc.

1.1.1 Injury Remodeling and Fibrosis in DMD

Immune cell infiltration often precedes clinically observable symptoms and is strongly correlated with DMD severity[1]. Immune cells play a critical role in skeletal muscle maintenance and repair. Upon injury, there is an initial influx of neutrophils and pro-inflammatory (M1) macrophages, which begin clearing damaged muscle fibers[1]. This is followed by a transition to anti-inflammatory macrophages (M2), which begin to promote fiber regeneration and fibrosis, supported by regulatory T-cells such as Foxp3+ Treg[1].

In contrast, initial immune cell infiltration in individuals with DMD is predominantly formed by both M1 and M2 macrophages and an early appearance of T-cells[1]. These findings are supported by results in studies performed on dystrophin deficient murine muscles[1]. This dysregulated pro- and anti-inflammatory signaling results in a chronic inflammatory response that creates lesions incapable of quick healing, further perpetuating muscle damage[1]. Over time, the diminished regenerative capacity and the sustained inflammation in dystrophic muscle leads to excess development of fibrotic tissue that is incapable of self-resolution[1].

The sustained chronic inflammatory response in DMD, marked by an imbalance between M1 and M2 macrophages, leads to increased expression of transforming growth factor-beta (TGF-β), a

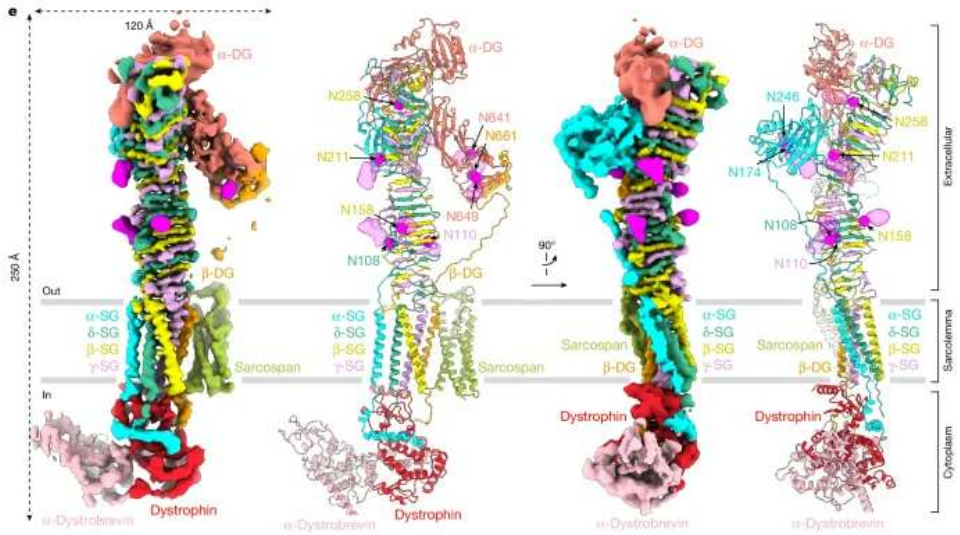

Figure 1.3: Cryo-EM structure of native dystrophin-glycoprotein complex. This figure visualizes the relationship between the cytoplasm, DGC, sarcolemma, and the ECM. Note. Adapted from "Native DGC structure rationalizes muscular dystrophy-causing mutations," by S. Liu, T. Su, X. Xia, & Z. H. Zhou, 2024, *Nature*, 637(8006), 1261–1271. https://doi.org/10.1038/s41586-024-08324-w. Copyright 2024 by Springer Nature.

key regulator of ECM deposition[9]. This upregulation triggers excessive production of extracellular fluid containing fibronectin, glycosaminoglycans, and proteoglycans, and overstimulates myofibroblasts, resulting in the overproduction of ECM proteins include type I and type III collagen, as well as fibronectin[1,9]. Combined with dystrophin deficiency which impairs proper muscular remodeling, these processes contribute to the development of muscular fibrosis in DMD patients[10].

Fibrosis is defined as the aberrant deposition of ECM components due to the body's inability to maintain muscular homeostasis[10]. While ECM typically comprises about 5% of healthy muscle tissue, its levels are shown to be significantly elevated in diseased or injured muscle models, reaching ~20%[1,11]. Increased deposition of ECM components– including collagen, fibronectin and gelatin– further prevents proper tissue function and healing, creating a positive feedback loop that results in limited mobility and reduces the amount of healthy muscle tissue available for therapeutic interventions[1,7,10]. Because fibrotic tissue development begins early in individuals with DMD, treatments targeting the reduction or resolution of fibrosis are desired in DMD treatment strategies[1].

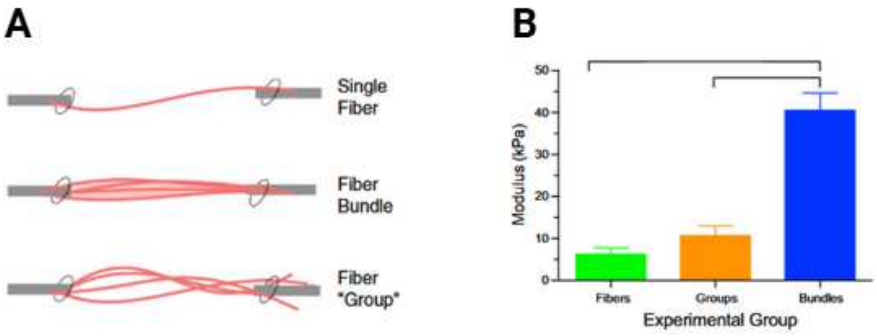

Figure 1.4: (A) Schematic illustration of the arrangement of 3 specimen types. Single fibers (curved pink lines) were isolated from the muscle and tested individually or secured in groups. Bundles of a similar number of fibers embedded in ECM (light pink) were isolated and similarly secured (B) Normalized stiffness of fibers, fiber groups, and fiber bundles. Fiber bundles have a significantly higher modulus than either individual fibers or fiber groups, demonstrating that the ECM provides a large fraction of the loadbearing. Fiber and fiber group moduli were not significantly different from each other. Connecting bars represent significant differences ($P < 0.05$). Note. Both A and B reprinted from [11]

There are over 20 types of collagen in the human body[12], collectively accounting for approximately 30% of total protein content[9]. Among these, collagen type I is the most abundant[12] and serves as the primary structural component of the ECM[9]. In fibrotic tissue, collagen levels in fibrotic tissue can exceed those in healthy tissue by more than 100-fold[9].

Within skeletal muscle, the responsibility of passive load bearing primarily falls to the interstitial collagen within the ECM[9,11,13]. This has been demonstrated in studies comparing the normalized stiffness of isolated muscle fibers, fiber bundles with intact ECM, and bundles with disrupted ECM (**Figure 1.4A**)[11]. By assessing viscoelastic properties in skeletal muscle through incremental stretching and measuring force and cross-sectional area, researchers found that bundles with intact ECM exhibited significantly higher stress (**Figure 1.4B**)[11]. These findings support the conclusion that the ECM is largely responsible for loadbearing, with a modulus of up to 25 times greater than that of muscle cells alone, despite comprising only 5-10% of the cross-sectional area[11,14].

In DMD patients, the proportion of ECM in skeletal muscle can increase up to 10-fold, resulting in markedly increased muscle stiffness[11]. Measurements of fibrotic wound tissue using atomic force microscopy (AFM) indicate an elastic modulus (E) ranging from approximately 20 to 60

kPa[15]. These values exceed the stiffness of typical soft tissues and overlap with those of cartilage and precalcified bone, as illustrated in **Figure 1.5A**[15].

A study comparing the stiffness of dissected extensor digitorum longus (EDL) muscles from wildtype (DBA) and dystrophin deficient (mdx) mice revealed significantly higher stiffness in mdx muscles (EDL: WT: 156.65 $\pm$ 42.27 kPa, mdx: 330.85 $\pm$ 127.46 kPa, P = 0.0001;) (**Figure 1.5B**)[14]. This same study related mechanical properties to a quantification of collagen presence in the EDL muscles, as well as the soleus (calf, SOL) muscle[14]. While collagen levels in the EDL did not differ significantly between groups, the soleus muscle in mdx mice showed a notable increase (**Figure 1.5C**), supporting the hypothesis that increased stiffness in muscles may be attributed to collagen presence and organization[12,14]. Additionally, the increase of the muscle microenvironment stiffness resulting from excess ECM component presence in fibrotic conditions generates a positive feedback loop, further stimulating TGF-β1 and enhancing fibrogenesis[9].

The assembly and hierarchical architecture of the ECM plays a crucial role in wound healing and the progression of fibrotic tissue[13]. The ECM network primarily constructed by fibroblasts, which deposit fibronectin fibers in a mechanoregulated manner[13]. Fibronectin is secreted by fibroblasts as a disulfide-bonded dimer, composed of three repeating modules that facilitate interactions with cells and other ECM components, such as collagen[16]. The polymerization of fibronectin is cell-dependent and requires interactions with integrin receptors[16]. These interactions induce a conformational change in fibronectin, exposing binding sites that enable fibronectin-fibronectin polymerization **Figure 1.6A**[16].

Literature review largely supports that fibronectin and its polymerization precedes and regulates the deposition of type I and III collagen[12,17,18,19]. The binding interaction between fibronectin and collagen types I and III has been well-documented. The collagen binding site is located at the 3/4–1/4 mammalian collagenase cleavage site[16,19], while the fibronectin binding site resides within a 40-kDa region near its amino terminus (**Figure 1.6A**)[12,20]. Specifically, the a1 chain of collagen type I binds to fibronectin's gelatin-binding domain (**Figure 1.6A**), a critical interaction for initiating collagen deposition[13]. *In vivo*, collagen type I assembly is cell-mediated and requires

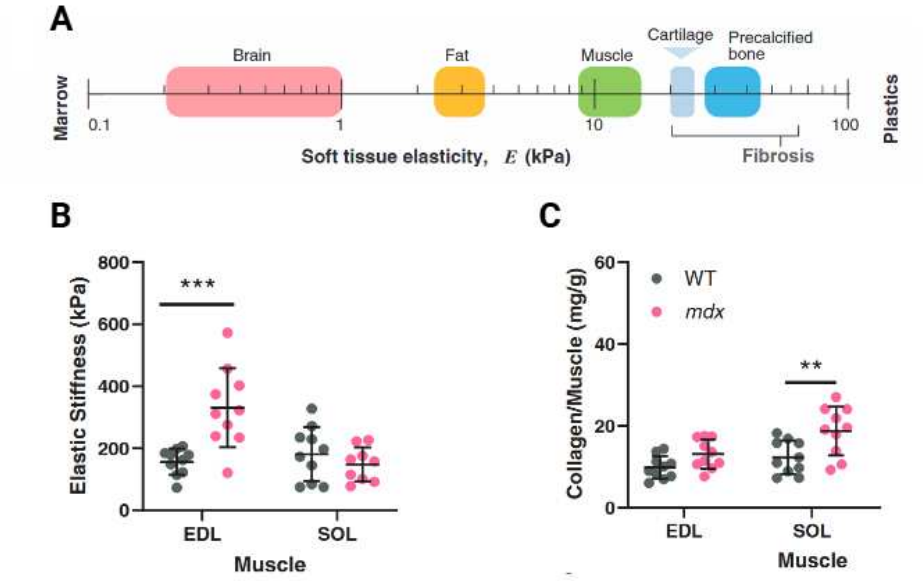

Figure 1.5: (A) Soft tissue elasticity scale ranging from soft brain, fat, and striated muscle to stiff cartilage [E ~20 to 30 kPa at the scale of adhesions] and precalcified bone. Note. Adapted from [15]. (B) Muscle size and mechanical properties from wildtype (n = 10; 5M/5F) and mdx (n = 10; 5M/5F) mice. Elastic stiffness taken as the elastic modulus at 10% strain shows the mdx EDL is significantly stiffer than the wildtype EDL. The soleus had similar stiffness between genotypes. (C) Collagen content and solubility, determined through a hydroxyproline assay, and its relation to passive mechanics. The amount of collagen per muscle in wildtype and mdx muscles. The soleus muscle collagen content of mdx mice was significantly increased compared with the wildtype (n = 6 wildtype; n = 8 mdx). Note. Figures B and C adapted from [14]

active fibronectin fibrillogenesis[13]. However, the precise mechanisms by which fibronectin fibrils direct collagen fiber deposition remain unclear, and a hypothetical model is illustrated in **Figure 1.6B**[13]. Despite this gap in understanding, the fibronectin-collagen interaction is also known to be essential for myofibroblast migration[17] and cell migration[20].

Several studies have been conducted to confirm and further investigate the fibronectin-collagen relationship. One such study explored the use of binding antibodies targeting the collagen-binding site on fibronectin, which resulted in the inhibition of collagen fibrillogenesis[16]. Other studies involved either removing fibronectin entirely or inhibiting its polymerization, with findings showing that collagen I fibrils were not deposited into the ECM, despite the presence of soluble collagen I[18,12]. In the same study, inhibition of fibronectin deposition into the ECM led to the turnover of

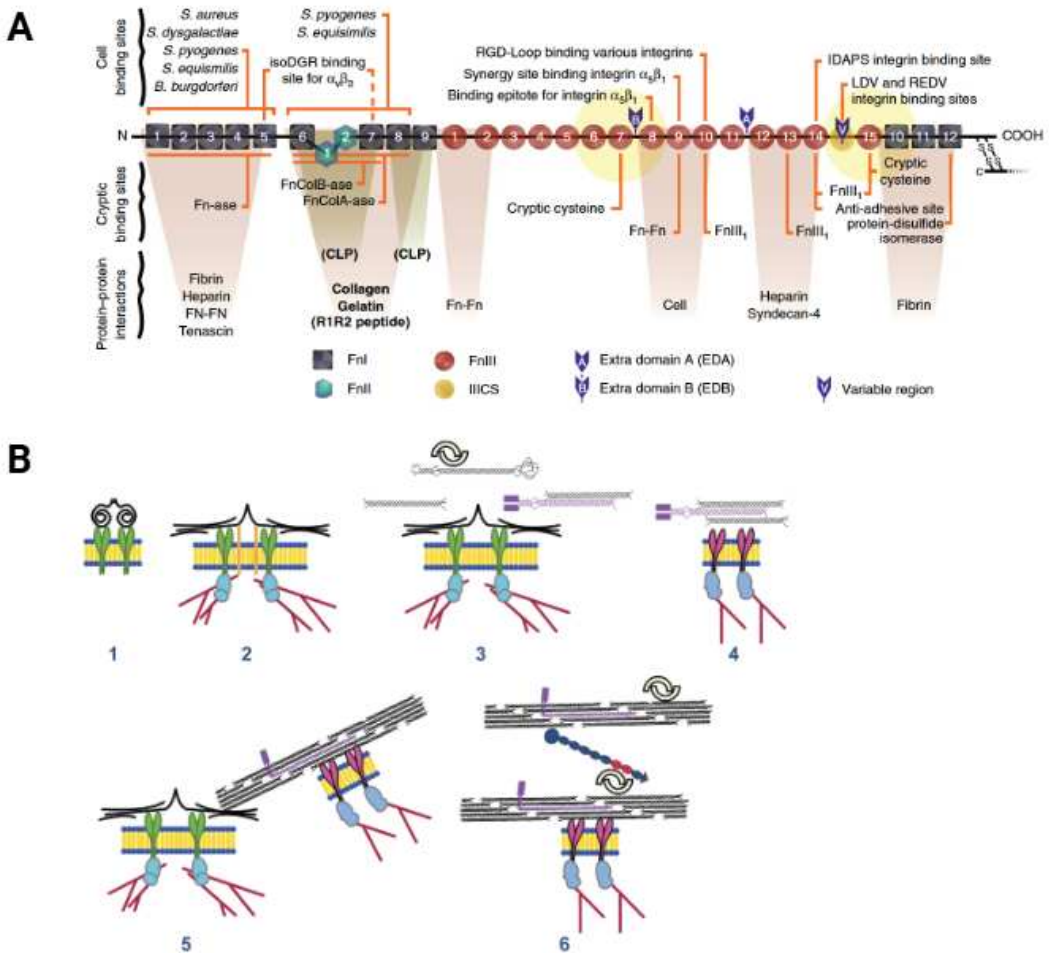

Figure 1.6: (A) Diagram of a FN monomer showing binding and interaction sites. Fn exists as a dimer of two nearly identical monomers, linked at the C-terminus by disulfide bonds. The yellow circles show the 6 nm Forster energy transfer radius for the acceptor dyes that are located on modules FnIII7 and FnIII15 in FRET-labelled Fn. While the FRET radii are drawn roughly to scale to indicate which modules are covered, other aspects of the diagram are not necessarily to scale. The canonical collagen/gelatin-binding domain, the R1R2 bacterial-adhesin-derived peptide, and the two binding sites for a CLP encompassing the Fn-binding domain of the collagen I $\alpha 1$ chain are shown in bold. (B) Hypothetical model of collagen fibril nucleation at the plasma membrane. (1) Dimeric FN (black) binds to $\alpha 5\beta 1$ integrins (green). (2) Engagement of the integrin with the cytoskeleton (red lines) causes a conformational change in FN with subsequent fibril formation. Additional receptors (orange bars) bind FN. (3) Collagen I, procollagen I (black), and collagen V (purple) engage with FN at the fibril surface to facilitate collagen fibril formation. Decorin (interlocking dimers) shown bound to procollagen. (4) Activated collagen integrins (e.g. $\alpha 2\beta 1$) bind collagen and induce a conformation change that facilitates fibril formation. (5) Collagen fibril formation at the cell surface. (6) Interactions between collagen fibrils determine fibril diameter, organization, and spacing. Note. (A) Adapted from [13]; (B) Adapted from [16].

both fibronectin and collagen I fibrils[18], further emphasizing the essential role of fibronectin in collagen matrix assembly.

Additional studies have further elucidated the fibronectin-collagen relationship, revealing that fibronectin initially provides tension-bearing support within the ECM until it is gradually superseded by increasing collagen content[13]. This demonstrates a reciprocal mechanoregulation within the ECM where collagen I fiber organization is initially guided by fibronectin, but as collagen fibers mature, they assume the primary role in stabilizing tissue against tensile forces[13]. Moreover, the load bearing capabilities previously discussed are largely attributed to collagen-fibronectin binding interactions[13].

Based on these findings, it is reasonable to conclude that regulating fibronectin deposition in fibrotic disease models may limit collagen deposition, thereby reducing the formation of fibrotic tissue. This insight presents a promising therapeutic avenue for managing fibrosis in conditions such as DMD.

1.1.2 Matrix Metalloproteinases (MMPs)

The structure and maintenance of the ECM is mediated by several enzymes, most notably the matrix metalloproteinases (MMPs)[21]. The human genome encodes 24 zinc-dependent MMPs, each with distinct functions and activation cascades[22]. Some MMPs rely on one another for processing and directing cytokines, chemokines, cell receptors and growth factors[17,21,22]. MMPs are classified based on their substrate specificity, structural domain organization[23], and ECM component degradation profiles[24]. The catalytic activity and degradative capabilities of each MMP correlate with its classification[22] and can be seen in **Table 1.1**.

Despite their different classifications, all MMPs share a similar core structure. Each MMP typically contains an 80-amino-acid propeptide domain, a 170-amino-acid catalytic metalloproteinase domain that includes a zinc ion, and a 200-amino-acid hemopexin domain (**Figure 1.7A**)[22,23]. While some structural variations exist (e.g., matrilysins lack the hemopexin domain), the overall architecture remains consistent across the MMP family[22].

Table 1.1: MMP Classification and Degradative Capabilities

Classification	MMPs	Degradative Targets
Collagenases	1, 8, 13, and 18	Triple-helical fibrillar collagens
Gelatinases	2 and 9	Basal lamina
Stromelysins	3, 10, 11, and 19	Fibronectin, other ECM components
Matrilysins	7 and 26	Most ECM components
Membrane-type (MT)-MMPs	14, 15, 16, 17, 24, and 25	Most ECM components
Enamelysins	20 and 21	Dental components
Others	12, 23, 27 and 28	Macrophages, lungs, intestine

MMP enzymes are secreted as inactive precursors known as zymogens, or pro-MMPs (**Figure 1.7B**)[22]. Activation requires the removal of the propeptide domain, which enables their enzymatic activity[22]. The regulation of MMP activity is tightly controlled by the binding of tissue inhibitors of metalloproteinases (TIMPs) (**Figure 1.7B**)[22,25]. Both pro-MMPs and TIMP-MMP complexes are enzymatically inactive and incapable of catalysis, meaning that only activated MMPs possess degradative abilities[22]. MMPs play a critical role in ECM regulation and turnover, as well as in tissue signaling, and are essential for maintaining tissue and organismal homeostasis[21]. Dysregulation of ECM remodeling can lead to uncontrolled cell proliferation, cancer, and tissue fibrosis, as observed in DMD[22]. Therefore, precise regulation of ECM components and their modulators is vital for effective fibrotic tissue repair[17].

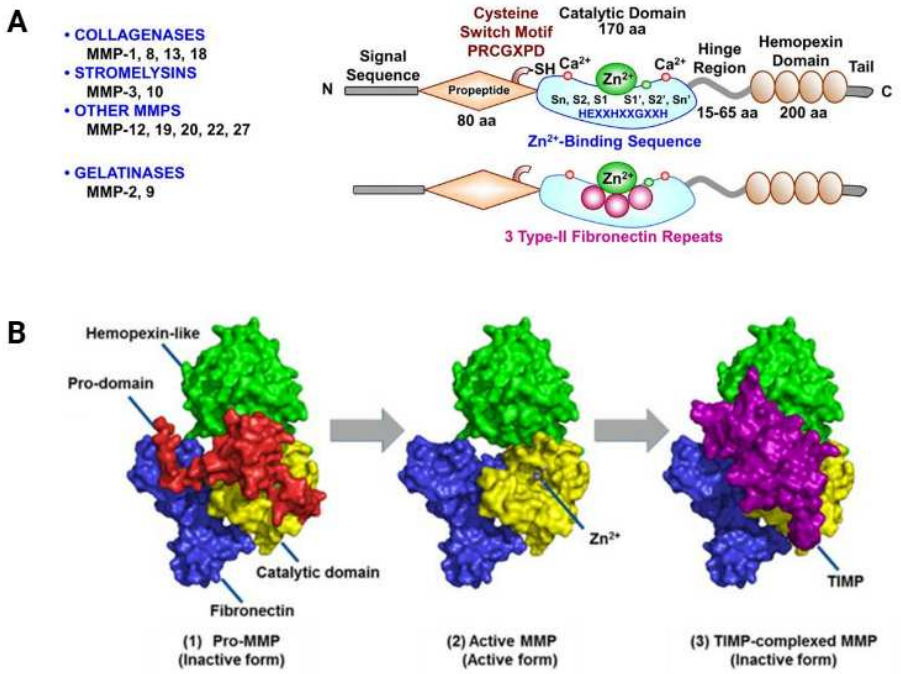

Figure 1.7: (A) Major MMP subtypes and structures. A typical MMP consists of a propeptide, a catalytic domain, a linker peptide (hinge region), and a hemopexin domain. The propeptide has a cysteine switch (PRCGXPD) whose cysteine sulfhydryl (–SH) group chelates the active site Zn^{2+}, keeping the MMP in the latent proMMP zymogen form. The catalytic domain contains the Zn^{2+} binding motif HEXXHXXGXXH, two Zn^{2+} ions (one catalytic and one structural), specificity conferring 'S-pockets', and two or three Ca^{2+} ions for stabilization. Some MMPs show exceptions in their structures. Gelatinases have 3 type-II fibronectin repeats in the catalytic domain. Note. Adapted from [23] (B) The three forms of MMPs as illustrated in MMP-2. MMPs are made as inactive zymogens or proMMPs. They are activated by removal of the propeptide domain. MMPs are regulated primarily by complexation with TIMPs. Note. Adapted from [22]

1.1.3 Current Therapies for Muscle Fibrosis

Treating fibrotic tissue becomes increasingly challenging as fibrosis progresses, primarily due to the limited availability of healthy muscle required for effective therapeutic interventions[7]. The ability to identify and utilize healthy muscle to support the treatment and healing of surrounding fibrotic tissue remains a significant obstacle in current therapeutic approaches[7].

Glucocorticosteroids are currently the primary treatment for individuals with DMD, although their mechanisms of action are not yet fully understood[1]. It is believed that their therapeutic effects, such as increased muscle mass and strength, are results from the stimulation of insulin-like growth

factors, leading to reduced inflammation, dampened lymphocyte activity, and decreased cytokine production, along with enhanced myoblast proliferation[1].

Viral gene therapy is another possible intervention, aiming to restore functional dystrophin levels by replacing the defective gene copy with a healthy one, reestablishing normal dystrophin expression throughout the body[1]. However, challenges include the large size of the dystrophin gene and the difficulty of achieving systemic delivery to all striated muscles[1].

Exon-skipping therapy is another investigational strategy that attempts to restore the disrupted open reading frame of dystrophin transcripts. By skipping defective exons, this method enables the production of a partially functional, internally truncated dystrophin protein[1]. Despite its potential, exon therapy is complex and costly, with limitations including delivery efficiency and variability in drug-induced dystrophin production[1].

Cell-based therapeutics have been explored as a treatment strategy for DMD, including the transplantation of genetically engineered induced pluripotent cells derived from the host. These cells contain functional dystrophin and are introduced into dystrophin-deficient muscle tissue[1]. While this approach carries a lower immunogenic risk, it is expensive, labor intensive, and not considered a long term-solution[1]. Other cellular therapies have investigated the use and modification of various cell types, including bone marrow-derived cells, pericytes, mesoangioblasts, and mesenchymal stromal/stem cells (MSCs). These cell types are considered ideal due to their ability to access the muscle compartments and their myogenic potential[1].

1.2 Mechanobiology Engineering MSCs

1.2.1 Mesenchymal Stromal Cells

Mesenchymal stromal/stem cells (MSCs) were first described in 1967 by Friedenstein as spindle-shaped, adherent, non-hematopoietic stem cells resident in the bone marrow[21]. There has been ongoing debate regarding whether mesenchymal stromal cells and mesenchymal stem cells are the same. While many reputable sources support their equivalence[26,27], others highlight distinct differences between the two[27], leaving the question unresolved. Despite this uncertainty, the ma-

jority of current literature suggests that both terms refer to the same cell population but emphasize different aspects: the stem-like properties versus their supportive and modulatory roles within the tissue environment[27]. In response to this ambiguity, the International Society for Cellular Therapy (ISCT) issued a statement recommending that functional definitions be used to clarify whether the MSC acronym stands for "mesenchymal stem cell" or "mesenchymal stromal cell" and that unfractionated populations be referred to as stromal cells, given their low frequency of stem/progenitor cells[28]. Therefore, in the context of this project, MSCs will refer specifically to mesenchymal stromal cells, in alignment with ISCT guidelines.

No specific surface markers have been universally identified for MSCs. However, the ISCT has established a set of minimal criteria to define MSCs[21,29]:

- Plastic adherence under standard culture conditions
- Positive expression of surface markers: Sca-1, CD44, CD71, CD73, CD90, CD105
- Negative expression of hematopoietic and endothelial markers: CD11b, CD19, CD31, CD34, CD45
- Multipotency, demonstrated by the ability to differentiate *in vitro* into various mesodermal lineages, including osteocytes, adipocytes, chondrocytes, and muscle cells under appropriate growth conditions

MSCs represent only a minor fraction of the cellular population in bone marrow, but they can be readily isolated and expanded *in vitro*. In addition to bone marrow, MSCs can also be obtained from various other tissues, including the umbilical cord wall, blood, placenta, adipose tissue, lung, liver, and skin (**Figure 1.8**)[21,29].

Multipotency differentiation by MSCs occurs through a two-step process. The first step is commitment, during which lineage-specific progenitor cells are generated. This phase continues until the second step, maturation, where the progenitor cells undergo transformation into terminally differentiated cells[21].

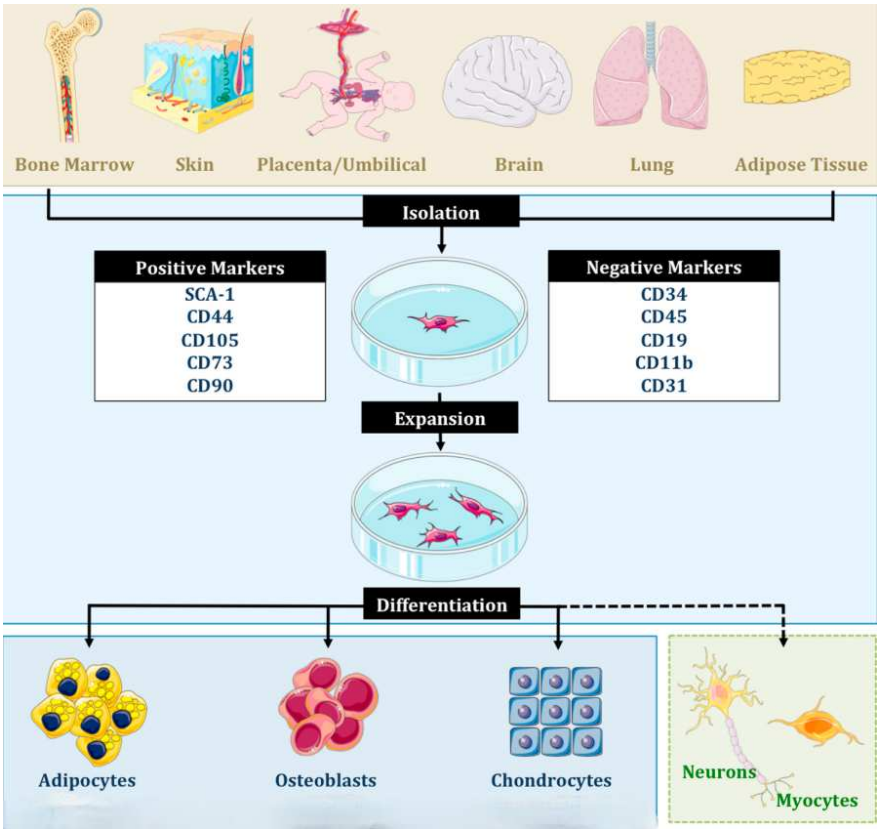

Figure 1.8: MSC isolation, expansion, differentiation and niche. MSCs can be isolated from various tissues. Upon isolation, MSCs may be expanded and enriched by *in vitro* passaging. A combination of positive and negative markers can be used to determine MSC purity. These cells can undergo differentiation *in vitro*, generating adipo, osteo, and chondrocytes, in addition to neurons and myocytes. Note. Adapted from [21]

In vivo microenvironmental characteristics, such as the ECM, mechanical forces, and cell shape, play a crucial role in determining MSC fate decisions[21]. Environmental signals from the MSCs' surroundings significantly influence their behavior, with the ECM serving as a primary source of these regulatory cues[21]. Numerous studies have investigated how MSCs sense and respond to signals from the ECM at the molecular level, ultimately guiding their differentiation and function[21]. These studies also demonstrate that MSC interactions with their surrounding microenvironment are reciprocal: MSCs can remodel their surroundings in response to the chemical and mechanical cues they receive from them[30]. This dynamic interplay is a central concept in mechanobiology, the study of how biological systems, such as cells, tissues and organs, sense and respond to mechanical stimuli to regulate processes including development, differentiation, physiology, and disease[31]. The secretome produced by MSCs in response to their microenvironment

can, in turn, alter the properties of that environment, further influencing cell behavior and tissue outcomes[29].

The MSC secretome contains a wide array of bioactive molecules that play a significant role in tissue repair strategies[29]. It consists of two main components: a soluble fraction, which includes growth factors, chemokines, cytokines, hormones, cell adhesion molecules, and interleukins; and a vesicular fraction, which carries RNAs, lipids, proteins, and DNA[29]. These factors exert regenerative and reparative effects primarily through paracrine signaling, facilitating cell-to-cell communication[29]. This signaling is crucial for adaptive and innate immunomodulation, angiogenesis, anti-cancer activity, and tissue protection[29]. MSC ability to exert paracrine effects is considered one of the key mechanisms underlying the therapeutic efficacy of MSC-based cell therapies[29].

Studies have shown that transplanted MSCs typically persist for only about 48 hours[32]. This suggests that therapeutic benefits are largely attributed to the angiogenic, immunomodulatory, antioxidative, and anti-apoptotic effects of the secreted growth factors, chemokines and cytokines, rather than direct differentiation or cell replacement[29]. Moreover, MSCs actively contribute to tissue repair and homeostasis by modulating the local environment, reducing inflammation and, depending on surrounding tissue characteristics, differentiating into other cell types[29]. The release of exosomes containing mRNA, protein, and microRNAs further enhances cell proliferation and reduces inflammation during tissue regeneration[29]. The relationship between MSCs and the innate immune system stimulates both pro- and anti-inflammatory responses, highlighting the immunoregulatory capabilities of MSCs[29]. These properties make MSCs great candidates for the treatments of various diseases.

1.2.2 Overview of Current MSC Therapy Clinical Trials

In 1995, Hillard Lazarus performed the first cell therapy using MSCs. Since then, stem cell therapy has been widely investigated as a potential method of treatment for graft-versus-host disease, malignant neoplasms, cardiovascular diseases, immune system disorders, and neurological conditions[29]. MSC-based tissue repair has shown promise due to several advantages, including

autologous transplantation, safe cellular division, and a low risk of teratoma formation[29]. According to the U.S. National Institutes of Health Clinical Trials database, 416 clinical trials involving MSCs were conducted between 2015 and 2022. As of 2022, 55 were active but not recruiting, 233 were recruiting, 117 were completed, 11 were terminated (**Figure 1.9A**)[29]. The United States and China are leading in the number of MSC-related clinical trials, with additional contributions from other countries[29]. An updated figure (**Figure 1.9B**), generated using data from the same source as of October 2025, represents approximately 293 clinical trials.

Discrepancies and mixed outcomes in MSC-based clinical trials have highlighted the need for a better control and consistency in therapeutic applications. One potential approach involves using mechanobiology to tailor the microenvironment surrounding MSCs, thereby influencing their behavior and promoting desired therapeutic outcomes. Previous studies support the use of mechanobiological strategies to enhance protein secretion from MSCs. For example, significant differences were observed in MSC responses to microenvironments of varying stiffness, created using alginate hydrogels crosslinked with $CaSO_4$ to produce tunable stiffness levels[33]. As shown in **Figure 1.10**, MSCs encapsulated in "soft" and "stiff" hydrogels and cultured in the presence of the inflammatory factor TNF-α exhibited increased secretion of proteins CCL2 and IL-6, with the "soft" hydrogel eliciting a significantly greater response than the "stiff" hydrogel[33]. This study, along with others[34,35,36], demonstrates the viability of a mechanobiological approach to enhance the therapeutic potential of MSCs by modulating their microenvironment.

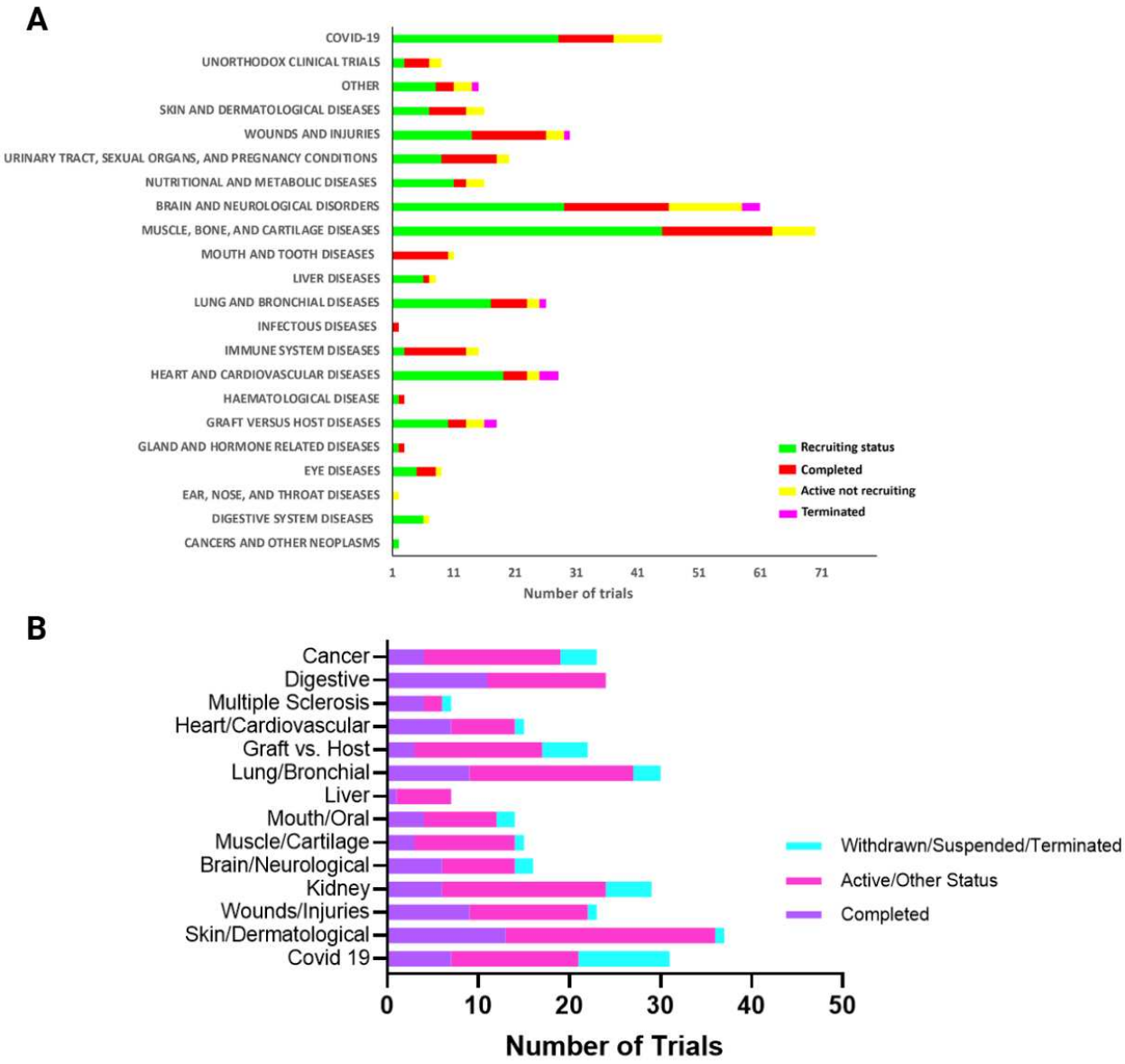

Figure 1.9: (A) MSC clinical trials classified by disease categories subdivided by progress status: in green, "Recruiting Status"; in red, "Completed"; in yellow, "Active not recruiting"; in magenta, "Terminated". The 22 shown categories account for >90% of the trials reported on clinicaltrials.gov from 2015 to present. Note. Reprinted from [29] (B) MSC clinical trials classified by disease categories and subdivided by progress status: in blue "Withdrawn/Suspended/Terminated"; in pink "Active/Other"; in purple "Completed", representing ~293 trials as of October 2025. Information sourced from ClinicalTrials.gov, visualized using GraphPad Prism.

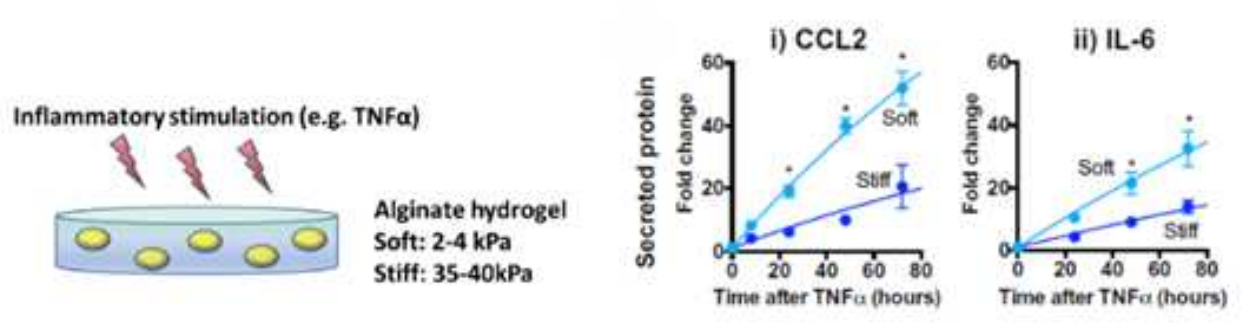

Figure 1.10: 3D matrix stiffness regulates expression of TNF-α-inducible genes implicated in monocyte functions. Effects of 3D matrix stiffness on protein secretion kinetics in response to TNF-α. Data were fitted to standard one-phase association curves. (i) CCL2: t1/2 = 126 hours for both soft and stiff; plateau for soft = 156-fold and for stiff = 61-fold. (ii) IL-6: t1/2 = 204 hours for both soft and stiff; plateau for soft = 143-fold and for stiff = 58-fold. Fold change refers to increase over untreated condition. Note. Adapted from [33].

1.3 Alginate

Alginate is a naturally occurring anionic polymer, typically derived from brown seaweed or algae, and is valued for its biocompatibility, low toxicity, cost-effectiveness, and ease of gelation, qualities that make it ideal for a wide range of biomedical applications[37]. Once formed into a hydrogel, alginate exhibits structural similarities to the ECM of living tissues, enabling its use in wound healing, drug delivery, cell transplantation and other therapeutic applications[37]. Alginate hydrogels possess tunable properties that allow for minimally invasive injection and implantation, further expanding their clinical potential[37]. Additionally, the ability to modulate characteristics such as stiffness and porosity, combined with cell encapsulation, enables researchers to tailor cell behavior, deliver cells to targeted sites, support new tissue formation, and control the structure and function of engineered tissues[37].

1.3.1 General Alginate Properties

Commercially available alginate is typically extracted from brown seaweed or algae through treatment with aqueous sodium hydroxide alkali solutions[37]. The extract is then filtered, and alginate is precipitated by adding either sodium chloride or calcium chloride. The resulting alginate

salt is converted into alginic acid via hydrochloric acid treatment and subsequently purified for commercial use[37].

Alginate is composed of unbranched polysaccharide chains made up of two uronic acid monomers: mannuronic acid (M), and guluronic acid (G) (**Figure 1.11A**). The arrangement of these monomers, whether in consecutive M residues (M-blocks), consecutive G residues (G-blocks), or alternating M and G residues (MG-blocks) (**Figure 1.11B**), can significantly influence the physical properties and chain length of alginate. The overall composition of alginate varies depending on the source material from which it is extracted[37,38].

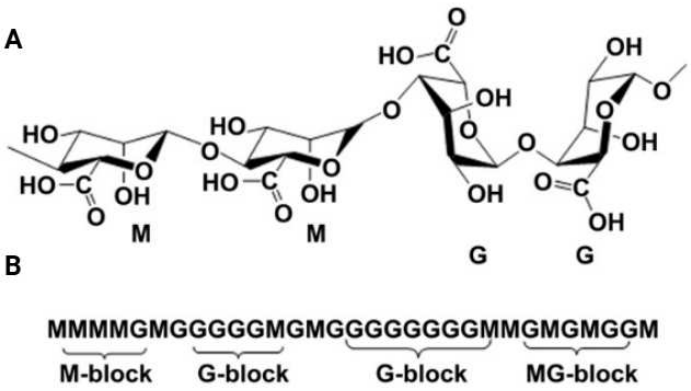

Figure 1.11: Representative alginate structure: (A) chain conformation and (B) block distribution. Note: Adapted from [38]

It is believed that only G-blocks within alginate participate in intermolecular cross-linking, typically achieved through the addition of divalent cations, such as calcium[37,38]. As a result, G-block content, length, and molecular weight are critical factors influencing the physical properties of alginate and the composition of resulting hydrogels[37,38]. Alginate with a higher G-block content generally exhibits a larger molecular weight[37]. Commercially available alginate has a wide range of molecular weights, typically between 32,000 to 400,000 g/mol[37]. While increased molecular weight and longer alginate chains can enhance the stability of the resulting gels, they also contribute to higher viscosity, which can lead to greater shear forces during mixing and injection[37]. Additionally, the post-gelation stiffness of alginate hydrogels is largely dependent on both molec-

ular weight and G-block content, due to their role in crosslinking[37]. Many properties of fabricated hydrogels, including gel stability, drug delivery and release, and behavior of encapsulated cells, can be tuned by adjusting these parameters[37,38].

Alginate has been studied in both *in vitro* and *in vivo* settings. Discrepancies in its immune response are largely attributed to alginate purity[37]. Impurities such as heavy metals, endotoxins, proteins, and polyphenolic compounds can potentially trigger an immune reaction[37]. However, studies using highly purified alginate have shown no significant foreign body reaction or inflammatory response when introduced an *in vivo* environment[37].

Alginate degradation via polymer chain cleavage requires alginase enzymes, which are not naturally present in mammals[37]. However, ionically cross-linked alginate gels can undergo gel disintegration through ion exchange reactions, where divalent cations (e.g., calcium) are replaced by monovalent cations such as sodium ions[37]. Complete biosorption *in vivo* depends heavily on both the type of crosslinker used and the molecular weight of the alginate, as the renal clearance threshold is lower than the molecular weights of many alginate formulations[37]. Therefore, careful consideration of these two variables is essential when selecting the appropriate type of alginate for *in vivo* therapeutic applications.

1.3.2 Hydrogel Creation

To create hydrogels from alginate, divalent cations such as calcium must be added. The "egg-box" model, first introduced in the early 1970s, explains the structure of the alginate gel network. It illustrates the cross-linking interaction between calcium ions and the guluronic acid (G) blocks in alginate, resulting in a gel structure that resembles eggs nestled in a carton (**Figure 1.12A**)[37,39].

The selection of a divalent ion for cross-linking is just as important as the choice of the alginate polymer, as differences in ion solubility and composition significantly affect gelation properties and degradation behavior. Calcium sulfate ($CaSO_4$) (**Figure 1.12B**) and calcium carbonate ($CaCO_3$) (**Figure 1.12C**) are commonly used in hydrogel fabrication due to their low solubility, which helps slow the gelation rate. This extended working time allows for more uniform gel for-

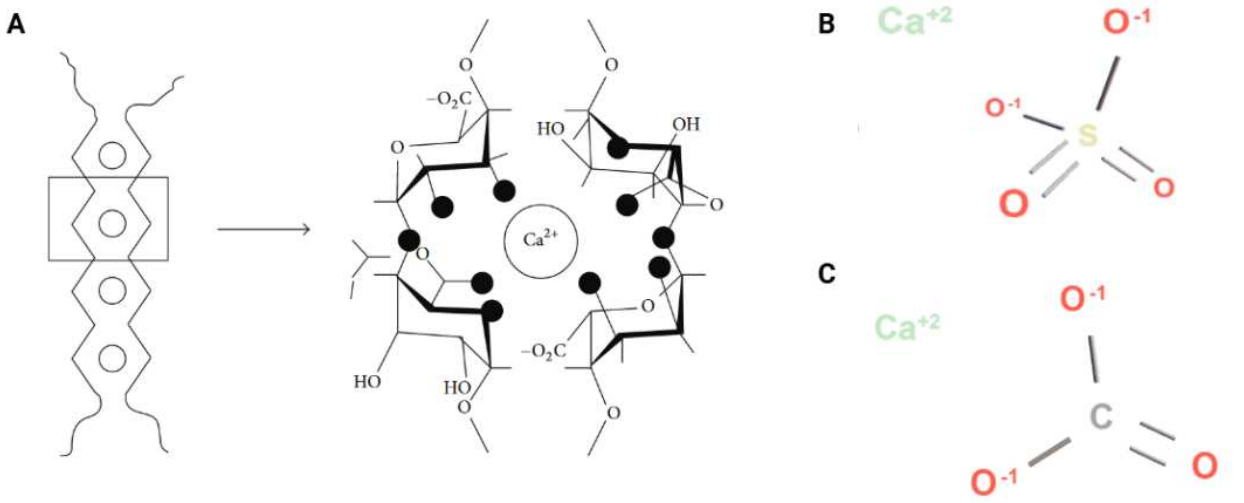

Figure 1.12: (A) Schematic drawing and calcium coordination of the "egg-box" model, as described for the pair of guluronate chains in calcium ALG junction ones. Dark circles represent the oxygen atoms involved in the coordination of the calcium ion. Note. Adapted from [39] (B) Molecular structure of anhydrous Calcium sulfate ($CaSO_4$) (C) Molecular structure of calcium carbonate ($CaCO_3$) Note. B and C rendered in Webqc.org

mation, resulting in improved mechanical integrity[37]. Additionally, the concentration of calcium ions within an alginate hydrogel can be adjusted to tune its mechanical properties, particularly stiffness, as higher calcium concentrations lead to increased cross-link density[37].

The need for a bioinert environment that supports nutrient transport and mimics biological tissue is well addressed by alginate. Its tunable mechanical properties make alginate an excellent candidate for MSC encapsulation, as modifying the microenvironmental characteristics can elicit specific, desired responses from the encapsulated MSCs.

1.4 Research Objectives

Inspired by prior mechanobiological studies, this project investigates how mechanical cues within the cellular microenvironment can be harnessed to enhance matrix metalloproteinase secretion by mesenchymal stromal cells. Specifically, this project focuses on modulating microenvironmental stiffness to stimulate MMP production, building on evidence that mechanical properties of the ECM significantly influence cellular behavior. MMPs are critical enzymes responsible for

ECM remodeling, and their upregulation may facilitate the degradation of excessive ECM components, such as collagen, fibronectin, and gelatin, that accumulate during muscle fibrosis, often resulting from repeated injury and impaired tissue regeneration.

To explore this, MSCs will be encapsulated within tunable alginate hydrogels, allowing precise control of stiffness parameters. By systematically varying these mechanical properties, the study aims to identify conditions that optimize MMP secretion. The ultimate goal is to leverage this mechanobiological response to engineer a therapeutic MSC platform capable of modulating fibrotic environments and promoting tissue homeostasis. This approach holds promise for developing customizable treatments tailored to the severity and progression of fibrotic conditions in skeletal muscle.

1.4.1 Aims

The overall goal of this project is achieved by the following aims:

- **Aim 1** Engineer biocompatible alginate hydrogels to enhance MSC secretion of MMPs
- **Aim 2** Evaluate the therapeutic efficacy of engineered MSC secretome on rodent muscle fibrosis

1.5 Organization of the Thesis Document

The second chapter explores the mechanobiological modulation of MSC secretome production through engineered hydrogel stiffness. To establish a tunable mechanical range, acellular hydrogels were fabricated using varying concentrations of calcium sulfate, enabling the identification of “soft” and “stiff” formulations. These were mechanically characterized via rheometry to confirm their distinct stiffness profiles. MSCs were then encapsulated within the optimized hydrogels and exposed to an inflammatory stimulus to induce cytokine release. Subsequent MMP gene expression was quantified using qPCR to assess the impact of microenvironmental stiffness of MSC secretory behavior. MMP-3 levels in the surrounding culture media were quantified using ELISA to confirm upregulation.

Chapter 3 evaluates the functional activity of MMP-3 secreted by MSCs encapsulated in hydrogels, as identified in Chapter 2. The chapter describes the experimental approaches used to assess the enzymatic functionality of the engineered MSC secretome *in vitro* and determine its potential role in extracellular matrix remodeling. Although these studies did not successfully demonstrate functional MMP-3 activity under the conditions tested, the results provided important insights into the limitations of the experimental design and informed the development of subsequent studies. Collectively, this chapter establishes the groundwork for the *in vivo* therapeutic investigations presented in Chapter 4.

Chapter 4 evaluates the enzymatic functionality and therapeutic potential of the engineered MSC secretome *in vivo*. Conditioned culture media collected from MSCs encapsulated in hydrogels were injected into murine thigh muscle to assess the biological activity of secreted factors. Histological evaluation of fibronectin and collagen content in skeletal muscle was performed to establish baseline fibrotic profiles and compare them with tissues receiving conditioned culture media injections. Data were collected from untreated female wild-type (DBA) and dystrophin-deficient (mdx) mice. Trichrome staining and immunohistochemistry were performed on calf and thigh muscle sections to identify collagen and fibronectin content, respectively. Quantification of collagen and fibronectin levels provided a basis for evaluating the effects of the engineered MSC secretome on fibrotic remodeling. By integrating histological outcomes with the molecular and cellular findings presented in previous chapters, this chapter investigates the potential of mechanically tuned, inflammation-preconditioned MSCs to modulate fibrosis and support muscle regeneration *in vivo*.

Chapter 5 summarizes the progress made to date and outlines the steps to come in furthering this research project. It synthesizes findings from earlier chapters, highlighting how mechanical tuning of MSC microenvironments and inflammatory preconditioning have influenced secretome output and functional activity. Long-term goals are discussed in the context of translating this engineered MSC platform into a customizable treatment for skeletal muscle fibrosis, with potential applications in Duchenne Muscular Dystrophy and other degenerative muscle conditions.

References

[1] A. Bez Batti Angulski et al. “Duchenne muscular dystrophy: Disease mechanism and therapeutic strategies”. In: *Frontiers in Physiology* 14 (2023), p. 1183101. DOI: 10.3389/fphys.2023.1183101. URL: https://doi.org/10.3389/fphys.2023.1183101.

[2] V. Venugopal and S. Pavlakis. “Duchenne Muscular Dystrophy”. In: *StatPearls*. StatPearls Publishing, 2025. URL: http://www.ncbi.nlm.nih.gov/books/NBK482346/.

[3] Muscular Dystrophy Association. *Duchenne muscular dystrophy fact sheet*. [PDF]. Feb. 2019. URL: https://www.mda.org/sites/default/files/2019/03/Duchenne_Muscular_Dystrophy_Fact_Sheet.pdf.

[4] CDC. *Data Summary. Muscular Dystrophy*. July 2025. URL: https://www.cdc.gov/muscular-dystrophy/research/summary.html.

[5] S. Ryder et al. “The burden, epidemiology, costs and treatment for Duchenne muscular dystrophy: An evidence review”. In: *Orphanet Journal of Rare Diseases* 12.1 (2017), p. 79. DOI: 10.1186/s13023-017-0631-3. URL: https://doi.org/10.1186/s13023-017-0631-3.

[6] Muscular Dystrophy Association. *Duchenne Muscular Dystrophy (DMD)—Diseases*. Nov. 2017. URL: https://www.mda.org/disease/duchenne-muscular-dystrophy.

[7] Y. Kharraz et al. “Understanding the Process of Fibrosis in Duchenne Muscular Dystrophy”. In: *BioMed Research International* 2014 (2014), p. 965631. DOI: 10.1155/2014/965631. URL: https://doi.org/10.1155/2014/965631.

[8] R. D. Cohn and K. P. Campbell. “Molecular basis of muscular dystrophies”. In: *Muscle & Nerve* 23.10 (2000), pp. 1456–1471. DOI: 10.1002/1097-4598(200010)23:10<1456::AID-MUS2>3.0.CO;2-T. URL: https://doi.org/10.1002/1097-4598(200010)23:10%3C1456::AID-MUS2%3E3.0.CO;2-T.

[9] N. M. Dewi et al. “Targeted Therapy for Skeletal Muscle Fibrosis: Regulation of Myostatin, TGF-β, MMP, and TIMP to Maintain Extracellular Matrix Homeostasis”. In: *Biologics :*

Targets & Therapy 19 (2025), pp. 213–229. DOI: 10.2147/BTT.S508221. URL: https://doi.org/10.2147/BTT.S508221.

[10] N. C. Henderson, F. Rieder, and T. A. Wynn. "Fibrosis: From mechanisms to medicines". In: *Nature* 587.7835 (2020), pp. 555–566. DOI: 10.1038/s41586-020-2938-9. URL: https://doi.org/10.1038/s41586-020-2938-9.

[11] "Structural and functional consequences of skeletal muscle fibrosis". In: *American Journal of Physiology - Cell Physiology* 305.4 (2013). DOI: 10.1152/ajpcell.00173.2013. URL: https://doi.org/10.1152/ajpcell.00173.2013.

[12] T. Velling et al. "Polymerization of Type I and III Collagens Is Dependent On Fibronectin and Enhanced By Integrins $\alpha 11\beta 1$and $\alpha 2\beta 1$*". In: *Journal of Biological Chemistry* 277.40 (2002), pp. 37377–37381. DOI: 10.1074/jbc.M206286200. URL: https://doi.org/10.1074/jbc.M206286200.

[13] K. E. Kubow et al. "Mechanical forces regulate the interactions of fibronectin and collagen I in extracellular matrix". In: *Nature Communications* 6.1 (2015), p. 8026. DOI: 10.1038/ncomms9026. URL: https://doi.org/10.1038/ncomms9026.

[14] S. E. Brashear et al. "Passive stiffness of fibrotic skeletal muscle in mdx mice relates to collagen architecture". In: *The Journal of Physiology* 599.3 (2021), pp. 943–962. DOI: 10.1113/JP280656. URL: https://doi.org/10.1113/JP280656.

[15] D. E. Discher, D. J. Mooney, and P. W. Zandstra. "Growth Factors, Matrices, and Forces Combine and Control Stem Cells". In: *Science* 324.5935 (2009), pp. 1673–1677. DOI: 10.1126/science.1171643. URL: https://doi.org/10.1126/science.1171643.

[16] K. E. Kadler, A. Hill, and E. G. Canty-Laird. "Collagen fibrillogenesis: Fibronectin, integrins, and minor collagens as organizers and nucleators". In: *Current Opinion in Cell Biology* 20.5 (2008), pp. 495–501. DOI: 10.1016/j.ceb.2008.06.008. URL: https://doi.org/10.1016/j.ceb.2008.06.008.

[17] "Collagen I matrix turnover is regulated by fibronectin polymerization". In: *American Journal of Physiology - Cell Physiology* 297.5 (2009). DOI: 10.1152/ajpcell.00341.2009. URL: https://doi.org/10.1152/ajpcell.00341.2009.

[18] J. Sottile and D. C. Hocking. "Fibronectin Polymerization Regulates the Composition and Stability of Extracellular Matrix Fibrils and Cell-Matrix Adhesions". In: *Molecular Biology of the Cell* 13.10 (2002), pp. 3546–3559. DOI: 10.1091/mbc.E02-01-0048. URL: https://doi.org/10.1091/mbc.E02-01-0048.

[19] "Role of fibronectin in collagen deposition: Fab' to the gelatin-binding domain of fibronectin inhibits both fibronectin and collagen organization in fibroblast extracellular matrix". In: *The Journal of Cell Biology* 92.2 (1982), pp. 485–492. DOI: 10.1083/jcb.92.2.485. URL: https://doi.org/10.1083/jcb.92.2.485.

[20] "Fibronectin-dependent collagen I deposition modulates the cell response to fibronectin". In: *American Journal of Physiology - Cell Physiology* 292.3 (2007). DOI: 10.1152/ajpcell.00130.2007. URL: https://doi.org/10.1152/ajpcell.00130.2007.

[21] T. Assis-Ribas et al. "Extracellular matrix dynamics during mesenchymal stem cells differentiation". In: *Developmental Biology* 437.2 (2018), pp. 63–74. DOI: 10.1016/j.ydbio.2018.03.002. URL: https://doi.org/10.1016/j.ydbio.2018.03.002.

[22] M. Chang. "Matrix metalloproteinase profiling and their roles in disease". In: *RSC Advances* 13.9 (2023), pp. 6304–6316. DOI: 10.1039/d2ra07005g. URL: https://doi.org/10.1039/d2ra07005g.

[23] N. Cui, M. Hu, and R. A. Khalil. "Biochemical and Biological Attributes of Matrix Metalloproteinases". In: *Progress in Molecular Biology and Translational Science* 147 (2017), pp. 1–73. DOI: 10.1016/bs.pmbts.2017.02.005. URL: https://doi.org/10.1016/bs.pmbts.2017.02.005.

[24] G. A. Cabral-Pacheco et al. “The Roles of Matrix Metalloproteinases and Their Inhibitors in Human Diseases”. In: *International Journal of Molecular Sciences* 21.24 (2020), p. 9739. DOI: 10.3390/ijms21249739. URL: https://doi.org/10.3390/ijms21249739.

[25] K. Brew, D. Dinakarpandian, and H. Nagase. “Tissue inhibitors of metalloproteinases: Evolution, structure and function1”. In: *Biochimica et Biophysica Acta (BBA) - Protein Structure and Molecular Enzymology* 1477.1 (2000), pp. 267–283. DOI: 10.1016/S0167-4838(99)00279-4. URL: https://doi.org/10.1016/S0167-4838(99)00279-4.

[26] J. Zhou and Y. Shi. “Mesenchymal stem/stromal cells (MSCs): Origin, immune regulation, and clinical applications”. In: *Cellular & Molecular Immunology* 20.6 (2023), pp. 555–557. DOI: 10.1038/s41423-023-01034-9. URL: https://doi.org/10.1038/s41423-023-01034-9.

[27] U. Lindner et al. “Mesenchymal Stem or Stromal Cells: Toward a Better Understanding of Their Biology?” In: *Transfusion Medicine and Hemotherapy* 37.2 (2010), pp. 75–83. DOI: 10.1159/000290897. URL: https://doi.org/10.1159/000290897.

[28] S. Viswanathan et al. “Mesenchymal stem versus stromal cells: International Society for Cell & Gene Therapy (ISCT®) Mesenchymal Stromal Cell committee position statement on nomenclature”. In: *Cytotherapy* 21.10 (2019), pp. 1019–1024. DOI: 10.1016/j.jcyt.2019.08.002. URL: https://doi.org/10.1016/j.jcyt.2019.08.002.

[29] U. Galderisi, G. Peluso, and G. Di Bernardo. “Clinical Trials Based on Mesenchymal Stromal Cells are Exponentially Increasing: Where are We in Recent Years?” In: *Stem Cell Reviews and Reports* 18.1 (2022), pp. 23–36. DOI: 10.1007/s12015-021-10231-w. URL: https://doi.org/10.1007/s12015-021-10231-w.

[30] F. M. Watt and W. T. S. Huck. “Role of the extracellular matrix in regulating stem cell fate”. In: *Nature Reviews Molecular Cell Biology* 14.8 (2013), pp. 467–473. DOI: 10.1038/nrm3620. URL: https://doi.org/10.1038/nrm3620.

[31] T.-J. Kim. “Mechanobiology: A New Frontier in Biology”. In: *Biology* 10.7 (2021), p. 570. DOI: 10.3390/biology10070570. URL: https://doi.org/10.3390/biology10070570.

[32] C. Toma et al. “Fate Of Culture-Expanded Mesenchymal Stem Cells in The Microvasculature”. In: *Circulation Research* 104.3 (2009), pp. 398–402. DOI: 10.1161/CIRCRESAHA.108.187724. URL: https://doi.org/10.1161/CIRCRESAHA.108.187724.

[33] S. W. Wong et al. “Soft extracellular matrix enhances inflammatory activation of mesenchymal stromal cells to induce monocyte production and trafficking”. In: *Science Advances* 6.15 (2020), eaaw0158. DOI: 10.1126/sciadv.aaw0158. URL: https://doi.org/10.1126/sciadv.aaw0158.

[34] S. W. Wong et al. “Inhibition of aberrant tissue remodelling by mesenchymal stromal cells singly coated with soft gels presenting defined chemomechanical cues”. In: *Nature Biomedical Engineering* 6.1 (2022), pp. 54–66. DOI: 10.1038/s41551-021-00740-x. URL: https://doi.org/10.1038/s41551-021-00740-x.

[35] S. W. Wong et al. “Controlled Deposition of 3D Matrices to Direct Single Cell Functions”. In: *Advanced Science* 7.20 (2020), p. 2001066. DOI: 10.1002/advs.202001066. URL: https://doi.org/10.1002/advs.202001066.

[36] S. Barbon et al. “Mesenchymal stromal cell-laden hydrogels in tissue regeneration: Insights from preclinical and clinical research”. In: *Frontiers in Pharmacology* 16 (2025), p. 1670649. DOI: 10.3389/fphar.2025.1670649. URL: https://doi.org/10.3389/fphar.2025.1670649.

[37] K. Y. Lee and D. J. Mooney. “Alginate: Properties and biomedical applications”. In: *Progress in Polymer Science* 37.1 (2012), pp. 106–126. DOI: 10.1016/j.progpolymsci.2011.06.003. URL: https://doi.org/10.1016/j.progpolymsci.2011.06.003.

[38] S. N. Pawar and K. J. Edgar. “Alginate derivatization: A review of chemistry, properties and applications”. In: *Biomaterials* 33.11 (2012), pp. 3279–3305. DOI: 10.1016/j.biomaterials.2012.01.007. URL: https://doi.org/10.1016/j.biomaterials.2012.01.007.

[39] A. Sosnik. “Alginate Particles as Platform for Drug Delivery by the Oral Route: State-of-the-Art”. In: *ISRN Pharmaceutics* (2014), p. 926157. DOI: 10.1155/2014/926157. URL: https://doi.org/10.1155/2014/926157.

Chapter 2

Aim 1: Engineer biocompatible alginate hydrogels to enhance MSC secretion of MMPs

2.1 Introduction

MSCs have the unique ability to remodel their surrounding environment in response to chemical and mechanical cues[1,2]. Through the principles of mechanobiology, the MSC microenvironment can be intentionally tailored to regulate secretome production[1], which in turn can alter the properties of the surrounding matrix, further influencing cell behavior and tissue architecture[3,4,5,6,7]. A bioinert and easily customizable material that mimics biological tissue and supports MSC encapsulation[3] while promoting desired cytokine output can be found in alginate.

In this aim, alginate hydrogels are fabricated and crosslinked using calcium sulfate ($CaSO_4$) to control the mechanical properties of the resulting gels for MSC encapsulation. Initially, acellular hydrogels were created to establish a workable range of $CaSO_4$ concentrations, identifying both low and high levels to compare responses between "soft" and "stiff" hydrogels for downstream experiments. Hydrogel stiffness was quantified using rheometric measurements. These optimized soft and stiff gel formulations were then used for MSC encapsulation. Following encapsulation, the hydrogels are exposed to an inflammatory factor to stimulate cytokine secretion from the MSCs. Resulting MMP expression levels were quantified using quantitative PCR (qPCR), the gold standard for gene expression measurement.

2.2 Alginate as a Biocompatible Matrix

2.2.1 Materials Preparation: Alginate and Calcium Sulfate

Alginic acid sodium salt from brown algae (medium viscosity sodium alginate, Sigma-Aldrich, A2033) was dissolved in deionized water using a laboratory-grade purification system at 1%

weight/volume (w/v). The solution was prepared at room temperature with magnetic stir mixing and allowed to dissolve overnight. The following day, the 1% w/v alginate solution was sterilized using a bottle-top filter system (CELLTREAT, Cat. No. 229707; 500 mL, 0.22 µm PES membrane).

Dialysis was then performed using Spectra/Por 7 dialysis tubing (50 kDa MWCO Repligen, Waltham, MA, USA; Cat. No. 132130). The dialysis process involved submerging the filled tubing for a minimum of three hours in a series of sodium chloride (NaCl) concentrations, starting at 15M and ending with three changes of pure deionized water. A 2.5M NaCl stock solution was prepared by dissolving 146.1g of high-purity sodium chloride (Avantor, Radnor, PA, USA; Cat. No. 7422832) in 1 L of deionized water using a graduated cylinder. This stock solution was used to create dialysis concentrations (**Table 2.1**), which were prepared in a 1,600 mL beaker.

Table 2.1: Dialysis Concentrations

NaCl (g/2 mL)	**2.5 M NaCl (mL)**	**DI H2O**
15 (start)	82.1	1517.9
12.5	68.4	1531.6
10	54.8	1545.2
7.5	41.1	1558.9
5	27.4	1572.6
2.5	13.7	1586.3
Pure DI H2O 3 Times (1600 mL DI H2O)		

Post-dialysis alginate was removed from the tubing and transferred into high-performance 50 mL polypropylene centrifuge tubes (VWR, Radnor, PA, USA; Cat. No. 89039-656), filled to their maximum freezing capacity (approximately 42 mL). The labeled tubes were placed into a $-20°$C freezer overnight. The following day, the tubes were transferred to a $-80°$C freezer and stored under these conditions for a minimum of one night. Once frozen, the caps were removed from

the tubes containing dialyzed 1% w/v alginate, and each tube was covered with Kimtech Science Kimwipes Delicate Task wipers (Kimberly-Clark Professional; catalog number 34155), secured with a rubber band. The tubes were loaded into a lyophilizer pre-cooled to $-80°$C and subjected to vacuum drying. Lyophilization was carried out for a minimum of five days to ensure complete dehydration. After the process was completed, the lyophilized alginate was carefully removed and stored under desiccated conditions at $-20°$C for future use.

Calcium sulfate dihydrate ($CaSO_4 \cdot 2H_2O$) (Santa Cruz Biotechnology; SC-207393, MW 172.17 g/mol) was used as the crosslinking agent for alginate gels. To account for the dihydrate component, the molecular weight of anhydrous calcium sulfate was calculated using the equation:

- 172.17 g/mol – (2×18.02 g/mol) = 136.13 g/mol

A 500 mM stock solution was prepared by calculating the required mass of $CaSO_4 \cdot 2H_2O$ to dissolve in a specified volume of deionized water. The solution was made in an autoclavable glass container and subsequently autoclaved at $120°$C ($250°$F) for 45 minutes. After sterilization, the 500 mM $CaSO_4$ solution was stored at $4°$C in a refrigerator for up to one month for future use.

2.3 Cell Culturing

2.3.1 General Cell Culturing

The D1 ORL UVA cell line (ATCC, CRL-12424), derived from mouse bone marrow, was used. Cells were cultured in 12 mL of medium consisting of Gibco DMEM high glucose (Thermo Fisher Scientific, Cat. No. 31053028) supplemented with 10% MSC-qualified fetal bovine serum (Quality Biological, Cat. No. 110-001-101HI), 1% penicillin–streptomycin solution (Corning®, Cat. No. 30-002-CI) and 1% GlutaMAX Supplement (Gibco, Thermo Fisher Scientific, Cat. No. 35050061). Cultures were maintained in 175 cm^2 NEST cell culture flasks (Cat. No. 5129832770998149 12; NEST Biotechnology Co., Ltd.).

Passaging was performed when MSC confluence reached ~80%. The spent culture medium was removed and the cells were washed with a 1 × dilution of Hank's Balanced Salt Solution

(HBSS) (Gibco, Thermo Fisher Scientific, Cat. No. 14185052). After removing HBSS, adherent cells were detached using 8 mL of HyClone™ Trypsin 0.25% protease solution (Cytiva, P 00445). Flasks were incubated for 3-5 minutes, 37°C with 5% CO_2, then gently tapped to dislodge remaining cells.

Following detachment, 16 mL of culture medium was added to each flask, creating a 2:1 ratio with the existing 8mL of trypsin-EDTA. The resulting cell suspension was collected using an autopipette and transferred into two 15 mL conical tubes (Corning, 17 mm O.D. × 120 mm, Cat. No. 352196). Tubes were centrifuged at 420 rcf, 20°C for 3 minutes. The supernatant was discarded, and the cell pellet was resuspended in either 1 mL of culture medium for continued culturing or 1 mL of freezing medium, composed of 10% molecular biology-grade dimethyl sulfoxide (DMSO) (bioWORLD; 40470006), 50% FBS and 40% culture medium, prior to storage at −80°C.

2.3.2 Cell Counting

Cell viability was assessed using the dye-exclusion method with 20 µL of Trypan Blue solution (0.4% in phosphate-buffered saline; Cytiva/HyClone, Cat. No. SV3008401) mixed with 20 µL of the 1 mL cell suspension obtained during routine passaging. From this mixture, 10 µL was loaded onto each side of a hemocytometer for cell counting. Depending on cell density, dilution of the original suspension was sometimes necessary. This was typically done by adding additional culture medium to facilitate accurate counting, followed by repeating the Trypan Blue staining step using 20 µL of the diluted suspension. Viable cells (those excluding the dye) in all eight squares of the hemocytometer were counted and averaged. The final cell concentration was calculated using the formula:

- Average cell count x 10,000 x 2

This calculated cell count was then used to prepare either six-well plate cultures or gel-encapsulated cell cultures.

2.3.3 Six-Well Plastic Culture

The ideal cell seeding density was determined to be 50,000 cells/mL for a four-day incubation period in plastic culture, using 2 mL of culture medium per well. To prepare six-well plastic cultures, the average cell count obtained from hemocytometer readings was used in the dilution equation:

- $C_1 \times V_1 = C_2 \times V_2$, where
- C_1 = concentration of the original cell suspension,
- C_2 = desired concentration (50,000 cells/mL),
- V_2 = final volume of the diluted solution needed,
- V_1 = volume of the original suspension required to achieve the desired concentration.

An excess volume of the cell/media mixture was prepared to ensure uniform distribution across all wells. The volume of culture medium added to the C_2 suspension was calculated by subtracting V_1 from the total volume needed (with a small excess added for accuracy). The combined V_1 and culture medium formed the final cell suspension. 1 mL of the final suspension was added to each well, followed by an additional 1 mL of fresh culture medium. Cells were seeded into six-well clear, flat-bottom, tissue culture-treated plates (Falcon®, Corning, Cat. No. 353046) and incubated at 37 °C with 5% CO_2.

2.3.4 Gel-encapsulated MSCs

To prepare gel-encapsulated MSCs, lyophilized alginate was weighed and dissolved FluoroBrite™ DMEM (Thermo Fisher Scientific, Cat. No. A1896701) to create a 3% w/v alginate solution. The required amount of FluoroBrite DMEM was calculated using the equation:

- 3 g / 100 mL = A / X,

Where A is the weight of the lyophilized alginate (in grams) and X is the volume of Fluorobrite DMEM (in mL) needed. The solution was allowed to dissolve overnight at room temperature inside a culture hood, while being gently being mixed on a low-speed stir plate. After dissolution, the alginate solution was stored at $4°$C for up to one week.

Two low-retention 2 mL microcentrifuge tubes (Thermo Scientific, Cat. No. 3453) were labeled for 60 mM and 160 mM $CaSO_4$ dilutions. To prepare the 60 mM $CaSO_4$ solution, 120 µL of the 500 mM $CaSO_4$ stock was added to 880 µL of general culture medium. For the 160 mM $CaSO_4$ solution, 320 µL of the 500 mM stock was mixed with 680 µL of general culture medium.

MSCs were passaged as usual until the cell pellet resuspension step. The resulting pellet was resuspended in 10 mL of culture medium and subsequently counted. The equation used to calculate the total cell count for gel encapsulation differs from that used for plastic culture. After obtaining the average cell count from the hemocytometer, the following formula was used to determine the Total Cell Count (TCC):

- Average cell count x 10,000 x 2 x 10mL = TCC

Cell-laden hydrogels were seeded at 1.5 million cells per gel, with six gels created per fabrication requiring approximately 9 million cells in total. To determine the volume of the original suspension needed, the following calculation was performed:

- 9,000,000 ÷ TCC = proportion of the 10 mL suspension needed

The resulting decimal value was then multiplied by 10 mL to obtain the volume of the original suspension required to achieve the desired cell number for gel encapsulation.

The calculated volume of the cell suspension was divided into six microcentrifuge tubes, one for each gel to be fabricated. The tubes were centrifuged at 420 rcf, 20 °C for 3 minutes. After centrifugation, the supernatant was removed, and the resulting cell pellets were resuspended in 1 mL of HBSS. The HBSS-suspended pellets were then centrifuged again under the same conditions. This washing process was repeated two additional times, for a total of three HBSS washes. Following the final centrifugation, the supernatant was discarded, and each pellet was resuspended in 50

µL of culture medium. These 50 µL cell suspensions were then transferred into sterile, single-use 3 mL Luer-Lok™ syringes (BD, 309657) using a pipette, in preparation for gel encapsulation.

400 µL of the 3% alginate/FluoroBrite DMEM solution was drawn into a 3 mL Luer-lock syringe and connected to another syringe containing the 50 µL cell pellet suspension. The syringes were pressed back and forth to mix the contents thoroughly, as illustrated in (**Figure 2.1A**). The final cell/alginate mixture was retained in one syringe, while the other was disconnected and discarded.

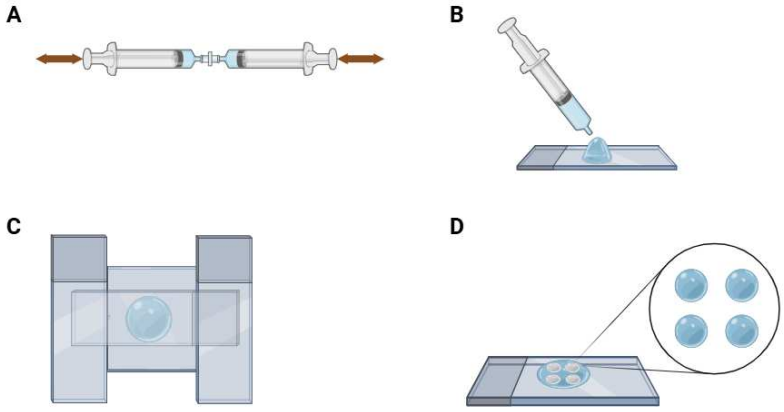

Figure 2.1: Fabrication of cell-laden alginate hydrogels. (A) Two syringes containing either (1) Alginate/FluoroBrite DMEM solution or cell pellet suspension or (2) cell/alginate mixture or $CaSO_4$ are connected and rapidly pressed back and forth for mixing. (B) The resulting $CaSO_4$/alginate mixture is deposited onto a glass slide. (C) Base slide is flanked by two 1 mm spacer slides and covered by a third slide to ensure uniform 1 mm thickness across gel. (D) After gelation period, four punchouts (8 mm diameter) were taken from each gel. Note. Figure generated in Biorender.

Next, 150 µL of the 60 mM $CaSO_4$ dilution was pipetted into a third syringe, which was then quickly connected to the syringe containing the cell/alginate mixture. The contents were mixed using the same back-and-forth method (**Figure 2.1A**). The resulting $CaSO_4$/alginate mixture was then deposited onto a glass slide (**Figure 2.1B**), flanked by two 1 mm spacer slides and covered by a third slide to ensure uniform 1 mm thickness across the gel (**Figure 2.1C**).

Due to the final composition, the 3% w/v alginate was effectively reduced to a 2% w/v working concentration, and all $CaSO_4$ dilutions were divided by four to reflect their working concentrations

in the final 600 µL gel. This process was repeated to fabricate two additional gels at 60 mM $CaSO_4$, followed by three gels at 160 mM $CaSO_4$.

Gelation was allowed to proceed for 2 hours, after which four punchouts (~8 mm diameter) were taken from each gel (**Figure 2.1D**). These punchouts were placed into the center 8 wells of three 24-well clear, flat-bottom, tissue-culture treated plates (Corning, Cat. No. 3527) with the center 8 wells filled with 500 µL of culture medium, and the surrounding 16 wells containing 1 mL of HBSS, as shown in (**Figure 2.2A**). Submerged gels were then incubated at 37 °C with 5% CO_2 for one day.

2.3.5 Gel Mechanical Characterization

The mechanical properties of alginate hydrogels are critical to the experiments in this project. Therefore, the gel fabrication process (excluding cells) was performed to establish a gel library. This library was created to identify a workable range of low and high $CaSO_4$ concentrations for downstream comparisons of cellular responses to "soft" and "stiff" hydrogels. During this process, qualitative criteria for hydrogel selection included homogeneity and the ability to remain intact and maintain shape after being covered by the top slide.

Rheological characterization of the hydrogels was performed using the Discovery Hybrid Rheometer HR 20 (TA Instruments, New Castle, DE, USA). Following fabrication, gelation was allowed to proceed for 2 hours. Punchouts were then extracted from each gel using the same method employed for cell encapsulation. To simulate physiological conditions, each punchout was placed in the rheometer's submersion chamber filled with culture media pre-warmed to 37°C. Axial compression tests were conducted using a plate also pre-heated to 37°C, with a soak time of 60 seconds prior to testing. Compression was applied at a rate of 5 µm/sec for a duration of 100 seconds. These tests were used to determine the Young's modulus of each gel formulation, residing in the first 10% of compression. Based on the resulting mechanical profiles, optimal low and high concentrations of $CaSO_4$ were identified for subsequent experimental use.

2.3.6 Inflammation Factor

Following a one-day incubation, the 24 well-plates were treated with recombinant mouse TNF-α (Gibco/PeproTech, 501628684) as an inflammatory factor. Upon arrival, the lyophilized TNF-α powder was allowed to reach room temperature and then dissolved in HBSS. 1.5 mL microcentrifuge tubes were labeled for aliquots, and a concentration of 50 ng/mL was prepared in each tube.

The optimal ratio of TNF-α to culture media was determined to be 0.4uL TNF-α : 1999.6 uL culture media, yielding a total volume of 2 mL and a final concentration of 10 μg/mL. This ratio was established through trial-and-error, as it represented the highest concentration that maintained nearly 100% cell viability. The existing culture media in the 24 well-plate was carefully removed via pipette. Then, four of the center eight wells were filled with 500 µL of TNF-α-supplemented media, while the remaining four received 500 µL of regular culture media, as shown in **Figure 2.2A**.

TNF-α treatment for the six-well plastic plates was performed similarly: the existing media was removed via pipette, and 1 mL of either regular or TNF-α-supplemented culture media was added to each well, as shown in **Figure 2.2B**. All treated plates were returned to the incubator and maintained at 37°C, 5% CO_2 for an additional three days.

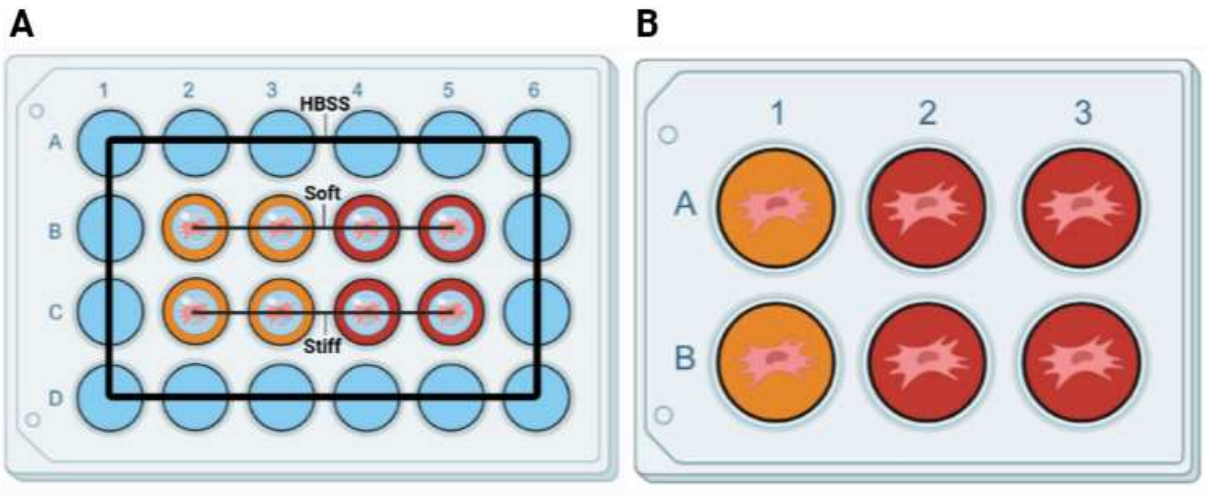

Figure 2.2: Well-plate configurations for hydrogel and plastic cultures. (A) 24-well plate layout for cell-laden alginate hydrogels: orange wells contain standard culture media; red wells contain TNF-α-supplemented media. (B) 6-well plate layout for MSC plastic cultures: orange = standard media, red = TNF-α-supplemented media. Note: Schematics in A and B were created using BioRender.

2.4 Plastic Wells RNA Purification and Reverse Transcription

After the three-day experimental incubation period, culture media from each well of the plastic culture plates was carefully removed and transferred into 1.5 mL microcentrifuge tubes for downstream analyses. Each well was then washed twice with 1 mL of HBSS, followed by total RNA isolation using 1 mL of TRIzol™ Reagent (Invitrogen™, Thermo Fisher Scientific; Cat. No. 15596018, 200 mL). TRIzol was allowed to incubate in the wells for 3-5 minutes at room temperature. The contents of each well were then collected into 1.5 mL microcentrifuge tubes for immediate RNA purification or stored at $-80°$C for up to two weeks.

For RNA purification, TRIzol-treated samples were kept on ice throughout the process. 200 µL of chloroform (ACS Reagent Grade; Ricca Chemical, Cat.No.RSOC0020) was added to each tube to initiate phase separation. Samples were vigorously shaken, then centrifuged at 14,000 rcf, $4°$C for 10 minutes. New 1.5 mL microcentrifuge tubes were labeled and placed on ice. After centrifugation, the upper aqueous phase was carefully transferred into the tubes.

To precipitate nucleic acids, 500 µL of 2-Propanol (Sigma-Aldrich, Cat. No. I9516) was added to each sample. Tubes were gently shaken and then left undisturbed on ice for at least ten minutes, followed by centrifugation under the same conditions as above. The supernatant was discarded, and the resulting pellet was washed with 1 mL of 75% ethanol (Fisher BioReagents™, Catalog No. BP28184). Samples were vortexed briefly and centrifuged at 2350 rcf, 4°C for 5 minutes. The supernatant was carefully removed via pipette to avoid disturbing the pellet, which was then resuspended in 10 µL of RNase-free water.

RNA quantification was performed using the NanoDrop™ OneC Microvolume UV-Vis Spectrophotometer (Thermo Scientific™, Catalog No. ND-ONEC-W). Prior to sample readings, the instrument was blanked with 1 µL of nuclease-free water, and this step was repeated before the first sample to ensure proper calibration. 1 µL of each RNA sample was loaded onto the NanoDrop, and absorbance was measured at 260 and 280 nm. The RNA concentration and purity ratios (A260/A280 and A260/A230) were calculated using NanoDrop software (version 2.11.0.10). Each sample was evaluated to ensure they met minimum criteria of 30 ng/µL for concentration and a purity ratio of at least 1.60. Samples meeting these thresholds were then advanced to reverse transcription.

After NanoDrop quantification, RNA samples were transferred from 1.5 mL microcentrifuge tubes into 0.2 mL polypropylene PCR tubes (USA Scientific, TempAssure, Cat. No. PCR-Tu-Flat). Total RNA was reverse transcribed into complementary DNA (cDNA) using a protocol adapted for this study.

Each RNA sample was combined with:

- 1 µL 50 µM Random Hexamer Primer (Thermo Scientific, Cat. No. SO142)
- 1 µL 10 mM dNTP solution (Thermo Scientific, Cat. No. R0192)

The mixture was incubated in a qPCR thermocycler at 65°C for 5 minutes to denature RNA secondary structures and facilitate primer annealing. After incubation, samples were chilled on ice for 1 minute.

A reverse transcription master mix was then prepared for each sample, containing:

- 4 µL 5x SSIV Buffer (Invitrogen, Thermo Fisher Scientific; Cat. No. 18080044)
- 1 µL DTT (Thermo Fisher Scientific, 0.1 M, Cat. No. 707265ML)
- 1 µL RiboLock RNase Inhibitor (Thermo Scientific, Cat. No. EO0381; 40 U/µL)
- 1 µL SuperScript™ III Reverse Transcriptase (Invitrogen, Thermo Fisher Scientific; Cat. No. 18080044)

This 7 µL master mix was added to each sample tube, and the tubes were placed back into the thermocycler under the following conditions:

- Primer annealing: $25°$C for 5 minutes: Stabilizes primer-template hybridization before extension
- Extension: $50°$C for 45 minutes: SuperScript III synthesizes cDNA from the RNA template
- Enzyme inactivation: $70°$C for 15 minutes: Terminates the reverse transcription reaction by inactivating the enzyme

The resulting cDNA was either used immediately for qPCR analysis or stored at $-20°$C for future use.

2.5 Gel-encapsulated MSC Purification & Reverse Transcription

2.5.1 Digestion of Gel-encapsulated MSCs

After the three-day experimental incubation period, culture media from each well was carefully removed and transferred into 1.5 mL microcentrifuge tubes, then stored at $-80°$C for downstream analyses. The alginate gel constructs were subsequently subjected to ethylenediaminetetraacetic

acid (EDTA) digestion to prepare for RNA purification. A 50 mM EDTA solution was prepared by dissolving 0.103 g of EDTA (Sigma-Aldrich, Cat. No. E9884) in 5 mL of nuclease-free water. 150 µL of the EDTA solution was pipetted into each well, and the gels were mechanically disrupted by pipetting up and down using a 1000 µL pipette until fully disintegrated, to encourage cell wall breakdown. The resulting contents were then ready for RNA purification.

2.5.2 CTAB protocol and RNA Purification/Reverse Transcription

The presence of alginate required a modification to the standard RNA purification protocol used for plastic cultures. Literature review revealed the need for polysaccharide decontamination[8,9]. Based on a protocol adapted from [8] and [9], it was found that the cationic detergent cetyltrimethylammonium bromide (CTAB) is effective in precipitating RNA from plant tissues rich in polysaccharides, making it suitable for alginate-containing samples.

Plant RNA/DNA extraction success depends on accomplishment of the following[9]:

1. Cell wall breakdown: Achieved in EDTA digestion
2. Cell membrane breakdown: Detergent used to disrupt cell membranes to release RNA and DNA
3. RNA/DNA protection: Prevention of RNA/DNA degradation
4. RNA/DNA isolation: RNA/DNA in the extraction buffer separated from other components
5. RNA/DNA precipitation: RNA/DNA precipitated out

Using insights from the literature, a CTAB extraction buffer and protocol were prepared. **Table 2.2** contains the reagents found in the buffer, in addition to their specific purposes[9]. The bulk recipe with precise measurements can be found in **Appendix B**. The buffer was stored at room temperature in a chemical fume hood for up to two months.

EDTA-digested samples were transferred into 1.5 mL centrifuge tubes containing pre-warmed CTAB extraction buffer at $65°$C, and vortexed for 5 minutes. To initiate phase separation, 600 µL

Table 2.2: CTAB Reagents and Purposes

Reagent	**Purpose**
Nuclease-free Water	
CTAB (Sigma-Aldrich, Cat. No. H6269)	Break cell membranes
Polyvinylpyrrolidone (Sigma-Aldrich, Cat. No. PVP40)	Remove phenolic compounds from plant DNA/RNA extracts
NaCl	Remove DNA-bound proteins and keep them dissolved in aqueous layer
Tris-HCl (Sigma-Aldrich, Cat. No. 648313)	Buffer for DNA stability
EDTA	Chelates divalent cations (Ca^{2+} and Mg^{2+}), make DNases nonfunctional
β-Mercaptoethanol (Sigma-Aldrich, Cat. No. 444203)	Clean tannins and polyphenols

of 24:1 chloroform-isoamyl alcohol (ACS reagent grade; Sigma Aldrich, Cat.No.AX1440) was added to each tube. Samples were then vigorously shaken and centrifuged at 15,000 × g, 20°C for 5 minutes.

After phase separation, the upper aqueous phase was carefully transferred into new 2 mL microcentrifuge tubes placed on ice. A second round of 600 uL chloroform-isoamyl alcohol was added to each tube, followed by shaking and again centrifugation under the same conditions. The upper phase was again extracted, and 600 µL of 2-propanol was added to each tube to precipitate nucleic acids. Tubes were gently shaken and then left undisturbed on ice for at least 10 minutes.

Samples were then centrifuged at 15,000 × g, 20°C for 15 minutes. The supernatant was discarded, and the resulting pellet was washed in 1 mL of 75% ethanol. Samples were centrifuged again at 15,000 × g, 20°C for 5 minutes. The supernatant was removed via pipette, taking care not to disturb the pellet. The pellet was then resuspended in 20 µL of RNase-free water. Samples were then transferred into 0.2 mL PCR tubes, and NanoDrop quantification was performed as described for plastic culture samples, using the same concentration and purity criteria.

Following NanoDrop quantification, reverse transcription was performed on the gel-encapsulated cell RNA samples using the same protocol as for plastic culture samples.

2.6 qPCR

2.6.1 Primers

Primers are short, single-stranded DNA sequences that serve as starting points for DNA synthesis during polymerase chain reaction (PCR). They are designed to bind specifically to target regions of DNA, allowing for the amplification of genes of interest. In this study, primers were designed to target the following genes: GAPDH (as a housekeeping gene for normalization), and MMP-2, MMP-3, MMP-9, and MMP-10, which are matrix metalloproteinases involved in extracellular matrix remodeling and inflammation.

Primer sequences were identified using the NCBI Primer-BLAST tool (ncbi.nlm.nih.gov), which provided gene-specific sequences based on accession numbers. These sequences were then input into IDT's PrimerQuest Tool (idtdna.com) to finalize assay design and evaluate thermodynamic properties. The final primer sequences for each gene were ordered from Invitrogen (**Table 2.3**).

Upon receipt, primers were dissolved in RNase-free water to prepare a 100 μM stock solution. This concentration is commonly used for long-term storage and allows for flexible downstream dilutions. From the stock, a working solution of 10 μM was prepared by performing a 1:10 dilution. Aliquots of the working solution were stored in low-retention microcentrifuge tubes to minimize freeze-thaw cycles and preserve primer integrity. This working concentration was used for all qPCR reactions, ensuring consistent primer performance across assays targeting GAPDH, MMP-2, MMP-3, MMP-9, and MMP-10.

2.6.2 Quantitative PCR (qPCR)

PCR plates were prepared for both plastic culture and gel-encapsulated cell samples, with each gene analysis performed in triplicate to ensure reproducibility and statistical reliability. The plate layout was organized as shown in **Figure 2.3**. To perform quantitative PCR (qPCR), a master mix was prepared for each target gene, including the housekeeping gene GAPDH, which served as an internal control for normalization.

Gene and Accession	Forward	Reverse
GAPDH NM_008084.4	CTTTGTCAAGCTCATTTCCTGG	TCTTGCTCAGTGTCCTTGC
MMP-2 NM_008610.3	ACCAAGAACTTCCGATTATCCC	CAGTACCAGTGTCAGTATCAGC
MMP-3 NM_010809.3	GATGAACGATGGACAGAGGATG	AAACGGGACAAGTCTGTGG
MMP-9 NM_013599.5	GATCCCCAGAGCGTCATTC	CCACCTTGTTCACCTCATTTTG
MMP-10 NM_019471.3	AGACCCCAGACAAATGTGATC	CAAATGAAATTCAGGCTCGGG

Table 2.3: Primer and Probe Sequences used for qPCR.

qPCR was conducted using SYBR Green chemistry on a QuantStudio 3 Real-Time PCR System (Thermo Fisher Scientific). Plate setup and run parameters were configured using Applied Biosystems Design & Analysis Software version 2.6.0 with layout matching that illustrated in **Figure 2.3**. Each 30 µL reaction contained the following components:

- 15 µL Forget-Me-Not™ EvaGreen® qPCR Master Mix (Biotium, Cat. No. 31041-T)
- 0.3 µL 10 µM forward primer
- 0.3 µL 10 uM reverse primer
- 3 µL of cDNA template

The cycling conditions were as follows:

- Initial hold: 50 °C for 2 minutes
- Initial denaturation: 95 °C for 10 minutes
- Amplification: 40 cycles of: 95 °C for 15 seconds, 60 °C for 1 minute

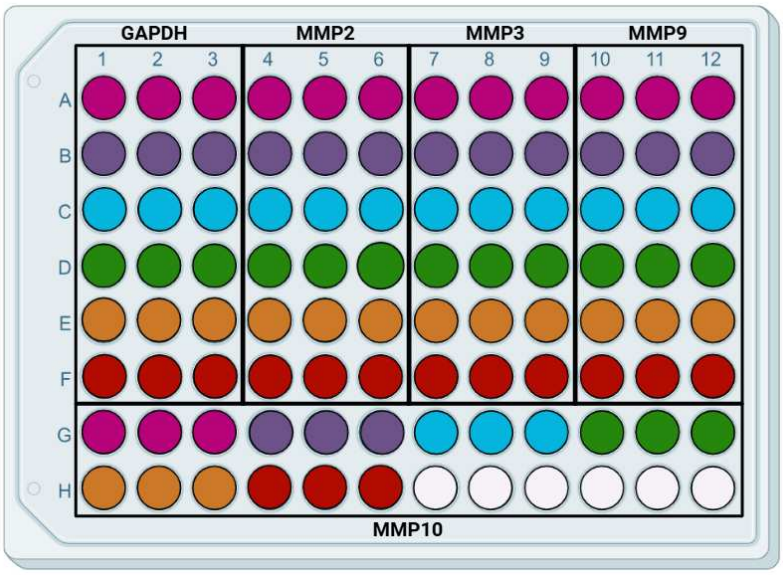

Figure 2.3: PCR Plate Layout. Target genes are sectioned by black lines, and labeled GAPDH, MMP-2, MMP-3, MMP-9 and MMP-10. Colors for samples are pink = soft gel control, purple = soft gel TNF-α, blue = stiff gel control, green = stiff gel TNF-α, orange = plastic control, red = plastic TNF-α. Samples were analyzed in triplicate to ensure reproducibility and statistical reliability.

2.7 MMP-3 ELISA

Given the significant upregulation of MMP-3 observed in the qPCR results (**Figure 2.6**) and the known role of fibronectin in modulating collagen deposition[10,11,12,13], MMP-3 was selected for further investigation as a potential therapeutic target. To quantify MMP-3 production levels secreted into the surrounding culture media by gel-encapsulated MSCs, a solid-phase sandwich ELISA kit specific to MMP-3 was used. Because MMP-3 levels were expected to be difficult to quantify, the high sensitivity of ELISA made it an ideal method for detection.

2.7.1 Collection of Conditioned Culture Media (CCM) from Gel-Encapsulated Cells and Plastic Culture

Gel-encapsulated MSCs were prepared as described previously for subsequent RNA analysis of MMP-3 expression. During sample preparation for RNA purification, the culture media surrounding both the hydrogels and plastic cultures was collected into 2 mL microcentrifuge tubes

and stored at $-80°$C for downstream applications. This collected media, referred to henceforth as conditioned culture media (CCM), was used for MMP-3 ELISA analysis and an *in vivo* degradation analysis, the latter performed in a fibrosis murine model and discussed in a subsequent chapter.

2.7.2 Reagents

For this experiment, the Mouse Matrix Metalloproteinase 3 (MMP-3) ELISA Kit (Thermofisher, Cat. EEL099) was used. This kit is a solid-phase sandwich enzyme-linked immunosorbent assay (ELISA) designed to detect and quantify murine MMP-3 levels in biological fluids. All necessary reagents for quantification were provided in the kit.

Reagent Preparation:

- 1X Wash Buffer: 30 mL of Wash Solution Concentrate (25X) was diluted with 720 mL of deionized water. The solution was labeled as 1X Wash Buffer and stored at $8°$C.

- 1X Biotinylated Detection Antibody Solution: Prepared as needed, using 100 µL/per well (plus an additional 200 µL to ensure sufficient volume). The antibody vial was centrifuged at 800 × g at 2-$8°$C for one minute. The 100x antibody solution was then diluted to a 1X working solution using the Biotinylated Detection Antibody Diluent, based on the calculated required volume.

- 1X HRP Conjugate Solution: Prepared similarly, using 100 µL/per well (plus 200 µL extra). The HRP vial was centrifuged at 800 × g at 2-$8°$C for one minute. The 100x HRP solution was diluted to a 1X working solution using the HRP Conjugate Diluent, according to the calculated volume needed.

- Diluted Standards: The provided standard vial was centrifuged at 10,000 × g at 2-$8°$C for one minute collect contents at the bottom. 1 mL of Standard & Sample diluent was added, and the vial was allowed to stand for 10 minutes with occasional inversion. Afterward, the contents were mixed thoroughly with a pipette to create a working solution of 10 ng/mL. Seven 1.5 mL microcentrifuge tubes were prepared, each containing 500 µL of Standard &

Sample diluent. A serial dilution was performed by transferring 500 µL of the 10 ng/mL solution into the first tube and mixing thoroughly to create a 5 ng/mL solution. This process was repeated sequentially until the second-to-last tube. The final tube contained only diluent and served as the blank. The resulting dilution gradient was: 10, 5, 2.5, 1.25, 0.63, 0.31, 0.16, and 0 ng/mL. The remaining 10 ng/mL stock was stored at $-20°$C for future use.

Samples were thawed on ice and required no dilution to fall within the standard curve range. To minimize degradation and variability, samples were only thawed once, used immediately, and then discarded.

2.7.3 Procedure and Analysis

100 µL of standards, blanks, and duplicate samples were added to designated wells, following the layout shown in **Figure 2.4**. The plate was sealed with the provided plate sealer and incubated for 90 minutes at $37°$C. After incubation, the plate was aspirated. Next, 100 µL of Biotinylated Detection Antibody Working Solution was added to all wells. The plate was resealed and incubated for 60 minutes at $37°$C. Following incubation, the plate was aspirated and washed three times with 350 µL of 1x Wash Buffer. The buffer was allowed to sit in the wells for 1 minute before each aspiration.

After the third wash, 100 µL of HRP Conjugate Working Solution was added to each well. The plate was covered and incubated for 30 minutes at $37°$C. It was then aspirated, and the wash process was repeated 5 times using 350 µL of 1X Wash Buffer per wash. Following the final wash, 90 µL of Substrate Reagent was added to each well. The plate was resealed and incubated for approximately 15 minutes, protected from light. Once sufficient color development was observed, 50 µL of Stop Solution was added to each well in the same order as the substrate addition, terminating the enzymatic reaction and changing the color from blue to yellow. The plate was gently tapped to ensure thorough mixing, and absorbance was immediately measured at 450 nm using a microplate reader (Agilent BioTek Epoch 2 Microplate Spectrophotometer; Agilent Technologies) with Gen 6 software version 1.04.

Raw absorbance values were exported to Excel for analysis. The absorbance value of the blank standard was subtracted from all readings. A standard curve was generated in Excel by forcing the Y-intercept to (0,0) and fitting a line of best fit. The standard linear equation, Y = mX + b, was used to calculate the concentration of each sample, where Y is the blank-adjusted absorbance, m is the slope of the fitted line, and b is the forced intercept of zero. Each equation was solved for X, yielding the MMP-3 concentration of each sample in ng/mL.

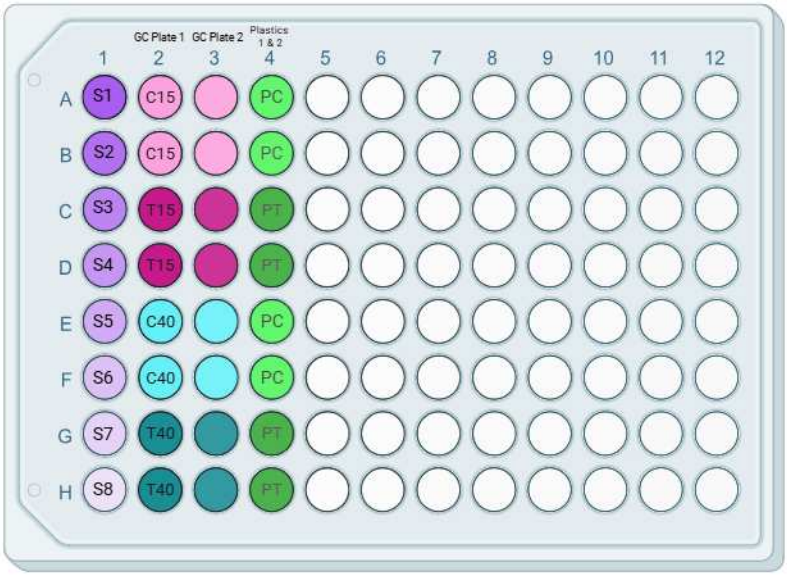

Figure 2.4: MMP-3 ELISA plate layout for a single experiment containing a standard curve (purple), soft gel control (light pink), soft gel TNF-α (dark pink), stiff gel control (light blue), stiff gel TNF-α (dark blue), plastic control (light green), and plastic TNF-α (dark green). All samples were performed in duplicate.

2.8 Stiffness Analysis of Hydrogels

Compression testing was conducted on alginate hydrogels crosslinked with varying concentrations of $CaSO_4$ to evaluate the influence of crosslinker density on mechanical stiffness and to determine optimal low and high $CaSO_4$ concentrations for subsequent experimental use. Only gels that met the minimum qualitative criteria, including homogeneity, structural integrity and the ability to maintain shape after being covered by a top slide, were selected for rheometric analysis. Each hydrogel had a total volume of 600 µL, composed of:

- 400 µL of 3% (w/v) alginate solution
- 50 µL of FluoroBrite DMEM
- 150 µL of $CaSO_4$ solution

This formulation effectively reduced the alginate concentration from 3% to 2% (w/v) in the final gel. Additionally, the $CaSO_4$ concentration was diluted to one-quarter of its original stock concentration due to the mixing ratio. Based on qualitative assessments, the working range of $CaSO_4$ concentrations was determined to be 15 mM to 40 mM, with compression tests performed at 5 mM increments within this range.

The stress-strain curves for all samples exhibited nonlinear elastic behavior, with a distinct linear region up to approximately 10% strain. To ensure consistency across samples, Young's modulus was calculated at 10% strain, within this linear region. As shown in **Figure 2.5**, the results demonstrated a clear trend: increasing $CaSO_4$ concentration led to a progressive increase in Young's modulus, indicating enhanced network stiffness due to greater ionic crosslinking.

To determine whether the difference in stiffness between the softest and stiffest hydrogels was statistically significant, an unpaired two-tailed t-test with Welch's correction was performed. The comparison was made between hydrogels crosslinked with 15 mM $CaSO_4$ (softest group, n = 3) and 40 mM $CaSO_4$ (stiffest group, n = 3).

The softest hydrogels exhibited a mean value of 2.91 kPa, while the stiffest hydrogels measured 5.00 kPa. The difference between groups was 2.09 ± 0.62 (SEM). An unpaired two-tailed Welch's t-test yielded a t value of 3.386 with 3.572 degrees of freedom and a p value of 0.0329, indicating a statistically significant difference between the two groups (**Figure 2.5**).

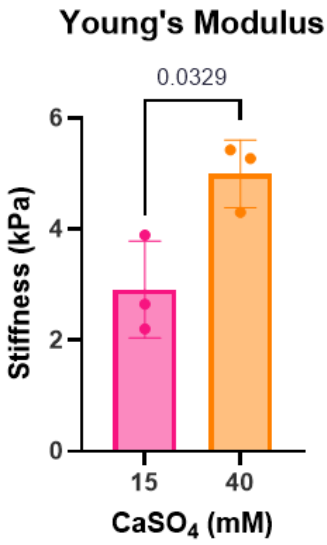

Figure 2.5: Young's Modulus measurements of alginate hydrogels. Comparison between the softest (15 mM $CaSO_4$) and stiffest (40 mM $CaSO_4$) hydrogels: the softest formulation exhibited a mean Young's Modulus of 2.91 kPa, while the stiffest reached 5.00 kPa. Statistical analysis yielded a p-value < 0.0329. Note. Graph visualized in GraphPad Prism.

2.9 qPCR Results

Quantitative PCR was used to identify gene expressions of different MMPs in plastic and gel-encapsulated MSC samples. This analysis was used to confirm whether alginate hydrogel encapsulation affects MSC behavior and expression of these ECM modulating enzymes. Normalizing against the housekeeping gene GAPDH, the MMPs 2, 3, 9 and 10 were selected for qPCR analyses. MMP-2 and 9 are gelatinases and degrade gelatin and basement membranes present in the ECM, while MMP-3 and 10 are stromelysins and primarily degrade fibronectin and collagen[14]. All qPCR analyses were performed on cells between passages 11 and 32. Results of qPCR analysis can be seen in **Figure 2.6** and are presented individually.

To assess whether there were statistically significant differences among six independent groups, a two-way analysis of variance (ANOVA) was conducted. This test was appropriate for comparing group means based on gel encapsulation and inflammation factor, with gene expression as the outcome measure. Prior to analysis, assumptions of normality and homogeneity of variances were evaluated and met. The ANOVA revealed significant differences among the groups, prompting

a post hoc analysis using Tukey's Honestly Significant Difference (HSD) test. This allowed for pairwise comparisons to determine which specific group differences were statistically significant while controlling for Type I error.

2.9.1 MMP-2

A two-way ANOVA was performed to examine the effects of gel encapsulation and TNF-α treatment on MMP-2 expression. The analysis revealed significant main effects of both factors and a significant interaction. Specifically, the row factor (gel encapsulation) was significant ($F(2, 24) = 5.037$, $p = 0.0149$), the column factor (TNF-α vs. Control) was significant ($F(1,24) = 6.527$, $p = 0.0174$), and the interaction between the two factors was also significant ($F(2,24) = 3.987$, $p = 0.0320$). These findings indicate that TNF-α treatment increased MMP-2 expression and that this effect varied depending on gel encapsulation. The predicted least squares mean for the control group was 0.0002899, while TNF-α was 0.001229, with a mean difference of -0.0009391 (95% CI: -0.001698 to -0.0001804), confirming a robust increase in MMP-2 with TNF-α treatment. To identify which specific groups differed, a post hoc analysis using Tukey's Honestly Significant Difference (HSD) test was conducted.

Tukey's HSD post hoc analysis revealed several statistically significant pairwise differences among the six groups. Specifically, the soft gel with inflammation factor (soft TNF-α) differed significantly from both the plastic control ($p = 0.0050$), the plastic TNF-α ($p = 0.0032$), indicating that gel encapsulation is necessary for upregulation. Additionally, the soft TNF-α group showed significant difference when compared to the soft control ($p = 0.0114$), and the stiff control ($p = 0.0117$), indicating that inflammation factor presence in addition to gel encapsulation is necessary for upregulation of MMP-2. Lastly, significance was established between the soft TNF-α and the stiff TNF-α ($p = 0.0254$), suggesting that encapsulation in a softer matrix can elicit a higher expression. No significant differences were observed between plastic control and plastic TNF-α groups, as well as between stiff control and stiff TNF-α groups. Altogether, these results suggest

that encapsulation in a softer matrix with inflammation factor presence for MSCs has a more pronounced effect on MMP-2 expression. These results are illustrated in **Figure 2.6A**.

2.9.2 MMP-3

Two-way ANOVA analysis for MMP-3 revealed a significant main effect of the column factor (TNF-α vs. Control) ($F(1, 24) = 7.070$, $p = 0.0137$), indicating that TNF-α treatment increased MMP-3 expression compared to control. However, the row factor ($F(2,24) = 2.611$, $p = 0.0942$), and the interaction between the row and column factors ($F(2,24) = 2.599$, $p = 0.0951$) were not statistically significant, suggesting that differences among gel encapsulation conditions and their interaction with TNF-α did not meaningfully influence MMP-3 levels. The predicted least squares mean for the control group was 0.001317, while TNF-α was 0.05830, with a mean difference of -0.05698 (95% CI: -0.1012 to -0.01275), confirming a significant increase in MMP-3 expression with TNF-α treatment. To explore pairwise differences among row conditions within each treatment group, a post hoc analysis using Tukey's HSD test was conducted.

Tukey's HSD post hoc analysis revealed significant pairwise differences between the soft gel with inflammation factor (soft TNF-α) and the plastic control ($p = 0.0244$), and plastic TNF-α ($p = 0.0266$), again indicating that gel encapsulation is necessary for upregulation. Additionally, the soft TNF-α group showed significant difference when compared to the soft control ($p = 0.0248$), the stiff control ($p = 0.0258$), again showing the effect of inflammation factor presence on expression. No significant differences were observed between plastic control and TNF-α groups, as well as between stiff control and TNF-α groups. However, there was also no significance established between the soft TNF-α and stiff TNF-α, indicating that matrix stiffness may not have an impact on MMP-3 expression. It is also worth noting that the scale at which MMP-3 was upregulated was much larger than in other MMPs. These results suggest that encapsulation in a matrix and presence of an inflammation factor may elicit significant MMP-3 upregulation, but that matrix stiffness may not have an impact. Results of these findings are illustrated in **Figure 2.6B**.

2.9.3 MMP-9

Two-way ANOVA analysis for MMP-9 revealed a significant main effect of the column factor (TNF-α vs. Control) ($F(1, 10) = 18.94$, $p = 0.0014$), indicating that TNF-α treatment markedly increased MMP-9 expression compared to control. In contrast, the row factor ($F(1,10) = 3.800$, $p = 0.0798$), and the interaction between the row and column factors ($F(1,10) = 3.035$, $p = 0.1121$) were not statistically significant, suggesting that matrix stiffness and its interaction with TNF-α did not significantly influence MMP-9 levels. The predicted least squares mean for the control group was 2.868×10^{-5}, while TNF-α was 3.628×10^{-4}, with a mean difference of -0.0003341 (95% CI: -0.0005052 to -0.0001631), confirming a strong TNF-α-driven increase in MMP-9 expression. Post-hoc analysis using Tukey's HSD was used to identify significant pairwise differences.

Tukey's HSD post hoc analysis revealed significant pairwise differences between the soft gel with inflammation factor (soft TNF-α) and the soft control ($p = 0.0070$) and stiff control ($p = 0.0056$), again showing the effect of inflammation factor presence on expression. No significant differences were observed between the soft TNF-α and stiff TNF-α, indicating that matrix stiffness may not have an impact on MMP-9 expression. Additionally, plastic control and TNF-α data obtained at this time did not fit inclusion criteria. Therefore, plastic analysis will be included in further studies. Absent of plastic comparisons, these results suggest that encapsulation in a matrix and presence of an inflammation factor may result in significant MMP-9 upregulation, but that matrix stiffness may not have an impact. Results of these findings are illustrated in **Figure 2.6C**.

2.9.4 MMP-10

A two-way ANOVA was conducted to evaluate the effects of gel encapsulation and TNF-α treatment on MMP-10 expression. The analysis revealed significant main effects of both factors and a significant interaction. Specifically, the row factor (gel encapsulation) was significant ($F(2, 14) = 4.647$, $p = 0.0283$), the column factor (TNF-α vs. Control) was highly significant ($F(1, 14) = 16.85$, $p = 0.0011$), and the interaction between the two factors was also significant ($F(2,14) = 7.066$, $p = 0.0076$). These findings indicate that TNF-α treatment increased MMP-10 expression

and that this effect varied depending on gel encapsulation. The predicted least squares mean for the control group was 0.0008325, while TNF-α was 0.004433, with a mean difference of -0.003600 (95% CI: -0.005481 to -0.001719), confirming a strong TNF-α-driven increase in MMP-10 expression. Post-hoc analysis using Tukey's HSD was conducted to identify specific pairwise differences.

Tukey's HSD post hoc analysis revealed significant pairwise differences between the soft gel with inflammation factor (soft TNF-α) and the plastic control (p = 0.0010), and plastic TNF-α (p = 0.0072), again indicating that gel encapsulation is necessary for upregulation. Additionally, the soft TNF-α group showed significant difference when compared to the soft control (p = 0.0009) and the stiff control (p = 0.0045), indicating that inflammation factor presence in addition to gel encapsulation is necessary for upregulation of MMP-10. Lastly, significance was established between the soft TNF-α and the stiff TNF-α (p = 0.0083), suggesting that encapsulation in a softer matrix can cause higher MMP-10 expression. No significant differences were observed between plastic control and plastic TNF-α groups, as well as between stiff control and stiff TNF-α groups. These results suggest that encapsulation in a softer matrix with inflammation factor presence can stimulate MMP-10 expression. Results are illustrated in **Figure 2.6D**.

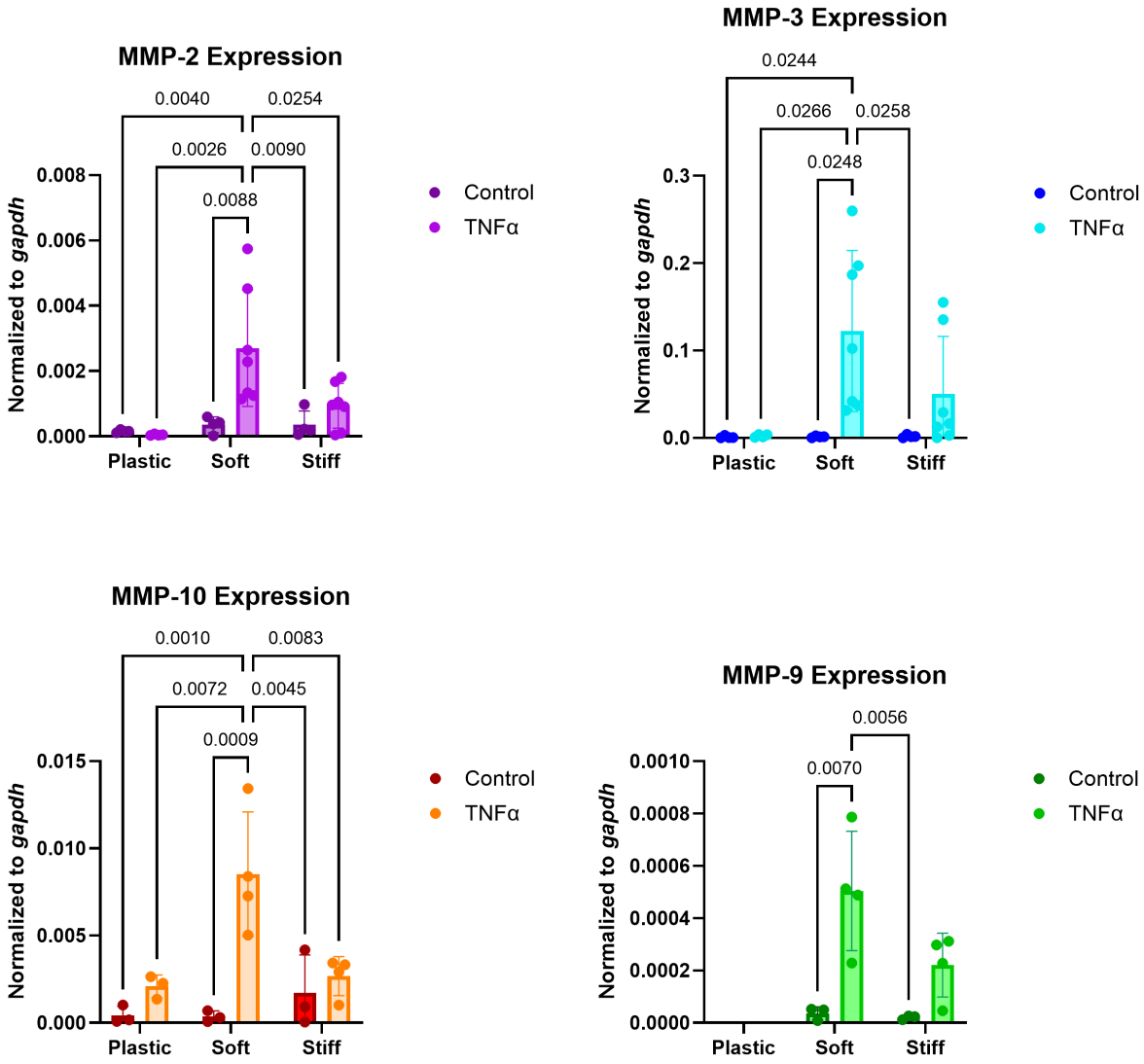

Figure 2.6: MMP Expressions in Plastics and Gel-Encapsulated MSCS, significance established by Two-Way Anova and confirmed with Tukey's post-hoc HSD. (A) MMP-2 expression is significantly upregulated in the soft gel with inflammation factor (soft TNF-α) compared to the plastic control (p = 0.0050), the plastic TNF-α (p = 0.0032), the soft control (p = 0.0114), and the stiff control (p = 0.0117). Significance was also established between the soft TNF-α and the stiff TNF-α (p = 0.0350). (B) MMP-3 expression is significantly upregulated in the soft gel with inflammation factor (soft TNF-α) compared to the plastic control (p = 0.0244), plastic TNF-α (p = 0.0266), the soft control (p = 0.0248), and the stiff control (p = 0.0258). No significance established between the soft TNF-α and stiff TNF-α. The scale at which MMP-3 was upregulated was much larger than in other MMPs. (C) MMP-9 expression is significantly upregulated in the soft gel with inflammation factor (soft TNF-α) compared to the and the soft control (p = 0.0070) and stiff control (p = 0.0056). No significance was established between the soft TNF-α and stiff TNF-α. MMP-9 plastic control and TNF-α data obtained at this time did not fit inclusion criteria. (D) MMP-10 expression is significantly upregulated in the soft gel with inflammation factor (soft TNF-α) when compared to the plastic control (p = 0.0010), plastic TNF-α (p = 0.0072), soft control (p = 0.0009) and the stiff control (p = 0.0045). Significance was also established between the soft TNF-α and the stiff TNF-α (p = 0.0083). Note. All graphs visualized in GraphPad Prism.

2.10 MMP-3 ELISA Results

To assess the levels of MMP-3 secreted into culture media, an ELISA was performed, with standard curves generated for production comparison. **Figure B.1** in Appendix B displays the three standard curves generated from known concentrations of MMP-3 across the three studies, along with raw absorbance values and calculated concentrations. The resulting standard curve exhibited a strong linear relationship between absorbance and concentration. All sample analyses were performed in duplicate.

MMP-3 concentrations were measured in culture media collected from plastic cultures treated with either pure media or TNF-α, as well as from soft and stiff hydrogels incubated with and without TNF-α. The results are summarized in **Figure 2.7**, which shows the mean MMP-3 concentrations across all conditions.

A two-way ANOVA was performed to examine the effects of gel encapsulation and TNF-α treatment on MMP-3 production. The analysis revealed significant main effects of both factors and a significant interaction. Specifically, the row factor (gel encapsulation) was significant ($F(2, 26) = 8.850$, $p = 0.0012$), the column factor (TNF-α vs. Control) was highly significant ($F(1, 26) = 47.07$, $p < 0.0001$), and the interaction between the two factors was also significant ($F(2, 26) = 8.272$, $p = 0.0017$). These findings indicate that TNF-α treatment strongly increased MMP-3 production and that this effect varied depending on gel encapsulation. The predicted least squares mean for the control group was 0.1406, while TNF-α was 4.270, with a mean difference of –4.129 (95% CI: -5.367 to –2.892), confirming a substantial TNF-α-driven increase. To identify which specific groups differed, a post hoc analysis using Tukey's HSD test was conducted.

Tukey's HSD post hoc analysis revealed significant pairwise differences between the soft gel with TNF-α (soft TNF-α) and the plastic control ($p < 0.0001$), as well as the plastic TNF-α group ($p = 0.0003$), indicating that gel encapsulation is necessary for upregulation. Additionally, the soft TNF-α group differed significantly from the soft control ($p < 0.0001$) and the stiff control ($p < 0.0001$), highlighting the impact of the inflammatory factor on MMP-3 expression. The stiff TNF-

α group also showed significant differences when compared to the plastic control ($p < 0.0001$), plastic TNF-α ($p = 0.0002$), soft control ($p < 0.0001$) and stiff control ($p < 0.0001$).

No significant differences were observed between the plastic control and plastic TNF-α groups, nor between either plastic group and the soft or stiff controls. Furthermore, no significant difference was found between the soft TNF-α and stiff TNF-α groups, suggesting that matrix stiffness may not influence MMP-3 expression, consistent with qPCR results. These results suggest that encapsulation within a matrix and the presence of an inflammatory factor may elicit significant MMP-3 upregulation, while matrix stiffness alone does not appear to have an effect. Results are illustrated in **Figure 2.7**.

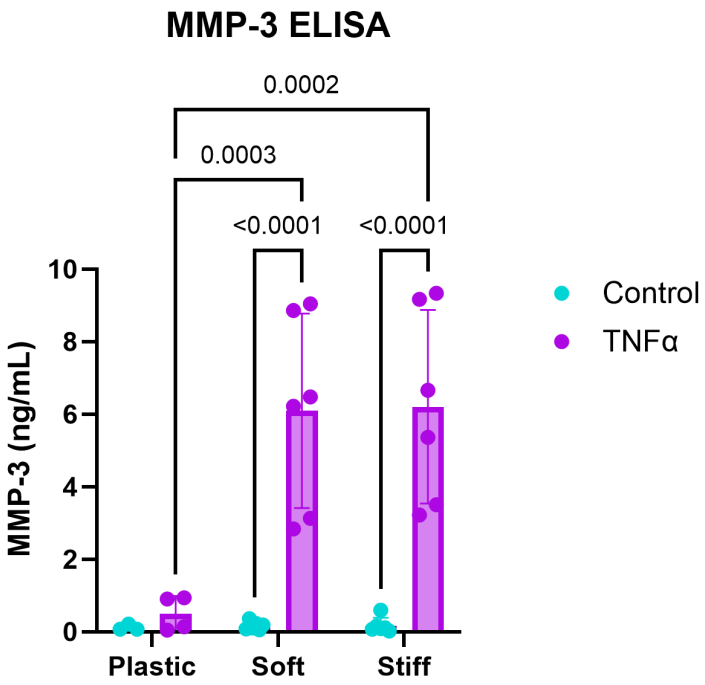

Figure 2.7: MMP-3 ELISA Assay Results. Statistical analysis using two-way ANOVA revealed revealed significant main effects of row factor (gel encapsulation) ($F(2, 26) = 8.850$, $p = 0.0012$), column factor (TNF-α vs. Control) ($F(1, 26) = 47.07$, $p < 0.0001$), and interaction between factors ($F(2, 26) = 8.272$, $p = 0.0017$). Tukey's HSD post hoc analysis revealed significant pairwise differences between the soft gel with TNF-α (soft TNF-α) and the plastic control ($p < 0.0001$), plastic TNF-α group ($p = 0.0003$), soft control ($p < 0.0001$) and the stiff control ($p < 0.0001$). The stiff TNF-α group also showed significant differences when compared to the plastic control ($p < 0.0001$), plastic TNF-α ($p = 0.0002$), soft control ($p < 0.0001$) and stiff control ($p < 0.0001$). No significance was established between the soft TNF-α and stiff TNF-α groups.

2.11 Discussion

To initiate this phase of the project, it was essential to characterize alginate hydrogel mechanics in order to establish a range of stiffness values suitable for evaluating MSC responses to soft versus stiff microenvironments. Compression testing was performed on alginate hydrogels formulated with varying concentrations of $CaSO_4$, a crosslinking agent that modulates gel stiffness through ionic interactions[3]. Hydrogels meeting the minimum criteria for uniformity and integrity were selected for mechanical testing, with $CaSO_4$ concentrations ranging from 15 mM to 40 mM in 5 mM increments.

Stress-strain curves generated from compression testing allowed for the calculation of Young's modulus at 10% strain, a region within the linear elastic range of the material. Results demonstrated a clear trend: increasing $CaSO_4$ concentration led to a progressive rise in Young's modulus, indicating enhanced network stiffness due to increased ionic crosslinking density. This confirmed that $CaSO_4$ concentration is a reliable parameter for tuning alginate hydrogel stiffness.

The difference in stiffness between the softest and stiffest gels was statistically significant, providing a sufficient mechanical contrast for downstream analysis of MSC behavior. This qualitatively and quantitatively determined mechanical range was deemed appropriate for modeling soft and stiff microenvironments, in turn representing healthy and fibrotic tissue stiffness profiles, which are known to influence MSC fate decisions and cytokine secretion[5,6,7].

Prior literature reports an anticipated hydrogel stiffness range of approximately 9–15 kPa, depending on formulation and measurement methodology[15]. While the stiffness values obtained in this study fall slightly below this reported range, they are substantially closer to the expected physiological regime than earlier measurements and, importantly, exhibit a clear and statistically significant distinction between the defined soft and stiff hydrogel conditions. This mechanically distinct separation, though modest in magnitude, was sufficient to induce observable changes in MSC behavior, emphasizing the sensitivity of these cells to relatively small variations in matrix stiffness.

These findings support the suitability of the selected $CaSO_4$ concentrations for systematically modulating the mechanical microenvironment in this hydrogel system. As such, the ability to reproducibly generate distinct soft and stiff conditions is functionally meaningful for probing mechanobiological responses. Collectively, these results underscore the importance of precise mechanical characterization in biomaterials research, particularly when linking material properties to cell behavior. Accurate and reproducible stiffness measurements are essential for interpreting mechanobiological outcomes, enabling cross-study comparisons, and ensuring the translational relevance of engineered extracellular matrix analogs.

qPCR was employed to assess the expression of MMPs in MSCs cultured on plastic and within alginate hydrogels of varying stiffness, both with and without the inflammatory cytokine TNF-α. This analysis aimed to determine whether hydrogel encapsulation and inflammatory stimulation influence MSC behavior, particularly in the expression of ECM-remodeling enzymes.

MMP-2 expression was significantly upregulated in the soft TNF-α group compared to both plastic control and plastic TNF-α groups, indicating that gel encapsulation is necessary for up-regulation. Furthermore, soft TNF-α samples showed significantly higher expression than soft and stiff controls, suggesting that inflammatory stimulation in combination with a soft matrix enhances MMP-2 expression. A significant difference between soft TNF-α and stiff TNF-α groups further implies that matrix softness may potentiate MMP-2 expression. No significant differences were observed between plastic control and plastic TNF-α, or between stiff control and stiff TNF-α, reinforcing the importance of both encapsulation and matrix compliance.

MMP-3 expression followed a similar trend. The soft TNF-α group showed significant upregulation compared to plastic control, plastic TNF-α, soft control, and stiff control, again highlighting the combined effect of encapsulation and inflammation. However, no significant difference was observed between soft TNF-α and stiff TNF-α groups, suggesting that matrix stiffness may not influence MMP-3 expression. Notably, the magnitude of MMP-3 upregulation was substantially higher than that of the other MMPs, indicating a potentially dominant role for MMP-3 in ECM modulation under these conditions.

MMP-9 expression was significantly elevated in the soft TNF-α group compared to soft and stiff controls, supporting the role of inflammatory stimulation in driving expression. However, no significant difference was found between soft TNF-α and stiff TNF-α groups, again suggesting that matrix stiffness may not be a key regulator of MMP-9 expression. Due to technical issues, data from plastic control and plastic TNF-α groups did not meet inclusion criteria. Despite this limitation, the current data suggest that encapsulation and inflammation together promote MMP-9 expression, independent of stiffness.

MMP-10 expression was significantly higher in the soft TNF-α group compared to plastic control, soft control and stiff control, indicating that both encapsulation and inflammatory signaling are necessary for upregulation. Additionally, a significant difference between soft TNF-α and stiff TNF-α groups suggests that a softer matrix may further enhance MMP-10 expression. No significant differences were observed between plastic control and plastic TNF-α groups, or between stiff control and stiff TNF-α, reinforcing the importance of the combined mechanical and biochemical cues.

During method development, several technical challenges were encountered. Initially, alginate digestion for RNA extraction was performed using alginate lyase, but this approach yielded inconsistent and low-quality qPCR results. A serendipitous substitution with EDTA, due to a temporary shortage of alginate lyase, resulted in markedly improved data quality. It is attributed that EDTA, by chelating calcium ions and rapidly disrupting ionic crosslinks, preserves the cellular transcriptomic state more effectively than the slower enzymatic digestion by alginate lyase, which may allow cells to adapt to the changing microenvironment during processing[16,17].

While each MMP exhibited distinct expression patterns, a consistent trend emerged: encapsulation within alginate hydrogels combined with TNF-α stimulation led to upregulation of MMPs, particularly in softer matrices. Although the influence of matrix stiffness was not uniform across all MMPs—being more pronounced in MMP-2 and MMP-10—these findings suggest that softer hydrogels may be more effective in promoting ECM-modulating activity in MSCs, which is critical for applications targeting fibrotic tissue remodeling.

The quantification of MMP-3 levels in culture media using ELISA revealed that a combination of gel encapsulation and the presence of an inflammatory factor (TNF-α) is necessary for significant upregulation of MMP-3. These results suggest that modifying the MSC microenvironment, particularly through mechanical confinement and inflammatory signaling, can influence cell behavior and cytokine output—specifically MMP-3, as observed in this study.

While the ELISA assay successfully quantified MMP-3 levels, it does not differentiate between the active and inactive (pro-form) of the enzyme[18]. MSCs typically secrete MMP-3 in its latent form, which requires activation, often via physiological mechanisms such as proteolytic cleavage or exposure to activating agents like 4-aminophenylmercuric acetate (APMA)[19,20]. Activated MMP-3 plays a critical role in ECM remodeling, with known degradative effects on fibronectin, collagen, and gelatin, all of which are commonly upregulated in fibrotic conditions, particularly within skeletal muscle[11,14,21].

Given that fibronectin deposition precedes and regulates collagen deposition[10,11,12,13], increased MMP-3 activity in fibrotic tissue may help resolve or prevent progression of fibrosis. This therapeutic implication elucidates the importance of not only quantifying MMP-3 but also assessing its functional activity. Therefore, a follow-up functionality assay investigating the capabilities of MSC-derived MMP-3 is necessary to evaluate its degradative potential on fibronectin.

These results contribute to a growing body of evidence supporting the use of mechanically tunable hydrogels and inflammatory cues to direct MSC behavior. Future studies will aim to validate these findings by correlating gene expression data with protein-level activity through functional assays, which is essential to fully understand the therapeutic potential of MSC-derived MMPs in regenerative medicine.

References

[1] U. Galderisi, G. Peluso, and G. Di Bernardo. "Clinical Trials Based on Mesenchymal Stromal Cells are Exponentially Increasing: Where are We in Recent Years?" In: *Stem Cell Reviews and Reports* 18.1 (2022), pp. 23–36. DOI: 10.1007/s12015-021-10231-w. URL: https://doi.org/10.1007/s12015-021-10231-w.

[2] F. M. Watt and W. T. S. Huck. "Role of the extracellular matrix in regulating stem cell fate". In: *Nature Reviews Molecular Cell Biology* 14.8 (2013), pp. 467–473. DOI: 10.1038/nrm3620. URL: https://doi.org/10.1038/nrm3620.

[3] K. Y. Lee and D. J. Mooney. "Alginate: Properties and biomedical applications". In: *Progress in Polymer Science* 37.1 (2012), pp. 106–126. DOI: 10.1016/j.progpolymsci.2011.06.003. URL: https://doi.org/10.1016/j.progpolymsci.2011.06.003.

[4] S. N. Pawar and K. J. Edgar. "Alginate derivatization: A review of chemistry, properties and applications". In: *Biomaterials* 33.11 (2012), pp. 3279–3305. DOI: 10.1016/j.biomaterials.2012.01.007. URL: https://doi.org/10.1016/j.biomaterials.2012.01.007.

[5] S. W. Wong et al. "Inhibition of aberrant tissue remodelling by mesenchymal stromal cells singly coated with soft gels presenting defined chemomechanical cues". In: *Nature Biomedical Engineering* 6.1 (2022), pp. 54–66. DOI: 10.1038/s41551-021-00740-x. URL: https://doi.org/10.1038/s41551-021-00740-x.

[6] S. W. Wong et al. "Controlled Deposition of 3D Matrices to Direct Single Cell Functions". In: *Advanced Science* 7.20 (2020), p. 2001066. DOI: 10.1002/advs.202001066. URL: https://doi.org/10.1002/advs.202001066.

[7] S. Barbon et al. "Mesenchymal stromal cell-laden hydrogels in tissue regeneration: Insights from preclinical and clinical research". In: *Frontiers in Pharmacology* 16 (2025), p. 1670649. DOI: 10.3389/fphar.2025.1670649. URL: https://doi.org/10.3389/fphar.2025.1670649.

[8] L. Wang and J. P. Stegemann. “Extraction of high quality RNA from polysaccharide matrices using cetyltrimethylammonium bromide”. In: *Biomaterials* 31.7 (2010), pp. 1612–1618. DOI: 10.1016/j.biomaterials.2009.11.024. URL: https://doi.org/10.1016/j.biomaterials.2009.11.024.

[9] A. Javaid et al. “Extraction of High-Quality Genomic DNA from Plants Using Modified CTAB-Based Method”. In: *Detection of Plant Viruses: Advanced Techniques*. Ed. by A. Hamid et al. Springer US, 2025, pp. 69–75. DOI: 10.1007/978-1-0716-4390-7_13. URL: https://doi.org/10.1007/978-1-0716-4390-7_13.

[10] T. Velling et al. “Polymerization of Type I and III Collagens Is Dependent On Fibronectin and Enhanced By Integrins $\alpha 11\beta 1$and $\alpha 2\beta 1$*”. In: *Journal of Biological Chemistry* 277.40 (2002), pp. 37377–37381. DOI: 10.1074/jbc.M206286200. URL: https://doi.org/10.1074/jbc.M206286200.

[11] “Collagen I matrix turnover is regulated by fibronectin polymerization”. In: *American Journal of Physiology - Cell Physiology* 297.5 (2009). DOI: 10.1152/ajpcell.00341.2009. URL: https://doi.org/10.1152/ajpcell.00341.2009.

[12] J. Sottile and D. C. Hocking. “Fibronectin Polymerization Regulates the Composition and Stability of Extracellular Matrix Fibrils and Cell-Matrix Adhesions”. In: *Molecular Biology of the Cell* 13.10 (2002), pp. 3546–3559. DOI: 10.1091/mbc.E02-01-0048. URL: https://doi.org/10.1091/mbc.E02-01-0048.

[13] “Role of fibronectin in collagen deposition: Fab’ to the gelatin-binding domain of fibronectin inhibits both fibronectin and collagen organization in fibroblast extracellular matrix”. In: *The Journal of Cell Biology* 92.2 (1982), pp. 485–492. DOI: 10.1083/jcb.92.2.485. URL: https://doi.org/10.1083/jcb.92.2.485.

[14] M. Chang. “Matrix metalloproteinase profiling and their roles in disease”. In: *RSC Advances* 13.9 (2023), pp. 6304–6316. DOI: 10.1039/d2ra07005g. URL: https://doi.org/10.1039/d2ra07005g.

[15] D. E. Discher, D. J. Mooney, and P. W. Zandstra. “Growth Factors, Matrices, and Forces Combine and Control Stem Cells”. In: *Science* 324.5935 (2009), pp. 1673–1677. DOI: 10.1126/science.1171643. URL: https://doi.org/10.1126/science.1171643.

[16] Ioanna N. Besiri et al. “Experimental Advances in the Real-Time Recording of Cross-Linking Alginate In Situ Gelation: A Review”. In: *Polymers* 15.13 (2023), p. 2875. DOI: 10.3390/polym15132875.

[17] Daniele Mattei et al. “Enzymatic Dissociation Induces Transcriptional and Proteotype Bias in Brain Cell Populations”. In: *International Journal of Molecular Sciences* 21.21 (2020), p. 7944. DOI: 10.3390/ijms21217944.

[18] Thermo Fisher Scientific. *Human MMP3 ELISA Kit (BMS2014-3)*. https://www.thermofisher.com/elisa/product/Human-MMP3-ELISA-Kit/BMS2014-3. Sandwich ELISA for quantification of human MMP-3 in serum, plasma, and cell culture medium. 2026.

[19] X. Zhang et al. “A Comparative Study of Fibronectin Cleavage by MMP-1, -3, -13, and -14”. In: *Cartilage* 3.3 (2012), pp. 267–277. DOI: 10.1177/1947603511435273. URL: https://doi.org/10.1177/1947603511435273.

[20] G. Galazka et al. “APMA (4-Aminophenylmercuric Acetate) Activation of Stromelysin-1 Involves Protein Interactions in Addition to Those with Cysteine-75 in the Propeptide”. In: *Biochemistry* 35.34 (1996), pp. 11221–11227. DOI: 10.1021/bi960618e. URL: https://doi.org/10.1021/bi960618e.

[21] T. Assis-Ribas et al. “Extracellular matrix dynamics during mesenchymal stem cells differentiation”. In: *Developmental Biology* 437.2 (2018), pp. 63–74. DOI: 10.1016/j.ydbio.2018.03.002. URL: https://doi.org/10.1016/j.ydbio.2018.03.002.

Chapter 3

Evaluate the Functionality of Engineered MSC Secretome *in vitro*

3.1 Introduction

Given the significant upregulation of MMP-3 observed in the qPCR results, and its known role in extracellular matrix remodeling, it was important to evaluate its functional activity. Fibronectin was selected as a target due to its role as an early ECM component that regulates collagen deposition during fibrosis[1,2,3,4]. Therefore, assessing the ability of MSC-secreted MMP-3 to degrade fibronectin provides key insight into its potential to disrupt early fibrotic processes and limit downstream matrix accumulation.

Following MMP-3 protein analysis, an attempt was made to modify a second solid-phase sandwich ELISA kit to detect fibronectin. This kit required protocol modifications, as it was repurposed for a functional assay, specifically, to observe and quantify fibronectin degradation mediated by MMPs present in the conditioned culture media surrounding the gel-encapsulated MSCs. This application differed from the kit's standard use, which typically involves measuring fibronectin concentration rather than its degradation.

3.2 Fibronectin Degradation Assay

3.2.1 Modified Fibronectin ELISA kit

Following the quantification of MMP-3 levels in the samples, a functionality assay was conducted to evaluate the activity of secreted MMP-3 and other cytokines from gel-encapsulated cells in degrading fibronectin. To achieve this, the standard protocol of a fibronectin ELISA kit was adapted to create a simplified degradability assay with reduced time requirements compared to conventional methods. The Mouse Fibronectin ELISA Kit (Invitrogen, Thermo Fisher Scientific;

Cat No. EEL096) was selected for this purpose. While the kit itself remained unmodified, the protocol was altered and additional reagents were introduced prior to use.

Literature review informed the appropriate MMP-3 to fibronectin ratio for analysis[5], and the calculations for sample and fibronectin standard volumes are discussed below. As outlined in Chapter 1, MMPs secreted by gel-encapsulated MSCs are initially in their inactive pro-form, rendering them incapable of ECM degradation[6]. Literature also supports the use of p-aminophenylmercuric acetate (APMA) buffer to activate latent MMPs[5,7]. By activating the pro-MMPs present in the culture media from gel-encapsulated cells, the functional capacity of these enzymes to degrade fibronectin could be assessed using the modified ELISA protocol. The extent of fibronectin degradation was then quantified against a set of standards.

3.2.2 Modified Incubation Protocol/APMA

To activate latent MMPs, a buffer solution was prepared containing 50 mM Tris-HCl, 10 mM $CaCl_2$ (Spectrum Chemical, Cat. No. C1096), 150 mM NaCl, 0.05% Brij-35 (Brij® 35, Sigma-Aldrich, Cat. No. 801962), and deionized water. All components were mixed under sterile conditions and filtered through a 0.22 µm syringe filter into a sterile 15 mL conical tube. The pH of the solution was adjusted to 7.4-7.5 using a pH meter. The buffer was then filtered again through a 0.22 µm syringe filter under sterile conditions. Fresh buffer was prepared from stock solutions for each use each and was not stored.

To prepare 1 mL of 100 mM APMA stock solution, 35.18 mg of APMA powder (MW = 351.8 g/mol, MedChemExpress, Cat. No. HY-148905) was dissolved in 1 mL of DMSO. The stock solution was stored at $-20°$C and protected from light.

For activation, the final APMA concentration in the buffer was 2 mM, achieved by adding 20 µL of the 100 mM APMA stock to 980 µL of activation buffer. For six of the eight experimental samples (plastic control, plastic TNF-α, soft control, soft TNF-α, stiff control, and stiff TNF-α), 1 mL of sample was mixed in a 1:1 ratio with the APMA-containing activation buffer. This dilution

reduced the final APMA concentration to 1 mM and halved the MMP-3 concentration in the soft and stiff TNF-α samples to 3 ng/mL, based on ELISA results.

A positive control using recombinant MMP-3 (R&D Systems, Cat. No. 548-MM) was prepared similarly. Recombinant MMP-3 was first diluted to 100 µg/mL by adding 100 µL of activation buffer (without APMA) to the received vial. To prepare 2 mL of activated recombinant MMP-3, 20 µL of the 100 µg/mL stock and 20 µL of 100 mM APMA stock were added to 1.96 mL of activation buffer, resulting in final concentrations of 1 mM APMA and 1 ng/µL recombinant MMP-3.

All seven samples were incubated for 1.5 hours at 37°C in a 5% CO_2 atmosphere. Following incubation, samples were placed on ice to halt APMA activity.

3.2.3 Filtration

To remove APMA following incubation, 10 kDa molecular weight cut-off (MWCO) spin filters (Thermo Scientific, Cat. No. 88517) were employed. Filters were first equilibrated by adding 300 µL of activation buffer (without APMA) and centrifuging at 14,000 × g for 1 minute. The flow-through was discarded. Then, 2 mL of each activated sample was transferred into the top chamber of its respective filter unit. Samples were centrifuged until approximately 100 µL remained (~25 minutes). The filtrate was discarded and 400 µL of activation buffer was added to the top chamber for a second wash, followed by centrifugation to ~100 µL. This washing process was repeated a total of three times.

After the final wash, samples were recovered by adding 500 µL of fresh activation buffer, restoring them to their original concentrations (0.006 ng/µL for experimental samples). The final concentration of recombinant MMP-3 was adjusted to 0.250 ng/µL.

3.2.4 Incubation Protocol

A literature review was conducted to determine the appropriate MMP-3 to fibronectin ratio for meaningful analysis[5]. The fibronectin standard supplied with the ELISA kit was reconstituted in

Standard & Sample Diluent according to the manufacturer's protocol, yielding a final concentration of 0.10 ng/µL.

For each of the eight experimental conditions, 40.80 µL of either conditioned culture media, recombinant MMP-3, or untreated culture media was added to 175 µL of the reconstituted fibronectin solution. These mixtures were incubated at 37°C in a 5% CO_2 atmosphere for 24 hours.

3.2.5 Fibronectin ELISA Assay Procedure

Following incubation, ELISA was performed with a minor modification to the standard curve generation protocol. In the original ELISA procedure, serial dilutions were conducted using a two-fold (1:2) dilution scheme. This involved combining 500 µL of the starting standard solution (100 ng/mL) with 500 µL of Standard & Sample Diluent in 1.5 mL microcentrifuge tubes. The process was repeated sequentially across six dilution steps, resulting in final concentrations of 100, 50, 25, 12.5, 6.25, 3.13 and 1.56 ng/mL. A seventh tube containing only diluent served as the blank.

To reduce reagent consumption and accommodate the limited standard volume remaining from earlier steps, the protocol was modified to use 150 µL of standard and 150 µL of diluent per dilution step. This adjustment maintained the same dilution factor and produced a standard curve that was consistent and fell within expected ranges during subsequent absorbance readings.

For the assay, 100 µL of standards, blanks, and duplicate samples were added to the designated wells, as illustrated in **Figure 3.3**. The plate was sealed with the provided plate sealer and incubated for 90 minutes at 37°C. After incubation, the plate was aspirated, and 100 µL of Biotinylated Detection Antibody Working Solution was added to each well. The plate was resealed and incubated for an additional 60 minutes at 37°C.

Following this, the plate was aspirated and washed three times with 350 µL of 1 × Wash Buffer, allowing the buffer to sit in the wells for one minute before each aspiration. After the third wash, 100 µL of HRP Conjugate Working Solution was added to each well, and the plate was incubated for 30 minutes. The plate was then aspirated and washed five times using the same procedure.

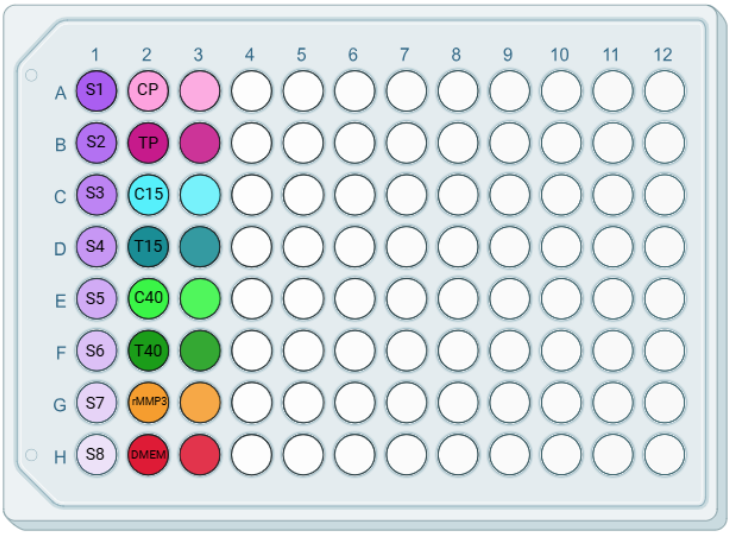

Figure 3.1: Fibronectin ELISA plate layout for a single experiment containing a standard curve (purple), plastic control (light pink), plastic TNF-α (dark pink), soft gel control (light blue), soft gel TNF-α (dark blue), stiff gel control (light green), stiff gel TNF-α (dark green), recombinant MMP-3 (orange), and untreated culture media (red). All samples were performed in duplicate.

After the final wash, 90 µL of Substrate Reagent was added to each well. The plate was resealed and incubated for approximately 15 minutes, protected from light. Once sufficient color development was observed, 50 µL of Stop Solution was added to each well in the same order as the substrate addition, halting the enzymatic reaction and changing the color from blue to yellow. The plate was gently tapped to mix, and absorbance was immediately read at 450 nm using a microplate reader.

Raw absorbance values were exported to Excel for analysis. Standard curves were generated and equations solved using the same approach as described in the MMP-3 ELISA analysis.

3.2.6 Results

The results obtained from this portion of the study were ultimately inconclusive, as the adapted *in vitro* assay failed to yield consistent or interpretable measurements of fibronectin degradation. Significant variability across replicates, combined with insufficient assay sensitivity, limited the ability to directly evaluate enzymatic activity within the MSC secretome under controlled conditions. These technical challenges likely stemmed from a combination of factors, including the

complexity of extracellular matrix protein degradation, potential interference from assay components, and constraints associated with recapitulating proteolytic dynamics in simplified *in vitro* systems.

Given these limitations, further optimization of the assay was deemed impractical within the scope of the study. Consequently, the experimental focus shifted toward *in vivo* models, where the biological activity of the MSC secretome could be assessed within a physiologically relevant microenvironment that more accurately reflects native matrix remodeling processes. This transition enabled evaluation of secretome function in the context of endogenous enzymatic regulation, cell–matrix interactions, and tissue-level feedback mechanisms that are difficult to replicate *in vitro*. While the *in vitro* findings did not permit definitive conclusions regarding fibronectin degradation, they informed the strategic decision to prioritize *in vivo* experimentation as a more robust and biologically meaningful approach for characterizing MSC-mediated matrix remodeling.

3.3 Discussion

The quantification of MMP-3 levels in culture media using ELISA revealed that a combination of gel encapsulation and the presence of an inflammatory factor (TNF-α) is necessary for significant upregulation of MMP-3. These results suggest that modifying the MSC microenvironment, particularly through mechanical confinement and inflammatory signaling, can influence cell behavior and cytokine output—specifically MMP-3, as observed in this study.

These findings align with previous studies, such as those by Wong et al., which report that mechanobiological interventions can enhance cytokine secretion from MSCs[8,9,10]. Such evidence supports the broader concept that mechanobiology can be leveraged to tailor MSC behavior, potentially enabling therapeutic modulation of the microenvironment in regenerative medicine applications.

Although MMP-3 concentrations were successfully measured, the assay does not provide information regarding enzyme activation state[11]. This distinction is important because MSC-derived MMP-3 is typically secreted as an inactive zymogen that must undergo activation before partic-

ipating in matrix degradation[5,7]. Therefore, elevated MMP-3 levels do not necessarily indicate increased proteolytic activity. Active MMP-3 can cleave several matrix components, including fibronectin, collagen, and gelatin, and has been implicated in the regulation of fibrotic extracellular matrix remodeling[2,6,12]

Given the established role of fibronectin as a precursor to collagen-rich fibrotic matrix formation[1,2,3,4], enzymes capable of degrading fibronectin may influence fibrosis resolution. This relationship underscores the importance of assessing MMP-3 activity in addition to protein abundance. Accordingly, the degradative capacity of activated MMP-3 toward fibronectin was examined in a dedicated functional assay.

To address this limitation, multiple iterations of a commercially available fibronectin ELISA were explored with the goal of adapting the assay to detect MMP–mediated degradation of fibronectin. These efforts included modifications to assay conditions and detection strategies intended to capture proteolytic breakdown products rather than total fibronectin content. Despite extensive optimization attempts, the adapted assay failed to yield consistent or interpretable measurements, thereby precluding reliable quantification of enzymatic activity within the MSC secretome. The technical challenges encountered highlight the difficulty of repurposing endpoint binding assays to assess dynamic extracellular matrix degradation processes *in vitro*.

Given these constraints, the study pivoted toward *in vivo* experimentation, where the functional impact of the MSC secretome could be evaluated within a physiologically relevant tissue environment. This approach enabled assessment of secretome activity in the context of native matrix architecture, endogenous protease regulation, and complex cell–matrix interactions that are not readily replicated in simplified *in vitro* systems. As such, the transition to *in vivo* studies provided a more biologically informative framework for investigating MSC-mediated matrix remodeling.

References

[1] T. Velling et al. “Polymerization of Type I and III Collagens Is Dependent On Fibronectin and Enhanced By Integrins $\alpha 11\beta 1$and $\alpha 2\beta 1$*”. In: *Journal of Biological Chemistry* 277.40 (2002), pp. 37377–37381. DOI: 10.1074/jbc.M206286200. URL: https://doi.org/10.1074/jbc.M206286200.

[2] “Collagen I matrix turnover is regulated by fibronectin polymerization”. In: *American Journal of Physiology - Cell Physiology* 297.5 (2009). DOI: 10.1152/ajpcell.00341.2009. URL: https://doi.org/10.1152/ajpcell.00341.2009.

[3] J. Sottile and D. C. Hocking. “Fibronectin Polymerization Regulates the Composition and Stability of Extracellular Matrix Fibrils and Cell-Matrix Adhesions”. In: *Molecular Biology of the Cell* 13.10 (2002), pp. 3546–3559. DOI: 10.1091/mbc.E02-01-0048. URL: https://doi.org/10.1091/mbc.E02-01-0048.

[4] “Role of fibronectin in collagen deposition: Fab’ to the gelatin-binding domain of fibronectin inhibits both fibronectin and collagen organization in fibroblast extracellular matrix”. In: *The Journal of Cell Biology* 92.2 (1982), pp. 485–492. DOI: 10.1083/jcb.92.2.485. URL: https://doi.org/10.1083/jcb.92.2.485.

[5] X. Zhang et al. “A Comparative Study of Fibronectin Cleavage by MMP-1, -3, -13, and -14”. In: *Cartilage* 3.3 (2012), pp. 267–277. DOI: 10.1177/1947603511435273. URL: https://doi.org/10.1177/1947603511435273.

[6] M. Chang. “Matrix metalloproteinase profiling and their roles in disease”. In: *RSC Advances* 13.9 (2023), pp. 6304–6316. DOI: 10.1039/d2ra07005g. URL: https://doi.org/10.1039/d2ra07005g.

[7] G. Galazka et al. “APMA (4-Aminophenylmercuric Acetate) Activation of Stromelysin-1 Involves Protein Interactions in Addition to Those with Cysteine-75 in the Propeptide”. In: *Biochemistry* 35.34 (1996), pp. 11221–11227. DOI: 10.1021/bi960618e. URL: https://doi.org/10.1021/bi960618e.

[8] S. W. Wong et al. “Soft extracellular matrix enhances inflammatory activation of mesenchymal stromal cells to induce monocyte production and trafficking”. In: *Science Advances* 6.15 (2020), eaaw0158. DOI: 10.1126/sciadv.aaw0158. URL: https://doi.org/10.1126/sciadv.aaw0158.

[9] S. W. Wong et al. “Inhibition of aberrant tissue remodelling by mesenchymal stromal cells singly coated with soft gels presenting defined chemomechanical cues”. In: *Nature Biomedical Engineering* 6.1 (2022), pp. 54–66. DOI: 10.1038/s41551-021-00740-x. URL: https://doi.org/10.1038/s41551-021-00740-x.

[10] S. W. Wong et al. “Controlled Deposition of 3D Matrices to Direct Single Cell Functions”. In: *Advanced Science* 7.20 (2020), p. 2001066. DOI: 10.1002/advs.202001066. URL: https://doi.org/10.1002/advs.202001066.

[11] Thermo Fisher Scientific. *Human MMP3 ELISA Kit (BMS2014-3)*. https://www.thermofisher.com/elisa/product/Human-MMP3-ELISA-Kit/BMS2014-3. Sandwich ELISA for quantification of human MMP-3 in serum, plasma, and cell culture medium. 2026.

[12] T. Assis-Ribas et al. “Extracellular matrix dynamics during mesenchymal stem cells differentiation”. In: *Developmental Biology* 437.2 (2018), pp. 63–74. DOI: 10.1016/j.ydbio.2018.03.002. URL: https://doi.org/10.1016/j.ydbio.2018.03.002.

Chapter 4

Evaluate the Therapeutic Efficacy of Engineered MSC Secretome on Rodent Muscle Fibrosis

4.1 Introduction

Following the inconclusive *in vitro* degradation assay results, the study transitioned to evaluating the biological effects of the MSC secretome *in vivo*. Conditioned culture media enriched in MSC-derived MMPs were directly injected into murine skeletal muscle to assess their impact on tissue remodeling. Behavioral performance was quantified using AnyMaze to identify functional changes following treatment. Muscle tissues were then harvested and analyzed using Masson's trichrome staining to assess collagen deposition and immunohistochemistry (IHC) to evaluate fibronectin content, enabling detailed characterization of extracellular matrix (ECM) remodeling at both the histological and molecular levels. Quantification of these histological results was performed using custom ImageJ analysis code.

Histological analysis is a critical tool for evaluating tissue architecture, ECM composition, and biological responses to engineered therapeutics and biomaterials. Both qualitative and quantitative assessments provide insight into inflammatory, fibrotic, and regenerative processes that occur following administration of novel treatments. In this chapter, trichrome staining and immunohistochemistry are employed to examine collagen and fibronectin content in murine skeletal muscle tissue, both before and after treatment with engineered MSC derived conditioned media.

By integrating molecular assays, *in vivo* behavioral analysis, and comprehensive histological and immunohistochemical evaluation, this chapter establishes a framework for determining how conditioned media derived from mechanically tuned, inflammation preconditioned MSCs may influence ECM turnover, reduce fibrosis, and promote muscle regeneration. Ultimately, these find-

ings provide foundational evidence to inform future development of MSC based therapeutic strategies targeting muscle fibrosis and tissue repair.

4.2 Animal Handling

All animal procedures were conducted in accordance with the guidelines established by Colorado State University (CSU) and were approved by the Institutional Animal Care and Use Committee (IACUC Protocol #7497). Female wild-type DBA (DBA/2J mice, JAX® Stock No. 000671; The Jackson Laboratory, Bar Harbor, ME) and dystrophin-deficient mdx (D2.B10-Dmd mdx/J mice, JAX® Stock No. 013141; Jackson Laboratory, Bar Harbor, ME) mice were used in this study to evaluate baseline tissue responses. Mice were housed under standard laboratory conditions with ad libitum access to food and water.

4.2.1 Home Cage Activity Monitoring Using AnyMaze

Adult female mice of both strains were used for all behavioral experiments. Home cage activity was assessed using the animals' standard home cages placed within an AnyMaze imaging enclosure. Prior to testing, all mice were removed from their home cage and transferred to a temporary holding cage with access to food and water. Loose bedding enrichment (e.g., paper shreds) was removed to prevent interference with automated tracking.

A rectangular red plastic shelter (hut) was included in the cage, and a white laminated cover was affixed to the top of the hut using double sided tape to improve contrast for video tracking. The prepared cage was then placed inside the imaging unit, ensuring consistent positioning across observations. Behavioral tracking was performed using AnyMaze software (Stoelting Co.). An overhead mounted camera integrated within the imaging unit was used to capture video. Prior to each experiment, the appropriate AnyMaze protocol for mouse cage monitoring was loaded, and a new experiment file was created using a standardized naming convention including the study name, experimental day, date, and operator initials.

Animals were registered within the experiment file using unique animal identification numbers, identifiable by ear notches. The apparatus boundaries were defined within AnyMaze by manually adjusting the cage outline and hut region to match the visual field of the camera. A digital ruler tool within the software was used to confirm accurate scaling of the cage dimensions.

For each observation, a background image of the empty cage was captured before introducing the animal. A new background image was obtained whenever the cage or apparatus position was changed. Individual mice were then placed into the cage, and recording was initiated. Each observation consisted of a 30 second acclimation period, followed by 10 minutes of continuous automated tracking. During recording, care was taken to minimize external disturbances such as movement, shadows, or excessive noise, as these can interrupt tracking. If animals attempted to climb the cage walls, movement near the enclosure was minimized and corrected gently to prevent escape without direct handling.

During the first minute of each observation, tracking accuracy was visually inspected in real time by confirming that the software correctly labeled animal location and behavioral states (e.g., immobility, presence in hut). Observations with incorrect tracking (e.g., false detection of being "in hut") were stopped and either discarded or repeated following correction of the issue. Observations were allowed to run to completion without interruption. Successful completion was indicated by automatic termination of the test at the end of the recording period.

AnyMaze automatically quantified locomotor and activity related parameters throughout the recording period. Behavioral outputs included time spent mobile versus immobile, spatial location within the cage (including time spent in the hut), and general movement patterns. Behavioral definitions and tracking parameters were consistent across all animals within an experiment.

At the conclusion of testing, AnyMaze experiment files were saved for downstream analysis, and behavioral data were exported from the Results tab of AnyMaze as structured reports including animal IDs, observation numbers, and summary statistics.

4.2.2 Intramusuclar Injection of Engineered MSC Secretome

Following behavioral assessment using the AnyMaze tracking system, select cohorts of mice received intramuscular injections of conditioned culture media. Animals were anesthetized prior to injection to minimize discomfort and ensure consistent delivery. Each mouse received daily intramuscular injections of 50 µL of conditioned culture media for a period of one week. Injections were administered using sterile hypodermic needles suitable for small-animal applications, following established institutional animal care and use protocols. This dosing regimen was designed to evaluate the effects of the conditioned media on muscle and behavioral outcomes *in vivo*.

At designated endpoints, animals were euthanized using CO_2 inhalation, followed by cervical dislocation as a secondary method to ensure death, in accordance with humane euthanasia protocols. Tissue samples, including calf and thigh muscles, were harvested immediately post-mortem for histological analysis.

4.2.3 Isolation of Murine Skeletal Muscle Tissue

Following euthanasia, mice were briefly rinsed in 70% ethanol to reduce surface contaminants and facilitate sterile tissue handling. Bilateral thigh and calf muscles were carefully excised for histological analysis. In addition to skeletal muscle, other organs, including the heart, lungs, and kidneys, were also harvested and preserved for future studies.

Excised tissues were immediately rinsed in HBSS to remove residual blood and debris. Samples were then placed into labeled histology cassettes and submerged in 10% neutral buffered formalin (VWR, Cat. No. 89370-094) for fixation. Tissues were fixed for 48 hours at room temperature to ensure adequate penetration and preservation of cellular and extracellular matrix structures prior to paraffin embedding and sectioning. This fixation duration was selected to optimize tissue integrity and facilitate downstream histological staining and analysis.

4.3 Histology

4.3.1 Tissue Processing

Tissue processing was performed using a Tissue-Tek VIP® 6 AI automated processor (Sakura Finetek), following a standardized dehydration and clearing protocol. Samples underwent a graded ethanol series for dehydration, consisting of sequential immersions in 70%, 80%, 80%, 95%, 95%, 100%, 100%, and 100% ethanol, with each step lasting 90 minutes to ensure thorough removal of water content. This was followed by two xylene treatments, each for 90 minutes, to clear residual ethanol and prepare tissues for paraffin infiltration.

Subsequently, tissues were immersed in four consecutive paraffin baths, each lasting 30 minutes, to allow complete infiltration of paraffin wax. This extended paraffin exposure was implemented to enhance tissue preservation and ensure optimal embedding quality for downstream sectioning and histological analysis.

4.3.2 Tissue Embedding

Following tissue processing, paraffin-infiltrated tissue cassettes were transferred from the automated processor to the Leica EG1150 H embedding station for manual embedding. Embedding molds were pre-warmed in a heated bath to maintain the paraffin in a molten state at approximately $60°$C. Using a dispenser-operated nozzle, molten paraffin was dispensed into each mold to create a base layer.

Tissues were carefully transferred into the molds using heated forceps, allowing precise orientation to preserve anatomical structure for downstream histological analysis. The corresponding labeled tissue cassette was placed atop the mold, and additional molten paraffin was dispensed to fully encapsulate the tissue and ensure secure adhesion between the tissue and the cassette.

Once properly positioned, the modes were transferred to a cold plate maintained at approximately $10°$C, facilitating rapid solidification of the paraffin and stabilization of tissue orientation. After approximately 30 minutes, the solidified paraffin blocks were removed from the molds and stored at room temperature until ready for microtomy and slide preparation.

4.3.3 Tissue Sectioning

Paraffin-embedded tissue blocks were sectioned using a Leica RM2255 motorized rotary microtome. Each block was securely clamped into the universal cassette holder, and the specimen was carefully oriented to align the cutting plane. Section thickness was set to 10 µm, a standard thickness for histological analysis that balances structural integrity with staining clarity.

A disposable microtome blade was installed in the knife holder, and initial trimming was performed manually to expose the tissue surface and create a smooth cutting face. Once this tissue was exposed, serial sections were cut in continuous ribbons and gently transferred to a $40°$C warm water bath containing Photoflo (Kodak), a wetting agent that reduces surface tension and helps flatten the sections.

Flattened sections were then mounted onto positively charged glass microscope slides, with two sections placed per slide to allow for comparative staining and analysis. Slides were left to air dry overnight at room temperature to ensure proper adhesion of the tissue to the slide surface. Once dried, slides were either stored in slide boxes at room temperature, or processed further for histological staining procedures.

4.3.4 Masson's Trichrome Staining

Masson's Trichrome staining was performed to assess baseline collagen content in murine thigh and calf muscles from mice aged 20 to 24 weeks. Both wild-type DBA mice and dystrophin-deficient mdx mice were included in this analysis to compare normal and fibrotic muscle tissue characteristics.

Prepared slides from previously sectioned paraffin-embedded tissues were deparaffinized using a Leica Autostainer XL (ST5010; Leica Biosystems Nussloch GmbH). Slides were immersed in xyline for six minutes, followed by a descending ethanol series (100%, 100%, 95%, 70%) to rehydrate the tissue. Slides were then rinsed in distilled water for 5 minutes to complete the deparaffinization process.

Next, slides were incubated overnight at room temperature in Bouin's Fixative (Epredia, Cat. No. 22110621) to enhance staining intensity and tissue contrast. Following incubation, slides were rinsed in distilled water for five minutes to remove residual fixative.

For nuclear staining, slides were immersed in 600 mL of a 1:1 mixture of Weigert's Iron Hematoxylin Part A (Rankin Biomedical, Cat. No. N-6259A-16) and Part B (Ferric Chloride; Rankin Biomedical, Cat. No. N-6259B-16) for seven minutes, followed by a five-minute rinse in running distilled water. Cytoplasmic and muscle fibers were stained red using Biebrich Scarlet-Acid Fuchsin Stain (Cancer Diagnostics, Cat. No. SSC1052) for three minutes, then rinsed for three minutes in running distilled water. To differentiate collagen fibers, slides were immersed in Phosphomolybdic/Phosphotungstic Acid (Rankin Biomedical, Cat. No. N-6165-16) for 12 minutes, which selectively removes red dye from collagen. Slides were then transferred immediately to an Aniline Blue solution (Cancer Diagnostics, Cat. No. SSC1048) for four minutes to stain collagen fibers blue. Excess dye was removed with a three-minute rinse in distilled water, followed by a one-minute immersion in 1% glacial acetic acid (Fisher Chemical, Cat. No. A38500; Certified ACS grade, $\geq$ 99.7%) to enhance contrast. A final three-minute rinse in distilled water completed the staining process.

Slides were then dehydrated in the Leica Autostainer XL using a graded ethanol series (95%, 100%, 100%, 100%) for one minute each, followed by a two-minute immersion in xylene. Coverslipping was performed using an automatic coverslipper; in cases where manual coverslipping was required, Cytoseal™ Mounting Medium (Richard-Allan Scientific, Cat. No. 23244257) was used. Slides were allowed to dry overnight at room temperature before proceeding to microscopic imaging and analysis.

4.3.5 Immunohistochemistry (IHC) Staining

Immunohistochemistry (IHC) staining was performed to assess fibronectin content in murine thigh and calf muscles from mice aged 20 to 24 weeks. Both wild-type DBA mice and dystrophin-

deficient mdx mice were included in this analysis to compare normal and fibrotic muscle tissue characteristics.

Prepared slides from previously sectioned paraffin-embedded tissues were deparaffinized using a Leica Autostainer XL (ST5010; Leica Biosystems Nussloch GmbH). Slides were immersed in xylene for six minutes, followed by a descending ethanol series (100%, 100%, 95%, 70%) to rehydrate the tissue. Slides were then rinsed in distilled water for 5 minutes to complete the deparaffinization process.

Slides were immersed in phosphate buffered saline (PBS; Gibco™, Thermo Fisher Scientific, Cat. No. 10010023) to prevent dehydration while proceeding to the next step. Slides were taken one at a time from the PBS bath, and circles were drawn around each tissue sample on the slide using a PAP pen hydrophobic barrier liquid blocker (Newcomer Supply, Middleton, WI, USA; Part No. 6505). Circled tissue samples were then covered with 0.1% Triton™ X-100 (Thermo Scientific Chemicals, Thermo Fisher Scientific, Waltham, MA, USA; Cat. No. A16046.AE) for 10-15 minutes to encourage tissue permeability. Following this, slides were washed using HBSS three times. Slides were then covered in 5% horse serum (Omega Scientific, Tarzana, CA, USA; Cat. No. DH-07) for 1 hour to encourage the blocking of non-specific binding. After an hour, the primary antibody (rabbit IgG; Invitrogen™, Thermo Fisher Scientific, Waltham, MA, USA; Cat. No. PA5-29578) was diluted in HBSS to 1:500. One tissue sample of each sample was preserved with no primary antibody, to be used as a negative control, while the rest of the samples received the primary antibody dilution. Slides were then incubated overnight at $2 - 8^{\circ}$C.

After overnight incubation, slides were retrieved and kept in the dark for the remainder of the staining procedure. Slides were washed three times with Tween 0.1% (Ultra Pure; Thermo Scientific, Waltham, MA, USA; Cat. No. AAJ20605AP), and then covered with a secondary antibody (Goat anti-rabbit IgG (H+L) cross-adsorbed secondary antibody, Alexa Fluor™ 488 (polyclonal; Invitrogen™, Thermo Fisher Scientific, Waltham, MA, USA; Cat. No. A-11008), and left to incubate at room temperature for 2 hours. Following the two hour incubation period, the secondary antibody was removed and slides were washed three times with Tween 0.1%, followed by a single

HBSS wash. Slides were then covered in a 1:1000 DAPI (4',6-diamidino-2-phenylindole; Invitrogen™, Thermo Fisher Scientific, Waltham, MA, USA; Cat. No. D3571) to HBSS/Glycerol (ACS grade; Macron™, Avantor, Radnor, PA, USA; Cat. No. MK-5092-200) mixture for staining of the nuclei, followed by a glass coverslip. Slides were then immediately taken for imaging, with care to protect them from light exposure.

4.3.6 Imaging

Dried slides were imaged using the Olympus VS200 Slide Scanner, which allows high-resolution whole-slide imaging. Each slide was loaded into the scanner and imaged at 10 × magnification to capture collagen or fibronectin deposition across the tissue sections.

Quantitative image analysis was performed using Fiji (ImageJ 2.14.0/1.53t; Schindelin et al., 2012), an open-source image processing platform. The analysis focused on quantifying collagen or fibronectin content in each tissue section. For collagen detection, after calibrating spatial resolution (1 pixel = 0.548 μm), images were converted to RGB format. A blank 8-bit black image (collagenMask) was generated to store detected collagen pixels.

A custom macro (see Appendix C) iterated through each pixel, identifying tissue regions where the sum of RGB values is less than 700 (excluding white background and black voids). Collagen pixels were defined by a dominant blue channel using the condition:

- blue > red + 37 && blue > green + 37 && blue > 100

Detected collagen pixels were marked as white in the mask.

A duplicate of the original image (EditableOverlay) was created, and blue pixels (RGB: 0, 0, 255) were overlaid where collagen was detected. Manual editng was then performed to refine detection, removing artifacts such as edge effects and pooled dye regions that could falsely indicate collagen. After refinement, the macro recalculated tissue and and collagen pixel counts and computed collagen percentage, collagen area, and total tissue area. Results were exported to Excel, and a side-by-side comparison image was generated (see **Figure 4.1**), showing the original image alongside the edited overlay with collagen highlighted in blue.

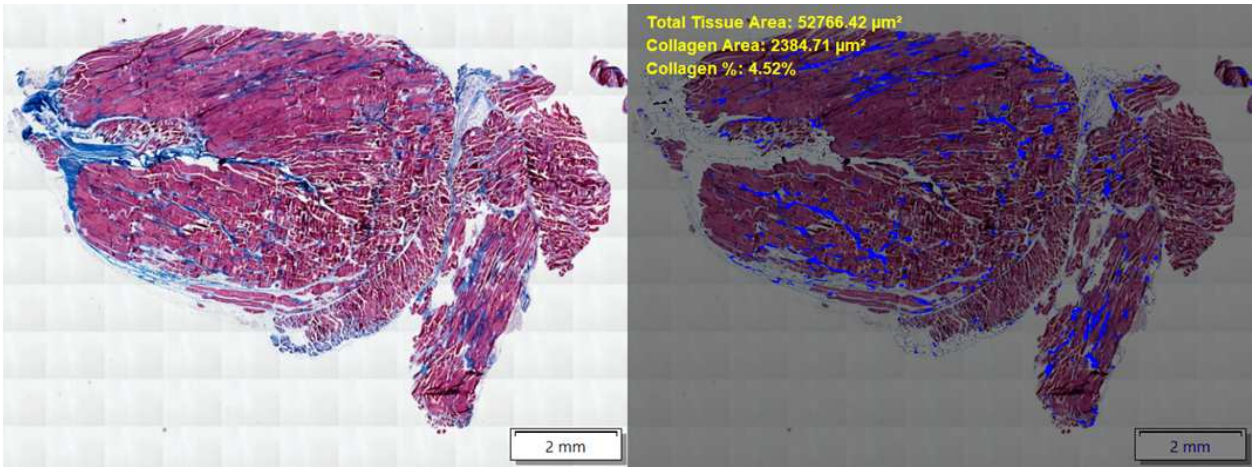

Figure 4.1: Example comparison image generated from ImageJ code for collagen content analysis. Image is of a 24-week mdx thigh, analyzed with a custom macro in Fiji (ImageJ).

For fibronectin quantitative image analysis, Fiji was also employed, but a different method had to be used to use it with fluorescence capturing. The fluorescence analysis focused on quantifying fibronectin content in each tissue section. After calibrating spatial resolution (1 pixel = 0.650 µm), the threshold for tissue identification was set (ranging 1 to 5), and any pixel that was not entirely black was turned white against a black background with the condition:

white = (255«16)+(255«8)+255; black = 0;

Image editing allowed for removal of non-tissue related pixels, such as the scale bar, to ensure accurate tissue area count (tissueMask).

Following acceptance of the tissue mask, the threshold for green identification within the sample was determined by trial and error, with a range of 40-60 for the minGreen (raw brightness cutoff) and 20-30 for the minExcess (green hue stronger than others). The user is able to change threshold values repeatedly until satisfied with the amount of green being shown. Following this, areas of green that may not be true fibronectin detection, such as areas of dye pooling or trapped dye, can be removed.

The custom macro (see Appendix D) iterated through each pixel, identifying fibronectin (green) pixels defined by a dominant green channel using the condition:

Figure 4.2: Example comparison image generated from ImageJ code for fibronectin content analysis. Image is of a 24-week untreated mdx thigh, analyzed with a custom macro in Fiji (ImageJ).

(g2>200 && r2<50 && b2<50)

Detected pixels were marked as green in the mask.

A duplicate of the original image (EditableOverlay) was created, and green pixels were overlaid where fibronectin was detected. After refinement, the macro recalculated tissue and fibronectin pixel counts and computed fibronectin percentage, area, and total tissue area, as well as a log of the threshold values used for each image. Results were exported to Excel, and comparison images were generated (see **Figure 4.2**), showing the original image alongside the tissue overlay, and the edited overlay with fibronectin highlighted in green.

4.4 AnyMaze Results

In this study, a total of 16 female mice aged 20–24 weeks were evaluated. Animals were divided into four groups (n = 4 per group): wild-type DBA mice without injection, wild-type DBA mice receiving injection, dystrophin-deficient (mdx) mice without injection, and dystrophin-deficient (mdx) mice receiving injection. Mice in the treatment groups received intramuscular injections into the left thigh consisting of plain culture media, and an injection with conditioned culture media (CCM) on their right thigh. The CCM was derived from the culture environment surrounding bulk-encapsulated mesenchymal stem cells (MSCs), as described in Chapter 2.

Behavioral data were collected using the AnyMaze tracking system across an eight-day period, consisting of one baseline measurement followed by seven consecutive days of monitoring. The

software quantified multiple locomotor parameters, including mean and maximum velocity, total distance traveled, and freezing duration. For the purposes of this analysis, distance traveled and anti-clockwise turning behavior were selected due to their relevance and sensitivity to observed differences between groups. All measurements were normalized to each animal's Day 1 baseline to account for inter-individual variability.

4.4.1 Distance Traveled

Locomotor activity, as assessed by total distance traveled, was evaluated over seven consecutive testing days in both DBA and mdx mice, with and without treatment (**Figure 4.3A**). Wild-type DBA mice exhibited relatively low and stable levels of locomotion throughout the study period (blue and red). Importantly, administration of injections did not produce a substantial deviation from this baseline pattern (red), indicating that treatment had minimal impact on locomotor output in healthy animals.

In contrast, mdx mice (green and purple) demonstrated consistently elevated locomotor activity relative to DBA controls. This increase is consistent with previously described behavioral phenotypes associated with dystrophin deficiency, including altered muscle function and compensatory movement patterns. Among mdx mice, treatment appeared to modulate activity in a distinct manner. Treated mdx mice (green) displayed notably higher and more variable locomotor activity, particularly during the early testing days, suggesting a transient enhancement or dysregulation of movement. In comparison, untreated mdx mice (purple) exhibited more constrained and comparatively stable activity levels over time.

Across all experimental groups, a gradual decline in activity was observed over repeated testing days. This trend may reflect habituation to the testing environment or reduced exploratory drive with repeated exposure. Notably, however, treated mdx mice maintained greater variability despite this overall downward trend, which may indicate underlying changes in neuromuscular function or behavioral responsiveness.

4.4.2 Anti-Clockwise Turning Behavior

Anti-clockwise turning behavior was also quantified to assess directional bias, motor coordination, and potential asymmetries in movement (**Figure 4.3B**). This parameter is less intuitive than gross locomotion but provides insight into lateralized motor function and stereotyped movement patterns. Increased anti-clockwise turning is generally indicative of leftward turning bias, which may arise from asymmetries in muscle strength, coordination, or neural control.

Wild-type DBA mice (blue and red) exhibited low to moderate levels of turning behavior with modest variability across days. Similar to the distance traveled results, treatment (red) did not significantly alter turning patterns in this group, suggesting preserved motor symmetry and coordination in healthy animals regardless of injection.

In contrast, mdx mice (green and purple) displayed a marked increase in anti-clockwise turning behavior compared to DBA controls. This finding is consistent with impaired motor coordination and potential asymmetrical muscle function associated with dystrophin deficiency. Within the mdx cohort, treated animals (green) showed particularly elevated and more variable turning behavior across the testing period. Untreated mdx mice (purple), while still showing increased turning relative to DBA mice, exhibited more constrained and consistent values.

The enhanced turning bias observed in treated mdx mice may reflect treatment-induced modulation of limb function. Given that CCM injections were administered unilaterally to the right hindlimb, these findings suggest that localized changes in muscle strength, stiffness, or coordination could contribute to altered movement symmetry. This asymmetry may manifest behaviorally as increased directional turning, particularly during exploratory activity.

Overall, these results demonstrate clear strain-dependent differences in both locomotor activity and turning behavior, with mdx mice exhibiting greater movement variability and asymmetry compared to wild-type controls. Furthermore, treatment with CCM appears to selectively influence behavioral outputs in mdx mice, potentially enhancing or altering neuromuscular function in a manner that is not observed in healthy animals.

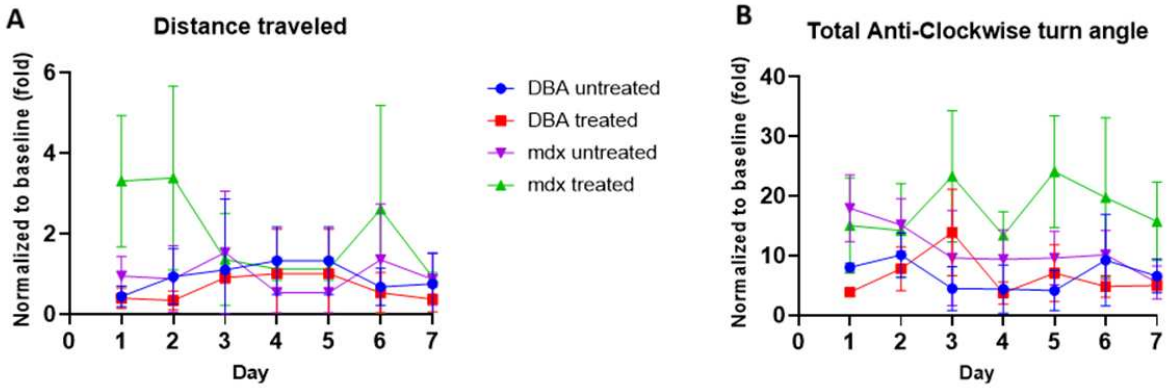

Figure 4.3: AnyMaze Results of sixteen 20 -24 week female mice divided into four groups (n = 4 per group): wild-type DBA mice without injection, wild-type DBA mice receiving injection, dystrophin-deficient (mdx) mice without injection, and dystrophin-deficient (mdx) mice receiving injection. **(A)** Distance traveled. Wild-type DBA mice exhibited low and stable levels of locomotion, mdx mice demonstrated consistently elevated locomotor activity relative to DBA controls. Treated mdx mice displayed notably higher and more variable locomotor activity, while untreated mdx mice exhibited more stable activity levels. **(B)** Anti-clockwise turning behavior. DBA mice exhibited low to moderate levels of turning behavior with modest variability. mdx mice displayed a marked increase in anti-clockwise turning behavior, and treated animals showed particularly elevated and more variable turning behavior across the testing period. Untreated mdx mice exhibited more constrained and consistent values compared to treated mdx mice.

To determine whether these behavioral differences are associated with underlying structural or cellular changes, subsequent histological analyses were performed.

4.5 Fibronectin Deposition After Engineered MSC Treatment

To evaluate fibronectin deposition, histological samples were obtained from the same cohort of 16 treated and untreated DBA and dystrophin-deficient (mdx) mice. Muscle sections were stained using immunohistochemistry (IHC) to detect fibronectin and imaged under consistent acquisition settings. Images were analyzed using a custom ImageJ macro, which enabled standardized thresholding and included steps to remove background signal and false-positive detection. Fibronectin-positive regions were identified based on green fluorescence intensity, and the proportion of positive staining was calculated relative to total tissue area, yielding a percentage-based measure of fibronectin content.

The resulting quantification from all samples was then compiled and visualized graphically to assess differences in fibronectin deposition between treated and untreated wild-type and dystrophin-

deficient mice. Statistical analyses were performed to determine the presence of significant differences between groups.

4.5.1 Baseline Comparison: mdx vs. DBA

Before evaluating treatment effects, we first characterized baseline differences in fibronectin deposition between dystrophin-deficient (mdx) and wild-type (DBA) mice. Both thigh and calf muscles were analyzed to determine whether fibrotic pathology varied between muscle groups. A two-way ANOVA revealed significant effects of genotype ($F(1,12) = 26.15$, $p = 0.0003$) and muscle group ($F(1,12) = 99.52$, $p < 0.0001$), as well as a significant interaction between genotype and muscle ($F(1,12) = 17.87$, $p = 0.0012$), indicating that the extent of fibrosis depends on both disease state and muscle type.

Post hoc analysis confirmed that mdx mice exhibited significantly higher fibronectin content than DBA controls in both muscles. This difference was present in the thigh ($p = 0.0074$) and was even more pronounced in the calf ($p < 0.0001$). Additionally, fibronectin levels in mdx mice were significantly higher in the calf compared to the thigh ($p = 0.0001$), whereas no difference was observed between muscles in DBA mice ($p = 0.9214$).

Together, these results as shown in **Figure 4.4A** establish a clear disease baseline, with mdx mice exhibiting elevated fibronectin deposition and the calf muscle representing a more severely affected region. The presence of a significant interaction further supports analyzing thigh and calf muscles separately when assessing treatment effects.

4.5.2 Treatment Effects in Thigh Muscle

Given the baseline differences we observed, we next examined treatment effects specifically in the thigh muscle (**Figure 4.4B**), which was also the site of intramuscular injection.

A one-way ANOVA revealed a significant effect of treatment condition on fibronectin content ($F(5,18) = 11.04$, $p < 0.0001$). Variance testing indicated no significant differences between groups (Brown–Forsythe $p = 0.0790$; Bartlett's $p = 0.1314$), supporting the validity of the analysis. Tukey's multiple comparisons test was used for post hoc evaluation.

In mdx mice, conditioned media (CCM; M) produced a significant improvement relative to both untreated (U) and regular culture media (CM; C) controls, with fibronectin levels significantly reduced compared to mdx untreated ($p = 0.0007$) and mdx CM ($p = 0.0033$). In contrast, no significant difference was observed between mdx untreated and mdx CM groups ($p = 0.9739$), indicating that standard culture media alone does not significantly impact fibronectin deposition. Notably, fibronectin levels in mdx mice treated with CCM were no longer significantly different from DBA controls ($p > 0.9999$), suggesting that treatment restores fibronectin content to near baseline levels.

In contrast, DBA thigh muscle did not exhibit a detectable treatment response. No significant differences were observed between DBA untreated (U), CM (C), and CCM (M) groups (all $p > 0.8$), indicating that fibronectin levels remain low and stable in healthy muscle regardless of treatment. Overall, the effect in thigh muscle was present but modest, consistent with the lower baseline disease severity observed in this muscle compared to the calf. While we observed a measurable treatment response in the thigh, the magnitude of change was limited relative to more severely affected tissue.

While we observed a measurable treatment response in thigh muscle, baseline data indicated that the calf muscle was more severely affected in mdx mice. We therefore next focused on the calf muscle to determine whether disease severity influences responsiveness to conditioned media, and whether treatment effects extend beyond the immediate injection site to impact distal muscle regions.

4.5.3 Treatment Effects in Calf Muscle

Although the thigh was the injection site, our baseline analysis showed that calf muscle was more severely affected in mdx mice. We therefore examined treatment effects in the calf muscle to determine whether increased disease severity influences responsiveness to conditioned media, and whether treatment effects extend beyond the immediate injection site (**Figure 4.4C**).

A one-way ANOVA revealed a significant effect of treatment condition on fibronectin content in calf muscle ($F(5,18) = 9.574$, $p = 0.0001$). Assumptions of equal variance were satisfied, as indicated by non-significant Brown–Forsythe ($p = 0.9660$) and Bartlett's ($p = 0.9767$) tests. Tukey's multiple comparisons test was therefore used for post hoc analysis.

Consistent with baseline findings, mdx untreated (U) mice exhibited significantly elevated fibronectin levels compared to DBA controls (DBA untreated vs. mdx untreated, $p = 0.0001$), confirming the presence of more severe fibrotic pathology in the calf muscle.

When we examined treatment effects in mdx mice, conditioned media produced a robust improvement. Fibronectin levels were significantly reduced in the mdx CCM (M) group compared to mdx untreated (U) animals ($p = 0.0007$), indicating a strong anti-fibrotic effect. In contrast, culture media (CM; C) alone produced only a partial effect, with mdx CM showing a modest reduction relative to mdx untreated ($p = 0.0371$), but remaining elevated overall. Importantly, the difference between mdx CM and mdx CCM was not statistically significant ($p = 0.4400$), suggesting variability in response or a less consistent effect of CM treatment.

Notably, fibronectin levels in mdx mice treated with CCM were no longer significantly different from DBA groups (e.g., DBA untreated vs. mdx CCM, $p = 0.9530$), indicating substantial normalization of ECM composition in this more severely affected muscle. In contrast, DBA mice again did not exhibit a detectable treatment response. No significant differences were observed between DBA untreated, CM, and CCM groups (all $p > 0.7$), consistent with the stable, low fibronectin levels observed in healthy tissue.

Overall, conditioned media produced a stronger effect in the calf muscle compared to the thigh and is shown in **Figure 4.4C**, consistent with the higher baseline disease severity in this region. This suggests that treatment efficacy may be influenced by the extent of pre-existing fibrosis. Furthermore, the presence of a treatment effect in the calf, despite it not being the injection site, indicates that conditioned media effects are not strictly localized, but instead reflect broader tissue-level remodeling.

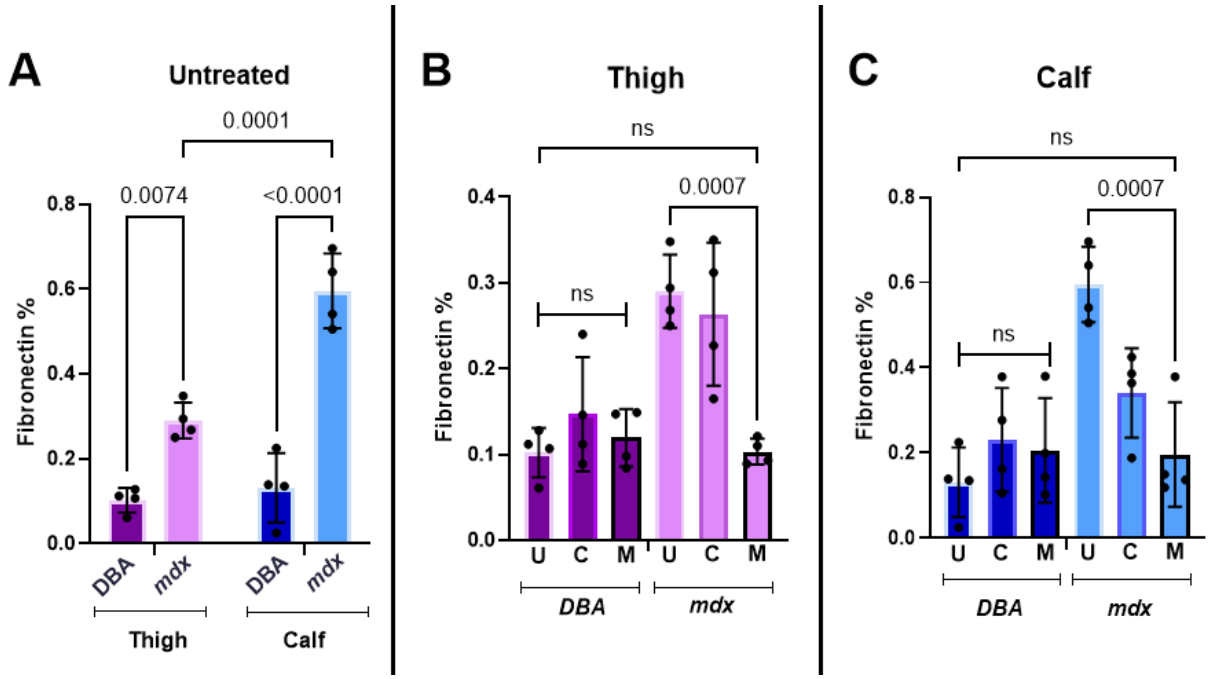

Figure 4.4: Quantification of fibronectin deposition in thigh and calf muscles across DBA and mdx mice following treatment. **(A)** mdx mice showed significantly elevated fibronectin compared to DBA controls at baseline, with greater severity in calf muscle. **(B)** In the thigh, conditioned culture media (M) significantly reduced fibronectin levels in mdx mice relative to untreated (U) and culture media (C) groups, resulting in values comparable to DBA controls, while CM alone had no significant effect. **(C)** In the calf, CCM produced a more pronounced reduction in fibronectin, consistent with increased baseline disease severity, whereas CM showed only partial or variable effects. No significant treatment effects were observed in DBA mice. Data are normalized to baseline and presented as mean ± [SEM/SD]; significance determined by one- or two-way ANOVA with Tukey's multiple comparisons test

Fibronectin is an early ECM component associated with tissue remodeling and, as discussed previously, often precedes and organizes collagen fibrillogenesis. To determine whether the conditioned media effects extend beyond early ECM changes, we next examined collagen deposition.

4.6 Collagen Deposition After Engineered MSC Treatment

Collagen content provides insight into fibrotic remodeling and long-term tissue architecture, representing a later stage of extracellular matrix (ECM) deposition compared to fibronectin. To determine whether the effects observed in fibronectin extend to more mature fibrotic outcomes, collagen content was quantified *in vivo* using the same cohort of treated and untreated DBA and dystrophin-deficient (mdx) mice.

Muscle sections from both thigh and calf were stained using Masson's trichrome, in which collagen is visualized in blue. Slides were imaged under consistent acquisition settings and analyzed using a custom ImageJ macro, optimized for collagen detection. This macro enabled standardized thresholding and included steps to remove background signal and false-positive detection.

The resulting quantification was expressed as the percentage of collagen-positive area relative to total tissue area. These values were compiled across all groups and visualized graphically to assess differences in collagen deposition between treated and untreated wild-type and dystrophin-deficient mice. Statistical analyses were performed to determine the presence of significant differences between groups.

4.6.1 Baseline Comparison: mdx vs. DBA

We first examined baseline collagen deposition as a readout of fibrotic extracellular matrix remodeling. A two-way ANOVA revealed a significant main effect of genotype ($F(1,12) = 41.75$, $p < 0.0001$) and a significant interaction between genotype and muscle group ($F(1,12) = 4.890$, $p = 0.0472$), while the main effect of muscle group alone was not statistically significant ($F(1,12) = 4.386$, $p = 0.0581$). These results indicate that collagen deposition is strongly driven by disease status, with muscle-specific differences emerging in the context of dystrophy.

As expected, mdx muscle exhibited substantially higher collagen levels than DBA controls, confirming pronounced baseline fibrosis. Post hoc analysis further demonstrated that this increase was significant in both muscle groups. In the thigh, mdx mice showed significantly elevated collagen compared to DBA controls ($p = 0.0003$), and a similar difference was observed in the calf ($p = 0.0469$).

Importantly, a muscle-dependent effect was observed within mdx mice. Collagen deposition in mdx thigh muscle was significantly higher than in mdx calf muscle ($p = 0.0439$), indicating regional variation in fibrotic severity. In contrast, DBA muscles remained uniformly low, with no significant difference between thigh and calf ($p = 0.9998$).

Additional comparisons supported this pattern, with mdx thigh muscle exhibiting significantly higher collagen levels than DBA calf muscle ($p = 0.0003$), further highlighting the magnitude of dystrophic remodeling.

Together, these findings shown in **Figure 4.5A** demonstrate that baseline fibrotic burden is strongly disease-dependent and exhibits muscle-specific variation in mdx mice. While overall differences between muscle groups were modest at the main-effect level, the significant interaction underscores that muscle type influences collagen deposition specifically in the presence of disease.

Given these muscle-specific differences in baseline fibrosis, we next asked whether conditioned media alters collagen deposition differently across muscles.

4.6.2 Treatment Effects in Thigh Muscle

With the elevated baseline collagen deposition observed in mdx thigh muscle, we next assessed whether treatment could modulate fibrotic remodeling at this site.

A one-way ANOVA revealed a significant effect of treatment condition on collagen content ($F(5,18) = 21.66$, $p < 0.0001$). While the Brown–Forsythe test was not significant ($p = 0.2464$), Bartlett's test indicated unequal variances ($p < 0.0001$), suggesting some heterogeneity across groups. Despite this, the overall ANOVA remained highly significant, and Tukey's multiple comparisons test was used for post hoc evaluation.

Consistent with baseline findings, mdx mice exhibited significantly elevated collagen deposition compared to DBA controls across all conditions (all $p \leq 0.0327$), confirming persistent fibrotic remodeling in dystrophic muscle.

When examining treatment effects within mdx mice, conditioned culture media (CCM; M) produced a reduction in collagen deposition relative to culture media (CM; C) ($p = 0.0117$). However, CCM did not significantly reduce collagen compared to untreated mdx muscle ($p = 0.1570$), and CM alone also did not differ significantly from untreated mdx ($p = 0.7690$). These findings indicate that while CCM provides some improvement relative to CM, it does not fully reverse collagen accumulation in dystrophic thigh muscle.

Importantly, collagen levels in mdx CCM-treated mice remained significantly higher than DBA controls (all $p \leq 0.0327$), further supporting that treatment does not restore collagen deposition to baseline levels in this muscle.

In contrast, DBA thigh muscle remained low in collagen across all treatment conditions (U, C, M), with no significant differences observed between groups (all $p > 0.9999$), confirming that treatment does not alter ECM composition in healthy tissue.

Overall, these results illustrated in **Figure 4.5B** suggest that conditioned media partially attenuates fibrotic remodeling in dystrophic thigh muscle, rather than fully normalizing collagen deposition. Compared to the fibronectin findings, where CCM restored levels to those of DBA controls, the more limited effect observed here is consistent with collagen representing a later stage of fibrosis that may be less readily reversible. We anticipate that these trends may become more robust with increased sample size in future studies.

In contrast to fibronectin, baseline collagen deposition was higher in mdx thigh than in calf muscle. We therefore next focused on the calf muscle to assess whether collagen remodeling is similarly responsive to treatment in a less fibrotic tissue environment, and to evaluate potential non-local effects of conditioned media.

4.6.3 Treatment Effects in Calf Muscle

In contrast to thigh muscle, collagen deposition in calf muscle appeared to be driven primarily by disease status rather than treatment. A one-way ANOVA revealed a significant effect of treatment condition ($F(5,18) = 6.020$, $p = 0.0019$). However, tests for equal variance were significant (Brown–Forsythe $p < 0.0001$; Bartlett's $p < 0.0001$), indicating substantial variability across groups, which should be considered when interpreting post hoc comparisons.

Consistent with baseline findings, mdx mice exhibited elevated collagen levels compared to DBA controls. Post hoc analysis indicated that this difference reached significance in some comparisons (e.g., DBA untreated vs. mdx CM, $p = 0.0263$), while others approached but did not reach

significance (e.g., DBA untreated vs. mdx untreated, p = 0.0930; DBA untreated vs. mdx CCM, p = 0.0516), reflecting variability within the dataset.

When examining treatment effects within mdx mice, no significant differences were observed between untreated (U), CM-treated (C), and CCM-treated groups (M) (all $p > 0.98$). This indicates that neither conditioned media nor culture media significantly altered collagen deposition in calf muscle. In contrast, DBA mice remained uniformly low in collagen across all treatment conditions (U, C, M), with no significant differences observed (all $p > 0.9999$), consistent with the stable ECM profile of healthy tissue.

Overall, these findings illustrated in **Figure 4.5C** suggest that fibrotic remodeling in calf muscle is less responsive to treatment compared to the thigh. Despite evidence of elevated collagen in mdx mice, conditioned media did not significantly reduce collagen levels relative to untreated or culture media-treated groups. This may reflect differences in matrix maturity, turnover dynamics, or therapeutic accessibility within the calf muscle microenvironment.

Together, these data indicate that collagen remodeling exhibits muscle-dependent treatment sensitivity, with partial modulation observed in thigh muscle but a more treatment-resistant fibrotic profile in calf muscle.

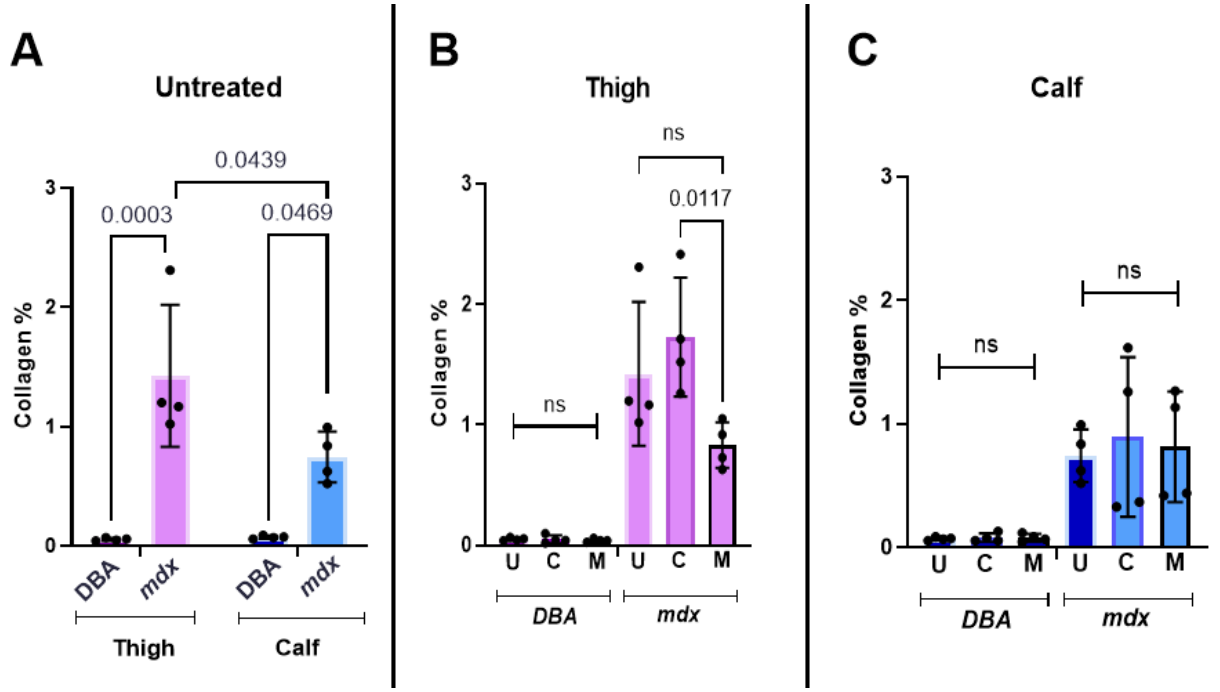

Figure 4.5: Collagen deposition in thigh and calf muscles of DBA and mdx mice with and without treatment. **(A)** At baseline, mdx mice exhibited significantly higher collagen content compared to DBA controls, with a muscle-dependent pattern in which thigh muscle showed greater collagen accumulation than calf. **(B)** In thigh muscle, conditioned culture media (M) partially reduced collagen deposition relative to culture media (C), but did not significantly differ from untreated (U) mdx, indicating incomplete reversal of fibrosis. **(C)** In calf muscle, collagen levels were primarily driven by disease status, with no significant differences observed between treatment conditions in mdx mice. DBA mice remained low in collagen across all groups. Data represent mean ± [SEM/SD]; statistical significance determined by ANOVA with Tukey's post hoc test ($p < 0.05$).

4.7 Discussion

In this study, a total of 16 female mice aged 20–24 weeks were evaluated and divided into four groups (n = 4 per group): wild-type DBA mice without injection, wild-type DBA mice receiving injection, dystrophin-deficient (mdx) mice without injection, and dystrophin-deficient (mdx) mice receiving injection. Mice in the treatment groups received intramuscular injections into the left thigh consisting of culture media, as well as conditioned culture media (CCM) in the contralateral thigh. The CCM was derived from the culture environment surrounding bulk-encapsulated mesenchymal stem cells (MSCs), as described in Chapter 2.

Behavioral data were collected using the AnyMaze tracking system to assess locomotor activity, including distance traveled and anti-clockwise turning behavior. Wild-type DBA mice exhibited low and stable levels of locomotion throughout the testing period, whereas mdx mice demonstrated consistently elevated locomotor activity relative to DBA controls. Treated mdx mice displayed higher and more variable activity levels, particularly during early testing days, while untreated mdx mice exhibited more stable locomotion.

These findings suggest that conditioned media influences movement behavior, indicating a biological effect on neuromuscular function. However, the increased activity and variability observed in treated mdx mice likely reflect a combination of altered muscle function, compensation, or adaptation over time, rather than a direct measure of improved muscle performance. The early increase in activity may represent an initial response to treatment, while the variability across animals suggests heterogeneous effects. As such, behavioral changes should be interpreted cautiously and in conjunction with histological outcomes to better assess therapeutic impact.

Analysis of turning behavior revealed a similar trend. DBA mice showed low to moderate turning behavior with limited variability, while mdx mice exhibited increased anti-clockwise turning, indicative of altered coordination or asymmetry in movement. Treated mdx mice displayed greater variability and elevated turning behavior compared to untreated mdx mice, suggesting that treatment may influence movement patterns, potentially through localized changes in muscle function.

However, several limitations are associated with the AnyMaze behavioral analysis. Behavioral outputs such as distance traveled and turning behavior provide quantitative measures of locomotion, but do not directly explain the underlying biological mechanisms[1,2]. Observed changes may reflect a combination of muscle function, compensatory movement strategies, or behavioral factors such as stress or habituation[2,3,4]. Additionally, behavioral data are sensitive to experimental conditions including lighting, handling, and time of day, although efforts were made to standardize these variables[5,6,7].

DBA mice are known to display distinct behavioral phenotypes, including heightened stress responsiveness and increased excitability, which can contribute to variability in experimental out-

comes and make repeated handling more difficult, particularly under conditions of repeated testing or environmental change[8,9]. Furthermore, the relatively small sample size increases variability across groups. Importantly, AnyMaze captures whole-animal movement and cannot resolve limb-specific contributions, which is a key limitation given the localized nature of the intramuscular injections. For this reason, histological analyses were included to provide tissue-level insight into the observed behavioral changes.

Histological analysis of fibronectin and collagen deposition aligned with the established pathology of Duchenne muscular dystrophy (DMD), in which the absence of dystrophin leads to progressive degeneration and fibrosis[10,11,12]. Statistical analyses were performed using one-way or two-way ANOVA depending on the experimental design, followed by Tukey's post-hoc tests when appropriate. These analyses demonstrated that genotype exerted a dominant effect on both fibronectin and collagen deposition, consistent with the fibrotic progression observed in dystrophin-deficient muscle[10,11,13].

Baseline fibronectin analysis revealed significantly elevated deposition in mdx mice compared to DBA controls, with the calf muscle representing a more severely affected region. The presence of a significant interaction between genotype and muscle group supports the importance of evaluating muscle types independently. Treatment with conditioned media resulted in a measurable reduction in fibronectin in mdx mice, with a modest effect observed in the thigh and a more pronounced response in the calf. Notably, this effect was observed even in the non-injected calf muscle, suggesting that conditioned media may exert broader tissue-level effects rather than acting solely at the injection site. These findings indicate that treatment efficacy may be influenced by baseline disease severity, with more fibrotic tissue exhibiting greater responsiveness.

Fibronectin serves as an early marker of extracellular matrix remodeling and plays a key role in organizing collagen deposition[14,15,16,17]. To determine whether the effects of conditioned media extend to later stages of fibrosis, collagen deposition was evaluated. Baseline collagen analysis confirmed elevated fibrotic burden in mdx mice, with a significant dependence on both disease status and muscle type.

In the thigh muscle, conditioned media partially attenuated collagen deposition. While collagen levels were reduced relative to culture media-treated groups, they remained elevated compared to DBA controls and were not significantly different from untreated mdx mice. This contrasts with the fibronectin results, in which conditioned media restored levels to those of healthy controls. These findings suggest that while conditioned media effectively modulates early ECM remodeling, it has a more limited impact on established fibrosis, consistent with collagen representing a later and more stable stage of matrix deposition.

In contrast, collagen remodeling in the calf muscle was largely unresponsive to treatment. Although mdx mice exhibited elevated collagen levels relative to DBA controls, no significant differences were observed between untreated, culture media-treated, and conditioned media-treated mdx groups. This suggests that fibrotic remodeling in the calf may be more resistant to therapeutic intervention, potentially due to differences in matrix maturity, turnover dynamics, or tissue accessibility[11,13].

Several limitations are associated with the histological analyses performed in this study. Both IHC and Masson's trichrome staining are semi-quantitative techniques, and results may be influenced by staining variability or differences in image acquisition[18,19,20,21]. Although custom ImageJ macros were used to standardize quantification and remove false positives, the analysis remains dependent on thresholding parameters, introducing some degree of user bias. Additionally, histological assessment represents two-dimensional sections of inherently heterogeneous three-dimensional tissue, which may not fully capture regional variability in fibrosis[22,23,24]. The relatively small sample size further contributes to variability in the dataset. Finally, while fibronectin and collagen provide valuable markers of ECM remodeling, these measures do not directly reflect functional properties such as tissue stiffness or contractility.

Importantly, the limitations of histological and behavioral analyses are complementary. Histology provides detailed insight into tissue-level changes but lacks functional resolution, whereas behavioral analysis captures functional outcomes but lacks mechanistic specificity. Together, these approaches provide a more comprehensive understanding of treatment effects.

Overall, these findings demonstrate that MMP-enriched conditioned media derived from hydrogel-encapsulated MSCs can modulate fibrotic remodeling in dystrophic muscle, with pronounced effects on early ECM components such as fibronectin and more limited effects on established collagen deposition. The therapeutic response appears to be both muscle-dependent and influenced by baseline disease severity. These results support the potential of MSC-derived conditioned media as a strategy to attenuate fibrosis in DMD, while also highlighting the need for further investigation into optimizing treatment efficacy and understanding the mechanisms underlying ECM remodeling.

References

[1] Mark G. Bowden et al. “Advancing Measurement of Locomotor Rehabilitation Outcomes to Optimize Interventions and Differentiate between Recovery versus Compensation”. In: *Journal of Neurologic Physical Therapy* 36.1 (2012), pp. 38–44. DOI: 10.1097/NPT.0b013e3182472cf6.

[2] Michael L. Seibenhener and Michael C. Wooten. “Use of the Open Field Maze to Measure Locomotor and Anxiety-like Behavior in Mice”. In: *Journal of Visualized Experiments* 96 (2015), e52434. DOI: 10.3791/52434.

[3] Melissa M. Haulcomb et al. “Locomotor Analysis Identifies Early Compensatory Changes During Disease Progression and Subgroup Classification in a Mouse Model of Amyotrophic Lateral Sclerosis”. In: *Neural Regeneration Research* 12.10 (2017), pp. 1664–1679. DOI: 10.4103/1673-5374.217346.

[4] Levente Gellert and Dániel Varga. “Locomotion Activity Measurement in an Open Field for Mice”. In: *Bio-Protocol* 6.13 (2016), e1857. DOI: 10.21769/BioProtoc.1857.

[5] Christiana K. Miller et al. “Interactions of the Estrous Cycle, Novelty, and Light on Female and Male Rat Open Field Locomotor and Anxiety-Related Behaviors”. In: *Physiology & Behavior* 228 (2020), p. 113203. DOI: 10.1016/j.physbeh.2020.113203.

[6] J. Adriaan Bouwknecht et al. “Differential Effects of Exposure to Low-Light or High-Light Open-Field on Anxiety-Related Behaviors; Relationship to c-Fos Expression in Serotonergic and Non-Serotonergic Neurons in the Dorsal Raphe Nucleus”. In: *Brain Research Bulletin* 72.1 (2007), pp. 32–43. DOI: 10.1016/j.brainresbull.2006.12.009.

[7] Christian G. Schwarz et al. “Influence of Diurnal Phase on Behavioral Tests of Sensorimotor Performance, Anxiety, Learning and Memory in Mice”. In: *Scientific Reports* 12 (2022), p. 310. DOI: 10.1038/s41598-021-03155-5.

[8] Michaela D. Filiou et al. “Behavioral and Metabolome Differences between C57BL/6 and DBA/2 Mouse Strains: Implications for Their Use as Models for Depression- and Anxiety-Like Phenotypes”. In: *Metabolites* 11.2 (2021), p. 128. DOI: 10.3390/metabo11020128. URL: https://www.ncbi.nlm.nih.gov/pmc/articles/PMC7926853/.

[9] B. Siegfried et al. “Effects of isolation on activity, reactivity, excitability and aggressive behavior in two inbred strains of mice”. In: *Behavioural Brain Research* 2.2 (1981), pp. 211–218. DOI: 10.1016/0166-4328(81)90056-5.

[10] Nicolas Dubuisson et al. “Histological Methods to Assess Skeletal Muscle Degeneration and Regeneration in Duchenne Muscular Dystrophy”. In: *International Journal of Molecular Sciences* 23.24 (2022), p. 16080. DOI: 10.3390/ijms232416080.

[11] Addeli Bez Batti Angulski et al. “Duchenne Muscular Dystrophy: Disease Mechanism and Therapeutic Strategies”. In: *Frontiers in Physiology* 14 (2023), p. 1183101. DOI: 10.3389/fphys.2023.1183101.

[12] Ridhi Sahani et al. “Diaphragm Muscle Fibrosis Involves Changes in Collagen Organization with Mechanical Implications in Duchenne Muscular Dystrophy”. In: *Journal of Applied Physiology* 132.3 (2022), pp. 653–672. DOI: 10.1152/japplphysiol.00248.2021.

[13] Yassine Kharraz et al. “Understanding the Process of Fibrosis in Duchenne Muscular Dystrophy”. In: *BioMed Research International* 2014 (2014), p. 965631. DOI: 10.1155/2014/965631.

[14] T. Velling et al. “Polymerization of Type I and III Collagens Is Dependent On Fibronectin and Enhanced By Integrins $\alpha 11\beta 1$and $\alpha 2\beta 1$*”. In: *Journal of Biological Chemistry* 277.40 (2002), pp. 37377–37381. DOI: 10.1074/jbc.M206286200. URL: https://doi.org/10.1074/jbc.M206286200.

[15] “Collagen I matrix turnover is regulated by fibronectin polymerization”. In: *American Journal of Physiology - Cell Physiology* 297.5 (2009). DOI: 10.1152/ajpcell.00341.2009. URL: https://doi.org/10.1152/ajpcell.00341.2009.

[16] J. Sottile and D. C. Hocking. “Fibronectin Polymerization Regulates the Composition and Stability of Extracellular Matrix Fibrils and Cell-Matrix Adhesions”. In: *Molecular Biology of the Cell* 13.10 (2002), pp. 3546–3559. DOI: 10.1091/mbc.E02-01-0048. URL: https://doi.org/10.1091/mbc.E02-01-0048.

[17] “Role of fibronectin in collagen deposition: Fab’ to the gelatin-binding domain of fibronectin inhibits both fibronectin and collagen organization in fibroblast extracellular matrix”. In: *The Journal of Cell Biology* 92.2 (1982), pp. 485–492. DOI: 10.1083/jcb.92.2.485. URL: https://doi.org/10.1083/jcb.92.2.485.

[18] Alexandra R. Crowe and Wei Yue. “Semi-quantitative Determination of Protein Expression Using Immunohistochemistry Staining and Analysis: An Integrated Protocol”. In: *Bio-Protocol* 9.24 (2019), e3465. DOI: 10.21769/BioProtoc.3465.

[19] Alexandra R. Crowe and Wei Yue. “Updated: Semi-quantitative Determination of Protein Expression Using Immunohistochemistry Staining and Analysis”. In: *Bio-Protocol* 13.2 (2023), e4610. DOI: 10.21769/BioProtoc.4610.

[20] Emily C. Stack et al. “Principles and Approaches for Reproducible Scoring of Tissue Stains in Research”. In: *Laboratory Investigation* 98.7 (2018), pp. 844–855. DOI: 10.1038/s41374-018-0057-0.

[21] János Bencze et al. “Comparison of Semi-Quantitative Scoring and Artificial Intelligence Aided Digital Image Analysis of Chromogenic Immunohistochemistry”. In: *Biomolecules* 12.1 (2022), p. 19. DOI: 10.3390/biom12010019.

[22] André Forjaz, Eduarda Vaz, Valentina Matos Romero, et al. “Three-Dimensional Assessments Are Necessary to Determine the True, Spatially Resolved Composition of Tissues”. In: *Cell Reports Methods* 5.6 (2025), p. 101075.

[23] Alexander Kurz et al. “3-Dimensional Reconstruction From Histopathological Sections: A Systematic Review”. In: *Laboratory Investigation* 104.6 (2024), p. 102049.

[24] Philipp Nolte, Marcel Brettmacher, Chris Johann Gröger, et al. “Spatial Correlation of 2D Hard-Tissue Histology with 3D MicroCT Scans Through 3D Printed Phantoms”. In: *Scientific Reports* 13 (2023), p. 18479. DOI: 10.1038/s41598-023-45518-0.

Chapter 5

Conclusions and Future Works

5.1 Conclusions

This project investigated the therapeutic potential of conditioned culture media derived from mesenchymal stromal cells encapsulated within alginate hydrogels of tunable stiffness, with the goal of modulating the MSC secretome to promote degradation of fibrotic tissue in Duchenne Muscular Dystrophy. By varying calcium sulfate concentrations and characterizing mechanical properties via rheometry, distinct soft and stiff hydrogel environments were established and used to encapsulate MSCs in bulk alginate constructs.

Results from *in vitro* studies demonstrated that matrix stiffness plays a critical role in regulating MSC behavior. In particular, softer hydrogel environments enhanced the expression of matrix metalloproteinases, including MMP-2, MMP-3, MMP-9, and MMP-10, which are key mediators of extracellular matrix remodeling. Although MMP-3 expression did not significantly differ between soft and stiff matrices under TNF-α stimulation, its overall upregulation, particularly in soft matrices, remains notable given its established role in collagen remodeling and fibrotic progression. These findings suggest that a compliant microenvironment may promote a more therapeutically favorable secretory profile.

ELISA-based protein quantification further supported the gene expression data, confirming elevated MMP-3 secretion by encapsulated MSCs compared to traditional plastic culture conditions. While stiffness-dependent differences in MMP-3 secretion were not significant under inflammatory stimulation, the soft hydrogel condition remained advantageous due to its broader enhancement of multiple MMPs. This suggests that modulation of matrix mechanics may influence not just individual factors, but the overall composition of the MSC secretome, potentially enabling synergistic effects on fibrotic tissue degradation.

To assess the functional relevance of these findings, *in vivo* studies were conducted using wild-type (DBA) and dystrophin-deficient (mdx) mice. Behavioral analysis using the AnyMaze tracking system revealed that treated mdx mice exhibited increased anti-clockwise turning behavior, which may reflect altered motor patterns or asymmetrical limb function. Given that injections were administered locally, this observation may indicate improved function or strength in the treated limb, although behavioral measures alone cannot definitively establish the underlying mechanism.

Histological analyses provided more direct evidence of ECM remodeling. Immunohistochemical staining for fibronectin demonstrated a reduction in fibronectin deposition in muscles exposed to CCM, indicating an effect on early-stage fibrotic processes. Subsequent Masson's trichrome staining revealed a decrease in collagen content in treated muscle, although these effects were more modest and muscle-dependent. Together, these findings support a model in which CCM influences early ECM remodeling and may partially attenuate the progression of fibrosis. Importantly, the differential effects observed between fibronectin and collagen highlight a key insight of this study: while CCM is effective at modulating early fibrotic markers, its ability to reverse established fibrosis is more limited. This suggests that timing and disease stage may be critical determinants of therapeutic efficacy. Additionally, variation in response between muscle groups indicates that local tissue environment and baseline disease severity play important roles in treatment outcomes.

Overall, these results demonstrate that MSC-derived conditioned media, particularly when generated within soft, biomimetic hydrogel environments, holds promise as a therapeutic strategy for modulating fibrotic remodeling in DMD. By enhancing the secretion of matrix-degrading enzymes, this approach offers a potential means of targeting fibrosis indirectly through cell-derived factors, rather than requiring direct cell engraftment.

In conclusion, this study provides foundational evidence that engineering the microenvironment of MSCs can be leveraged to direct their secretome toward anti-fibrotic outcomes. These findings contribute to the broader development of biomaterial-based therapies for DMD and highlight the potential of fibronectin-targeted and MMP-mediated strategies to mitigate fibrosis and improve muscle tissue integrity.

5.2 Future Work

Future work will focus on expanding both the scope and depth of this study to further evaluate and optimize the therapeutic potential of MSC-derived conditioned media. Increasing sample size will be a critical first step to improve statistical power and reduce variability across both behavioral and histological outcomes. In parallel, refining delivery strategies, such as optimizing injection frequency, dosage, and targeting, will be essential to enhance treatment consistency and efficacy. Further characterization of the molecular mechanisms underlying ECM remodeling, particularly the role of MMPs and their interactions with fibronectin and collagen, will also provide important insight into how this therapy functions at a mechanistic level.

To better assess functional outcomes, future studies will incorporate additional assays of muscle performance, including strength-based tests such as hanging or grip assays, as well as measurements of muscle contractility. Longitudinal studies will also be implemented to evaluate the progression of fibrosis over time and to determine whether conditioned media acts primarily to prevent fibrosis, delay its progression, or reverse established tissue remodeling.

Building upon the current work, future efforts will expand to include primary cell isolation and single-cell encapsulation using a microfluidic approach currently under development in the laboratory. Emerging literature suggests that singly encapsulated or singly coated MSCs may exhibit enhanced gene expression and improved therapeutic efficacy compared to bulk populations[1,2]. By encapsulating individual MSCs within defined microenvironments, it may be possible to achieve greater control over cell behavior and secretome composition.

These primary cells will be individually encapsulated and delivered *in vivo* using DBA and mdx mouse models of DMD. Outcomes will be evaluated through a combination of behavioral assays and histological analyses, including quantification of fibronectin and collagen deposition. This approach aims to more closely mimic physiological cellular organization while improving the consistency and potency of the therapeutic response.

Ultimately, future studies will compare the efficacy of this MSC-based conditioned media approach to existing or commercially available therapies for DMD. Such comparisons will be critical

in determining the translational potential of this strategy and its viability as a competitive therapeutic option. By integrating advances in biomaterials, cell engineering, and *in vivo* evaluation, this work has the potential to contribute toward the development of more effective, targeted treatments for fibrosis in dystrophic muscle.

References

[1] S. W. Wong et al. “Controlled Deposition of 3D Matrices to Direct Single Cell Functions”. In: *Advanced Science* 7.20 (2020), p. 2001066. DOI: 10.1002/advs.202001066. URL: https://doi.org/10.1002/advs.202001066.

[2] S. W. Wong et al. “Inhibition of aberrant tissue remodelling by mesenchymal stromal cells singly coated with soft gels presenting defined chemomechanical cues”. In: *Nature Biomedical Engineering* 6.1 (2022), pp. 54–66. DOI: 10.1038/s41551-021-00740-x. URL: https://doi.org/10.1038/s41551-021-00740-x.

Appendix A

CTAB Bulk Mixture Recipe (100 mL)

1. 70 mL of solvent (RNase free H_2O) put in graduated cylinder with a stir bar
2. Add 2 g CTAB
3. Add 2 g polyvinylpyrrolidone
4. Add 8.1816 g of NaCl
5. Add 1.576 g of Tris-HCl
6. Add .58498 g of EDTA
7. Wait until fully dissolved
8. Remove stir bar
9. Add RNase free water until reaches 99 mL
10. Put in 100 mL bottle
11. pH solution until it equals 8.0 (this is when it turns clear)
12. Autoclave
13. Add back stir bar
14. Add 1 mL B-mercaptoethanol

Appendix B

MMP-3 Excel Standard Curves

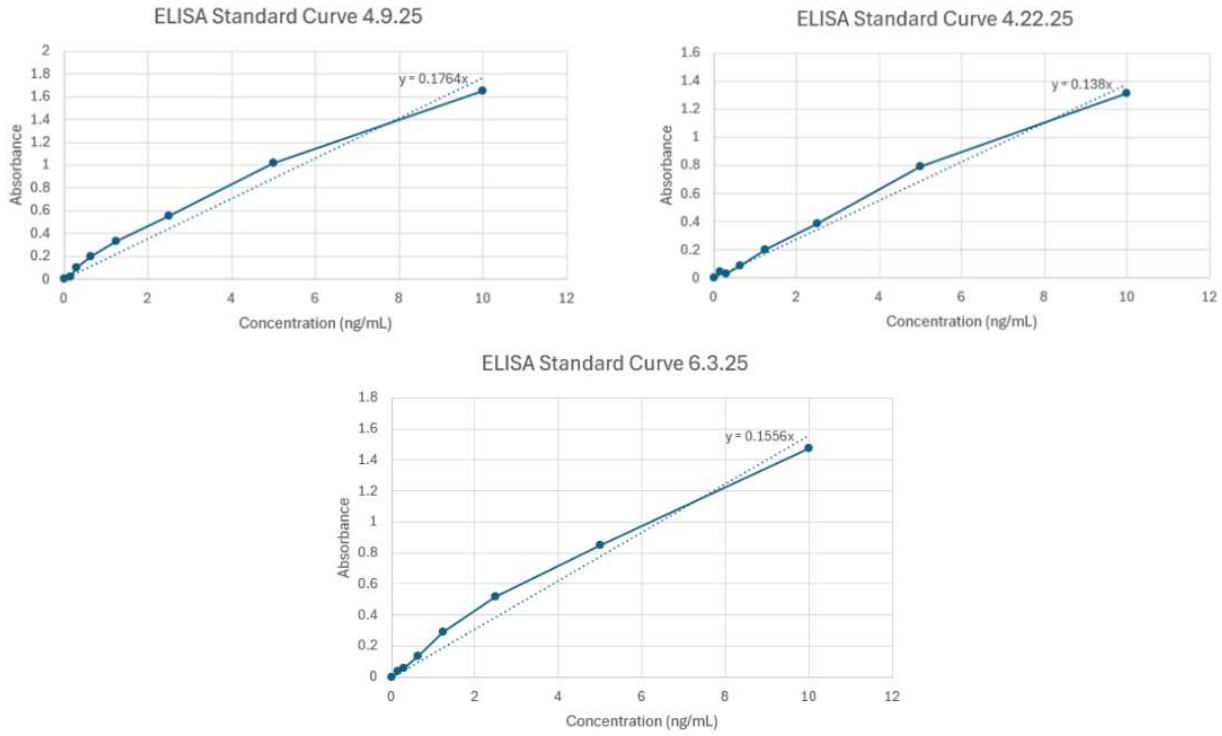

Figure B.1: Excel-generated standard curves from the three MMP-3 ELISA experiments

Appendix C

ImageJ Editable Collagen Macro

```
// ==========================
// Editable Collagen Macro (Original Tissue Colors + Blue Collagen)
// ==========================

// Define pixel size in micrometers
pixelSize = 0.548;
pixelArea = pixelSize * pixelSize;

// Adjustable darkness factor for right side overlay
darkenFactor = 0.5;  // 0.7 = lighter, 0.3 = darker

dir = getDirectory("Choose folder with your image");
list = getFileList(dir);

csvPath = dir + "collagen_results.csv";
File.delete(csvPath);
File.append("ImageName,CollagenPixels,TissuePixels,CollagenPercent,
    CollagenArea_um2,TissueArea_um2\n", csvPath);

setBatchMode(true);

for (i = 0; i < list.length; i++) {
    if (endsWith(list[i], ".png") || endsWith(list[i], ".jpg") || endsWith(
        list[i], ".tif")) {

        open(dir + list[i]);
        title = getTitle();
        run("RGB Color");

```

```
width = getWidth();
height = getHeight();

totalPixels = 0;

// --- Step 1: Count tissue pixels and identify initial collagen ---
newImage("collagenMask", "8-bit black", width, height, 1);
selectWindow(title);

for (y = 0; y < height; y++) {
    for (x = 0; x < width; x++) {
        value = getPixel(x, y);
        r = (value & 0xff0000) >> 16;
        g = (value & 0x00ff00) >> 8;
        b = (value & 0x0000ff);

        if (r + g + b < 700) { // tissue pixel
            totalPixels++;
            if (b > r + 37 && b > g + 37 && b > 100) {
                selectWindow("collagenMask");
                setPixel(x, y, 255); // mark collagen in mask
                selectWindow(title);
            }
        }
    }
}

// --- Step 2: Create editable overlay on top of original tissue ---
run("Duplicate...", "title=EditableOverlay");
selectWindow("EditableOverlay");

// packed RGB for blue
blue = (0<<16) + (0<<8) + 255;
```

```
61
62          for (y = 0; y < height; y++) {
63              for (x = 0; x < width; x++) {
64                  selectWindow("collagenMask");
65                  maskVal = getPixel(x, y) & 0xff;
66                  selectWindow("EditableOverlay");
67
68                  if (maskVal > 0) {
69                      setPixel(x, y, blue); // paint collagen blue
70                  }
71              }
72          }
73
74          // --- Step 3: Let user manually edit collagen ---
75          setBatchMode(false);
76          waitForUser("Edit collagen areas directly on the overlay (blue on
               tissue). Click OK when done.");
77          setBatchMode(true);
78
79          // --- Step 4: Recount collagen + tissue pixels after manual editing
               ---
80          bluePixels = 0;
81          newTotalPixels = 0;
82          selectWindow("EditableOverlay");
83
84          for (y = 0; y < height; y++) {
85              for (x = 0; x < width; x++) {
86                  value = getPixel(x, y);
87                  r = (value & 0xff0000) >> 16;
88                  g = (value & 0x00ff00) >> 8;
89                  b = (value & 0x0000ff);
90
91                  if (r + g + b < 700) {
```

```
                newTotalPixels++;
            }
            if (b > r + 37 && b > g + 37 && b > 100) {
                bluePixels++;
            }
        }
    }

    percent = (bluePixels / newTotalPixels * 100);
    collagenArea = bluePixels * pixelArea;
    tissueArea = newTotalPixels * pixelArea;

    // --- Step 5: Save results to CSV ---
    line = title + "," + bluePixels + "," + newTotalPixels + "," + d2s(
       percent, 2) + "," + d2s(collagenArea, 2) + "," + d2s(tissueArea,
       2) + "\n";
    File.append(line, csvPath);

    // --- Step 5b: Print to log ---
    print("Image: " + title);
    print("Edited Collagen (blue) pixels: " + bluePixels);
    print("Original total tissue pixels: " + totalPixels);
    print("Edited total tissue pixels: " + newTotalPixels);
    print("Collagen %: " + d2s(percent, 2));
    print("Collagen area (ÂţmÂš): " + d2s(collagenArea, 2));
    print("Total Tissue area (ÂţmÂš): " + d2s(tissueArea, 2));
    print("----------------------------");

    // --- Step 6: Save overlay ---
    saveAs("Tiff", dir + title + "_overlay.tif");

    // --- Step 7: Side-by-side comparison ---
    newImage("Comparison_" + title, "RGB black", width*2, height, 1);
```

```
123
124         open(dir + list[i]);
125         title = getTitle();
126         selectWindow(title); run("Copy");
127         selectWindow("Comparison_" + title); makeRectangle(0,0,width,height);
                run("Paste");
128
129         selectWindow(title +"_overlay.tif"); run("Copy");
130         selectWindow("Comparison_" + title); makeRectangle(width,0,width,
                height); run("Paste");
131
132         // --- Darken right side but keep collagen bright ---
133         selectWindow("Comparison_" + title);
134         for (y = 0; y < height; y++) {
135             for (x = width; x < width*2; x++) {
136                 value = getPixel(x, y);
137                 r = (value & 0xff0000) >> 16;
138                 g = (value & 0x00ff00) >> 8;
139                 b = (value & 0x0000ff);
140
141                 if (b > r + 37 && b > g + 37 && b > 100) {
142                     newVal = (r<<16) + (g<<8) + b;
143                 } else {
144                     r = r * darkenFactor;
145                     g = g * darkenFactor;
146                     b = b * darkenFactor;
147                     newVal = (r<<16) + (g<<8) + b;
148                 }
149                 setPixel(x, y, newVal);
150             }
151         }
152
153         // --- Step 8: Add labels ---
```

```
154         setFont("SansSerif", 18, "bold");
155         setColor("yellow");
156         textX = width + 20; textY = 30;
157         drawString("Total Tissue Area: " + d2s(tissueArea, 2) + " ÂţmÂš",
                textX, textY);
158         drawString("Collagen Area: " + d2s(collagenArea, 2) + " ÂţmÂš", textX,
                textY + 25);
159         drawString("Collagen %: " + d2s(percent, 2) + "%", textX, textY + 50);
160
161         saveAs("Tiff", dir + "Comparison_" + title + ".tif");
162
163         // --- Step 9: Close images ---
164         close(title);
165         close("collagenMask");
166         close("EditableOverlay");
167     }
168 }
169
170 setBatchMode(false);
```

Listing C.1: Editable Collagen Macro used for quantifying and visualizing collagen content while preserving original tissue colors.

Appendix D

ImageJ Editable Fibronectin Macro

```
// ==========================
// IHC GREEN MACRO: FINAL + SIDE-BY-SIDE OUTPUT + THRESHOLD LOGGING
// ==========================

// Pixel size
pixelSize = 0.650;
pixelArea = pixelSize * pixelSize;

// ==========================
// CHOOSE FOLDER
// ==========================
dir = getDirectory("Choose folder with your images");
list = getFileList(dir);

// Output folder
outDir = dir + "output_images/";
File.makeDirectory(outDir);

// CSV with thresholds logged
csvPath = dir + "ihc_results.csv";
File.delete(csvPath);
File.append("ImageName,MinGreen,MinExcess,GreenPixels,TissuePixels,
    GreenPercent,GreenArea_um2,TissueArea_um2\n", csvPath);

// Defaults
minTissue = 30;
minGreen = 40; // starting faint-slide default
minExcess = 20;

```

```
// ==========================
// LOOP
// ==========================
for (i = 0; i < list.length; i++) {

    if (endsWith(list[i], ".png") || endsWith(list[i], ".jpg") || endsWith(
        list[i], ".tif")) {

        open(dir + list[i]);
        title = getTitle();
        run("RGB Color");

        width = getWidth();
        height = getHeight();

        // ==========================
        // TISSUE EDIT
        // ==========================
        adjustingTissue = true;
        while (adjustingTissue) {

            Dialog.create("Tissue Threshold - " + title);
            Dialog.addNumber("Min Tissue Brightness:", minTissue);
            Dialog.show();
            minTissue = Dialog.getNumber();

            run("Duplicate...", "title=TissuePreview");
            selectWindow("TissuePreview");

            white = (255<<16)+(255<<8)+255;
            black = 0;

            for (y=0; y<height; y++) {
```

```
            for (x=0; x<width; x++) {
                v = getPixel(x,y);
                r=(v&0xff0000)>>16; g=(v&0x00ff00)>>8; b=(v&0x0000ff);
                bright=(r+g+b)/3;
                if (bright>minTissue) setPixel(x,y,white);
                else setPixel(x,y,black);
            }
        }

        waitForUser("Edit tissue (WHITE), then OK.");
        if (getBoolean("Use this tissue?")) {
            adjustingTissue=false;
            rename("FinalTissueMask");
        } else {
            close("TissuePreview");
        }
    }

    // Store tissue mask
    selectWindow("FinalTissueMask");
    tissueMask = newArray(width*height);
    index=0;
    for (y=0;y<height;y++) {
        for (x=0;x<width;x++) {
            tissueMask[index++] = getPixel(x,y);
        }
    }

    // ==========================
    // GREEN EDIT
    // ==========================
    continuePreview=true;
    while (continuePreview) {
```

```
94
95          Dialog.create("Green Thresholds");
96          Dialog.addNumber("Min Green:", minGreen);
97          Dialog.addNumber("Min Green Excess:", minExcess);
98          Dialog.show();
99
100         minGreen = Dialog.getNumber();
101         minExcess = Dialog.getNumber();
102
103         selectWindow(title);
104         run("Duplicate...", "title=EditableOverlay");
105         selectWindow("EditableOverlay");
106
107         green = (0<<16)+(255<<8)+0;
108
109         for (y=0;y<height;y++) {
110             for (x=0;x<width;x++) {
111                 v=getPixel(x,y);
112                 r=(v&0xff0000)>>16; g=(v&0x00ff00)>>8; b=(v&0x0000ff);
113                 bright=(r+g+b)/3;
114                 if (bright>minTissue) {
115                     gExcess=g-(r+b)/2;
116                     if (g>minGreen && gExcess>minExcess)
117                         setPixel(x,y,green);
118                 }
119             }
120         }
121
122         waitForUser("Edit GREEN, then OK.");
123         if (getBoolean("Use this green?")) continuePreview=false;
124         else close("EditableOverlay");
125     }
126
```

```
127         // Store overlay pixels
128         selectWindow("EditableOverlay");
129         overlayPixels = newArray(width*height);
130         index=0;
131         for (y=0;y<height;y++) {
132             for (x=0;x<width;x++) {
133                 overlayPixels[index++] = getPixel(x,y);
134             }
135         }
136 
137         // ==========================
138         // COUNTING
139         // ==========================
140         greenPixels=0;
141         tissuePixels=0;
142         index=0;
143 
144         for (y=0;y<height;y++) {
145             for (x=0;x<width;x++) {
146 
147                 vT = tissueMask[index];
148                 rT=(vT&0xff0000)>>16; gT=(vT&0x00ff00)>>8; bT=(vT&0x0000ff);
149 
150                 if (rT>200 && gT>200 && bT>200) { // tissue
151                     tissuePixels++;
152 
153                     v = overlayPixels[index];
154                     r2=(v&0xff0000)>>16; g2=(v&0x00ff00)>>8; b2=(v&0x0000ff);
155 
156                     if (g2>200 && r2<50 && b2<50) greenPixels++;
157                 }
158                 index++;
159             }
```

```
        }

        if (tissuePixels==0) percent=0;
        else percent=(greenPixels/tissuePixels)*100;

        greenArea = greenPixels * pixelArea;
        tissueArea = tissuePixels * pixelArea;

        // ==========================
        // LOG TO CSV (with thresholds)
        // ==========================
        File.append(title + "," + minGreen + "," + minExcess + "," +
            greenPixels + "," + tissuePixels + "," +
            d2s(percent,3) + "," +
            d2s(greenArea,3) + "," +
            d2s(tissueArea,3) + "\n", csvPath);

        // ==========================
        // SIDE-BY-SIDE OUTPUT
        // ==========================
        selectWindow(title);
        run("Duplicate...", "title=OriginalCopy");
        selectWindow("FinalTissueMask");
        run("Duplicate...", "title=TissueCopy");
        selectWindow("EditableOverlay");
        run("Duplicate...", "title=GreenCopy");

        run("Images to Stack", "name=Stack title=[] use");
        run("Make Montage...", "columns=3 rows=1 scale=1");

        saveAs("PNG", outDir + title + "_comparison.png");

        // Cleanup
```

```
193         close("*");
194     }
195 }
196 
197 print("DONE. CSV + side-by-side images saved. Thresholds logged per slide.");
```

Listing D.1: Editable Fibronectin Macro used for quantifying and visualizing fibronectin content